Numerical and experimental studies of X-ray light field imaging systems

Ying Li

▶ **To cite this version:**

Ying Li. Numerical and experimental studies of X-ray light field imaging systems. Optics / Photonic. Institut Polytechnique de Paris, 2022. English. NNT : 2022IPPAE009 . tel-04431611

HAL Id: tel-04431611
https://theses.hal.science/tel-04431611

Submitted on 1 Feb 2024

HAL is a multi-disciplinary open access archive for the deposit and dissemination of scientific research documents, whether they are published or not. The documents may come from teaching and research institutions in France or abroad, or from public or private research centers.

L'archive ouverte pluridisciplinaire **HAL**, est destinée au dépôt et à la diffusion de documents scientifiques de niveau recherche, publiés ou non, émanant des établissements d'enseignement et de recherche français ou étrangers, des laboratoires publics ou privés.

INSTITUT POLYTECHNIQUE DE PARIS

NNT : 2022IPPAE009

Thèse de doctorat

Études numériques et expérimentales de systèmes d'imagerie plénoptique à rayons X

Thèse de doctorat de l'Institut Polytechnique de Paris
préparée à Laboratoire d'Optique Appliquée

École doctorale n°626 École doctorale de l'Institut Polytechnique de Paris (EDIPP)
Spécialité de doctorat : Physique

Thèse présentée et soutenue à Palaiseau, le 06 juillet 2022 , par

YING LI

Composition du Jury :

Alexis CASNER Directeur de recherche, University of Bordeaux-CNRS-CEA	Président
David ROS Maître de conférences, IJCLab	Rapporteur
Alexis CASNER Directeur de recherche, University of Bordeaux-CNRS-CEA	Rapporteur
Sebastien LE PAPE Cadre scientifique, LULI	Examinateur
Alessia CEDOLA Directrice de recherche, CNR-Institute of Nanotechnology	Examinateur
Ombeline DE LA ROCHEFOUCAULD Ingénieure de recherche, Imagine Optic	Co-directeur de thèse
Philippe ZEITOUN Directeur de recherche, CNRS	Co-directeur de thèse

Acknowledgement

A doctoral dissertation is a long solitary journey, yet it is not something one can achieve alone. At the very end of the four-year study, I would like to thank all the people who provided indispensable support and assistance during my PhD.

First and foremost, I am deeply grateful to my supervisors, Dr. Philippe Zeitoun and Dr. Ombeline de La Rochefoucauld, for their guidance and insight into the research process. They gave me plenty of trust and freedom in my academic work, as well as the tireless moral encouragement through the rough road to finish this thesis.

Besides my advisors, I would like to thank the rest of my thesis committee:
Dr. Alexis Casner, Dr. David Ros, Dr. Sebastien Le Pape and Dr. Alessia Cedola.

The smooth running of my PhD project is inseparable from the efforts and kindness of the Laboratoire d'Optique Appliquée staff: the directors Stéphane Sebban and Antoine Rousse, the administrative members and the technical support.

I also wish to extend my warmest thanks to the colleagues and friends I have met at different stages in the past four years: Elena Longo, Domenico Alj, Charlotte Herzog, Ginevra Begani, Eirini Papagiannouli, Ghada Mahmoud, Marie Froidevaux, Zhang Yi and others even if who are not explicitly mentioned here. It is very rare to have such an international working environment outside the research field. I learned different qualities from them and appreciated different cultures. All the moments I spent with them are valuable experiences and precious memories for me.

Getting to the end, I owe special thanks to my boyfriend Rémi and his family who made me feeling at home in France.

Finally, I would like to express my love and gratitude to my beloved family. Due to the COVID-19 epidemic, my family had to grudgingly learn to accept my separation from them for years. Half a world away, they still gave me a lot of support emotionally and financially. I dedicate this thesis to my parents: Thank you for your understanding and unconditional love throughout my life.

Résumé long

L'imagerie plénoptique est une nouvelle technique d'imagerie qui s'est développée rapidement durant les trente dernières années. Le concept général de l'imagerie plénotique se résume à la description de la position et de la direction de chaque rayon lumineux dans l'espace. Plus précisément, l'imagerie plénoptique essaie de mesurer l'information spatiale et angulaire des rayons lumineux suivant le modèle de l'optique géométrique.
Une telle information plénoptique ne peut être acquise par une caméra conventionnelle. L'image bidimensionnelle obtenue par une caméra conventionnelle est en fait de l'intensité lumineuse intégrée dans toutes les directions. Ainsi, l'information angulaire est perdue lors de l'acquisition.
La caméra plénoptique a été développée dans le but de capturer aussi cette information. Une caméra plénoptique usuelle se compose d'une lentille principale, d'une matrice de micro-lentilles et d'un détecteur. Il s'agit d'un design compact capable de capturer simultanément l'information spatiale et angulaire, ce qui lui permet de refocaliser numériquement et de reconstruire un modèle 3D de l'objet imagé en une seule prise. Grâce à cette propriété, de nombreuses applications de la caméra plénoptique ont vu le jour, par exemple pour suivre l'activité de neurones, pour des systèmes de suivi industriel et pour l'imagerie volumétrique de cellules vivantes.
Cependant, tout l'intérêt scientifique et toutes les applications se sont pour le moment portés sur le domaine de la lumière visible, avec très peu de recherche sur le domaine des rayons X. Pourtant, la plénoptique en rayons X a deux avantages majeurs en comparaison avec la technique d'imagerie à rayons X 3D la plus utilisée (la tomographie assistée par ordinateur). D'abord, elle ne nécessite pas de tourner l'objet, ce qui la rend

plus pratique pour des objets encombrants ou ne pouvant être bougés. D'autre part, l'imagerie en une seule acquisition permet de réduire la dose de rayonnement ionisant reçue par des échantillons biologiques, et pourrait même nous permettre d'enregistrer des vidéos en 3D d'échantillons vivants. Ainsi, l'objectif de cette thèse est de construire un système d'imagerie plénoptique à rayons X, en particulier en vue d'applications bio-médicales.

Ce manuscrit rend compte du travail réalisé en ce sens et inclu des études théoriques, des simulations et des vérifications expérimentales. Le manuscrit est organisé de la façon suivante:

Le chapitre 1 présente une introduction générale du projet de recherche et du cadre de cette thèse.

Le chapitre 2 pose les bases théoriques de l'imagerie plénoptique, du principe de fonctionnement et de la structure de la caméra plénoptique. Différentes représentations et perspectives du champ de lumière 4D capturé par la caméra plénoptique sont aussi données dans ce chapitre.

Le chapitre 3 est entièrement consacré aux algorithmes et au traitement de l'image permettant la reconstruction de l'image plénoptique. Ces algorithmes sont cruciaux pour extraire l'information spatiale et obtenir une image de bonne qualité. Une revue est faite des méthodes déjà existantes de calibration, de refocalisation et d'estimation de la profondeur dévelopées spécifiquement pour la plénoptique. En particulier, nous comparons trois algorithmes simples de refocalisation et nous démontrons mathématiquement les liens entre ces différents algorithmes.

Dans le chapitre 4, nous proposons un système d'imagerie plénoptique basé sur des plaques zonales de Fresnel (FZP, Fresnel Zone Plate en anglais) dans lequel les lentilles réfractives sont remplacées par des FZPs basées sur la diffraction. Une limitation importante de ce système se trouve dans le compromis entre la taille et la résolution de chaque FZP dans la matrice de FZP. Ce compromis se retrouve dans le choix du nombre de zones de la FZP. Afin de mieux guider ce choix, nous avons développé un algorithme de simulation basé sur la théorie de la diffraction, nous permettant ainsi d'étudier l'effet

du nombre de zones sur la performance d'imagerie de la FZP pour différentes conditions de cohérence de la lumière.

La précision de la reconstruction 3D est intimement liée à l'ouverture numérique de la lentille principale de la caméra plénoptique. Cependant, les optiques pour rayons X ont souvent une très petite ouverture numérique à cause de la faible interaction des rayons X avec la matière, particulièrement pour les rayons X de haute énergie. Ainsi, nous nous sommes intéressés au cristal courbe pour ses propriétés de focalisation tout en gardant une large ouverture numérique. Le but du chapitre 5 est donc d'examiner les performances d'imagerie du cristal courbe en tant que lentille principale de notre caméra plénoptique. En développant notre propre algorithme de traçage de rayons, nous avons étudié la taille de la zone effective diffractante du cristal et sa capacité de focalisation pour différentes géométries. Nous avons fait fabriquer trois cristaux de notre conception, deux cristaux toroïdaux et un cristal cylindrique afin de les utiliser comme lentille principale et comme condenseur respectivement. Ce chapitre détaille aussi les mesures de diffraction des rayons X que nous avons réalisées pour vérifier les paramètres des trois cristaux, ainsi que des mesures préliminaires d'imagerie avec l'un des cristaux toroïdaux.

Le chapitre 6 s'intéresse aux mesures expérimentales sur le système plénoptique complet à deux énergies différentes pour les rayons X. Dans la première partie, nous présentons la construction d'un microscope plénoptique aux rayons X dans la fenêtre dite "de l'eau". Les composants principaux du microscope, ainsi que la source laser-plasma émettant les rayons X doux, sont décrits en détail. La deuxième partie contient un rapport détaillé de la première expérience d'une caméra plénoptique basée sur des FZPs sur une source synchrotron émettant des rayons X à 11 keV. Le dispositif expérimental et l'acquisition des données y sont détaillés. Nous y analysons les images brutes expérimentales et le traitement d'image utilisé. Nous avons appliqué un algorithme de refocalisation développé pour la lumière visible sur les images plénoptiques obtenues avec des rayons X et nous montrons les images obtenues à l'issue du traitement. Nous évaluons quantitativement la performance de notre système expérimental selon plusieurs paramètres d'imagerie.

Nous analysons aussi la qualité des images refocalisées et la profondeur est extraite des données expérimentales du champ plénoptique.
Finalement, dans le chapitre 7, nous résumons le travail effectué et son intérêt pour la recherche actuelle et future.
En conclusion, le travail réalisé pendant cette thèse a contribué à la compréhension de l'imagerie plénoptique aux rayons X et a établi les bases permettant de construire une caméra plénoptique dans les rayons X de par la conception d'éléments optiques adaptés.

Table of Contents

Chapter 1

Introduction

Vision, one of the most important human senses, is based on detecting the wealth of information carried by light to perceive the world. The three-dimension structure of our environment is strongly shaped from the integration of the cues unconsciously extracted from the light that passes through the scene and is received by our eyes. To theoretically describe the light flow at each point and in each direction in space, the notion of light field has been coined as early as 1936. Modern light field of a stereo scene has been simplified and summarised to a series of four-dimension (4D) functions under geometric optics. That is, the spatial and angular information of each light ray propagating in the scene is parameterized by the coordinates of its two intersections with two separate planes.

Such 4D light field can not be recorded by the conventional cameras, which produce a 2D image by integrating the intensity of light rays in all directions, thus losing the angular information of the light field. Various imaging systems for the acquisition of light field, known as plenoptic cameras, have been proposed and developed. The plenoptic cameras are basically created by inserting a second imaging component, an optical splitter, into the conventional camera to retain the angular information of the captured light.

Thanks to the additional angular information, plenoptic camera combined with dedicated algorithms makes it possible to numerically change focus, switch views and render 3D model after image capture in a single snapshot. Due to this property, plenoptic cam-

eras opens the gateway to a broad range of applications, especially in computer vision, industrial inspection, biomedical diagnostics, etc. Although light field imaging and plenoptic cameras have been extensively studied and applied in visible light, there have been very limited developments about X-ray light field imaging system.

Compared to the most common 3D X-ray imaging technology, computed tomography, the significant advantages of implementing the light field imaging in X-ray range includes two main aspects. First, with a single acquisition, quasi-3D information encapsulated in the light field can be obtained. Thus this technique could be used to image biological samples with lower radiation damage. Secondly, a series of short single acquisitions could be envisaged, i.e. video imaging. This would enable 3D videos of living organisms without requiring immobilization.

However, to transform the plenoptic camera from visible light to X-rays, the most challenging problem is finding the alternative optical components to refractive lenses, since the refractive index is very closed to unity for all materials in X-ray range. Therefore, this thesis aims at building a prototype of X-ray light field imaging system with adapted optical elements to achieve near-3D X-ray images in very few exposures in primary stage. The work performed in this thesis is all based on the configuration of a mainstream and commercialized plenoptic camera in visible light, consisting of main lens, micro-lens array and detector.

We report in this manuscript the work carried out to prototype an X-ray light field imaging system by the following content structure:

To serve as a groundwork, Chapter 2 gives an overview of light field imaging and plenoptic camera. We introduce in detail the principle and structure of plenoptic camera. The different representations of the 4D light field dataset captured by plenoptic camera arranged from different perspectives are also summarized in this chapter.

Chapter 3 is dedicated to the processing and algorithms behind the light field reconstruction, which play a crucial role in spatial information extraction and imaging quality. We review the existing calibration method, refocusing and depth estimation approaches developed specifically for light field data in this chapter. In particular, we compare

three basic refocusing algorithms with each other and mathematically demonstrate the interconnection between them.

In Chapter 4, we propose an X-ray light field imaging system based on Fresnel zone plate (FZP), i.e. replacing refractive lenses in visible light system by diffractive FZPs. One major issue with this design is the trade-off between the size and the resolution of each FZP in the lens array. This trade-off is reflected in the choice of the number of zones for the FZP. To address this issue, we develop a simulation algorithm based on the diffraction theory. With the help of this algorithm, we investigate the effect of the number of zones on the imaging performance of FZP.

A main drawback of FZP used as the main lens of the X-ray light field imaging system is its limited numerical aperture, especially for hard X-rays, leading to low depth resolution in 3D reconstruction. To counter this shortcoming, diffractive curved crystal seems to be an optimal alternative optics for the main lens. Therefore, the theme of Chapter 5 is to examine the imaging performance of the curved crystal for the use of the main lens. Using a ray-tracing algorithm, we study the effective diffracting area and the focusing ability of the curved crystal with different geometries. The toroidal crystal attracts our attention for its imaging focusing property and large numerical aperture. Three crystals of our customized design have been purchased, including two toroidal crystal and one cylindrical crystal to serve as the main lens and condenser, respectively. This chapter reports in detail the X-ray diffraction measurements performed to verify the geometries of the three crystals, as well as the preliminary imaging testing of one toroidal crystal.

Chapter 6 reports the experimental work on the entire light field imaging system at two different X-ray energies. In the first part, the construction of an X-ray light field microscope in the "water window" is presented. The main components of the X-ray light field microscope, including the laser-plasma source emitting soft X-rays, are described in detail. The second part provides a comprehensive report of the first experiment of the FZP-based light field imaging system with synchrotron X-ray radiation at 11 keV. The experimental set-up and data acquisition method are described in detail. We interpret

the experimental raw images and discuss the corresponding image processing. We apply the refocusing algorithm developed from visible light on the X-ray light field images and display the resulting images. We quantitatively evaluate the performance of the experimental X-ray light field system by several imaging parameters. In the meantime, we analyze the quality of the refocused images and extract the depth information from the acquired light field data.

Chapter 2

Light Field Overview

2.1 Light field Definition

The concept that the light should be interpreted as a field like the magnetic field, was firstly suggested by Michael Faraday in 1846[1]. The term "light field" originated from Andrey Gershun's publication on the radiometric properties of light in three-dimensional space in 1939 [2]. Light field, representing the light flow at each point and in each direction in space, becomes popular in the domain of computer graphics and vision in the last few decades. In order to systematically study how to extract spatial geometric information from the images, Adelson and Bergen [3] introduced the "plenoptic function" to parameterize the propagation of light with rays model. In 1996, Levoy and Hanrahan [4] and Gortler et al.[5] simplified the plenoptic function with two-planes parameterization and developed light field into a 4D vector term. The notion of light field that we are familiar with nowadays is the collection of 4D plenoptic functions, which describes the total distribution of light rays in space.

2.2 Plenoptic Function and Two-planes Parameterization

The original plenoptic function, firstly introduced by Adelson and Bergen, describes the geometric distribution of light flow in space by 7 parameters: three for spatial position, two for angular directions, plus wavelength and time.

$$LF = L(x, y, z, \theta, \phi, t, \lambda) \tag{2.1}$$

For a monochromatic light at a given time (t and λ fixed), the 7D plenoptic function is reduced to a 5D parameterization 2.2, the most straightforward way to represent a light ray, as illustrated in figure 2.1(a).

$$LF = L(x, y, z, \theta, \phi) \tag{2.2}$$

As stated in Levoy and Hanrahan [4] and Gortler et al.[5], the plenoptic function can be further simplified from 5D to 4D via two-planes parameterization. Assuming a light ray passes through a two planes system, as shown in figure 2.1(b), the 4D plenoptic function uses two pairs of spatial coordinates of the intersections with two planes to determine the light ray's position and direction, noted as

$$LF = L(u, v, s, t) \tag{2.3}$$

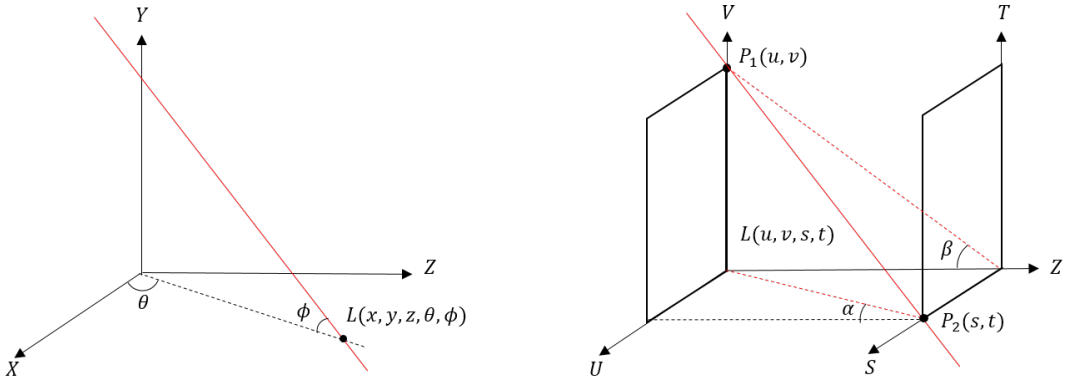

(a) **(b)**

Figure 2.1: (a) 5D plenoptic function representation : a light ray can be described with 3 spatial coordinates and 2 angular coordinates. The red line is an example of a ray passing through the two planes. (b) Two-plane parameterization: a light ray can also be defined by four spatial coordinates of two intersection points $P1$ and $P2$ on two different planes. The ray's direction is represented by the two incident angles α and β on the VZ and UZ planes, equally to the XZ and YZ planes in (a).

Different from the angular representation θ and ϕ in the coordinate system of the 5D plenoptic function, the ray's direction in the two-planes parameterization is given by the two incident angles α and β on the VZ and UZ planes, equally to the XZ and YZ planes in figure 2.1(a). Under the paraxial approximation and with a known distance between the two planes z, α and β can be given by

$$\alpha \approx \frac{u-s}{z},\ \beta \approx \frac{v-t}{z} \tag{2.4}$$

2.3 Light Field Acquisition

The main advantage of the two-planes parameterization is not only to reduce the dimensionality of plenoptic function, but more importantly, to enable the measurement of light field by the imaging devices. Although a conventional camera contains two planes: the lens and the photo sensor planes, it cannot capture the 4D light field from a scene. This is due to the fact that each point on the sensor plane is actually an integral of the rays from the lens, and the directional information of each ray is lost after being recorded.

In visible light, many attempts have been made to built a light field acquisition system. One main idea of the light field acquisition system is to separate the incident light from the lens before arriving on the photosensor plane. As early as 1908, long before the concept of light field appeared, Lippmann proposed to place a homemade lenslet array in front of photographic film, named as "integral photography", to acquire a collection of 2D elemental images for 3D scene displaying [6]. However, limited by the manufacturing of precision optics and the computational capacity, it was not until the 1990s that light field acquisition device has experienced a rapid development with the advancement of the digital photographic cameras. In 1992, the term "Plenoptic Camera" is generated after Adelson and Wang's publication, which provided the first pinhole-based light field acquisition device and reported a computer-aided analysis on plenoptic image data [7]. This idea has been further exploited and refined by Ng et al. Inserting a micro-lens array (MLA) in front of the sensor in the conventional camera, they prototyped a hand-

held light field camera, which was published in 2005 with a computational refocusing algorithm [8]. Their work demonstrated the ability of the light field camera to refocus and display the scene from different angles with a single acquisition. However, the refocusing algorithm of Ng et al. treats each micro-lens as a reconstructed pixel on the refocused plane, which leads to a significant loss in resolution of the final image. Three years later, Lumsdaine and Georgiev proposed different configuration allowing flexibility of the MLA position associated to a new algorithm [9].

(a) (b) (c)

(d) (e)

Figure 2.2: Various plenoptic cameras: (a) Stanford multi-camera array [10] (b) Adobe LightField camera [11] (c) Coded Aperture [12] (d) Lytro [13] and (e) Raytrix [14]

Besides the aforementioned light field camera design, the acquisition system developed in various directions. The Stanford multi-camera array model incorporates a large numbers of cameras to capture the light emitted from the scene at different angles (figure 2.2 (a))[10]. Adobe Light Field camera relies on a special compound lens made of 19 sub-lenses in a hexagonal array to split the incident rays (figure 2.2 (b)) [11]. The Coded Aperture method records simultaneously the high resolution image information and depth information with a patterned mask within the aperture of the conventional

camera (figure 2.2 (a)) [12].

Currently, the designs consisting of a main lens, a micro-lens array and a photosensor are most common in the light field cameras on the market, such as Lytro and Raytrix (see figures 2.2 (d) and (e)). This sensor-side structured light field camera will be further discussed in the following sections.

2.4 Configuration of the sensor-side structured plenoptic camera

The sensor-side structured plenoptic camera records the light field by a light-splitting optics, such as a microlens array, a pinhole mask and so on, placed in the front of the photosensor. According to the relative position between the light-splitting optics and the intermediate image from the main lens, this kind of plenoptic camera can be subdivided into two categories: the unfocused plenoptic camera with the light-splitting optics on the intermediate image plane and the focused plenoptic camera with the light-splitting optics before or after the the intermediate image plane (see figures 2.3 (a), (b) and (c)).

The typical light field images obtained from each camera are displayed in figure 2.3 (d), (e) and (f). This classification method assumes that the object is fixed and on a single plane. Under this assumption, these three configurations can be transformed to each other by changing the distance between ML and MLA [15]. On the contrary, in practice, the plenoptic camera captures the objects located at various depths with a constant ML-MLA distance, merging all the three types of light field images.

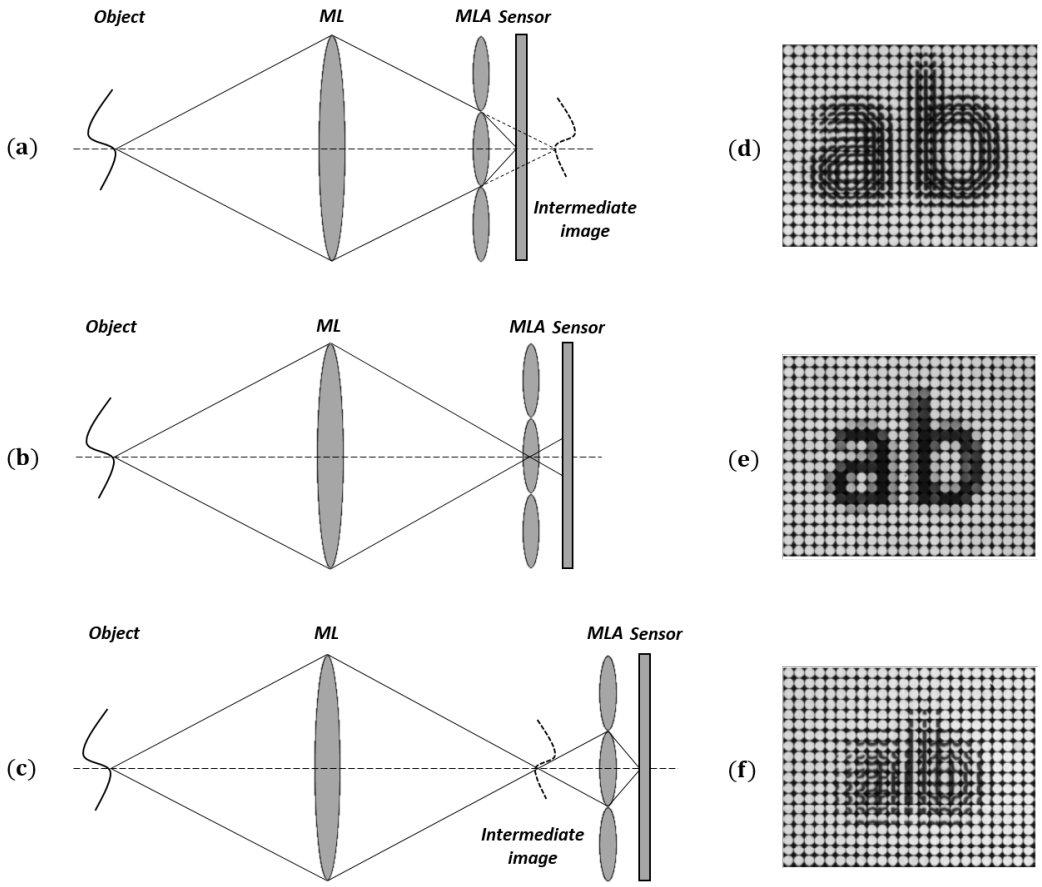

Figure 2.3: Different configurations of the sensor-side structured plenoptic camera: taken the microlens-based plenoptic camera as an example, (a) and (c) focused plenoptic camera with the MLA before and after the intermediate image plane. (b)unfocused plenoptic camera with the MLA on the intermediate image plane. (d), (e) and (f) are the typical raw light field images obtained from (a), (b) and (c). ML, main lens; MLA, microlens array (images (d),(e) and (f) from [15]).

2.5 Principle of the sensor-side structured plenoptic camera

Regardless of the configuration, the principle to capture the light field remains the same between the sensor-side structured plenoptic cameras. To explain how the plenoptic camera acquires simultaneously the spatial and angular information of the light, the geometric ray-tracing diagram of a light field acquisition system using microlens array is shown in figure 2.4 (a). Because of the symmetry of the system, we only illustrate the ray propagation of one axis in the lateral plane in the figure. Since the size of each elemental microlens is very small respect to the ML, we can simplify the model by regarding each microlens as a pinhole and considering only the chief rays (the ones passing through the center of the microlens).

Inside the plenoptic camera, the two-planes parameterization is founded by the ML and MLA planes, adopting the coordinate system in the section 2.2, noted as (u, v) and (s, t) planes, respectively. Every microlens collects the rays propagated with a certain direction from the ML and generates a micro-image on the photosensor. Moreover, the position of the pixel on the micro-image indicates the place where the ray crosses the ML. Thus, the spatial and angular information of rays are indexed by a pair of coordinates (u, v) and (s, t) of the pixels recorded in the light field image.

Conventionally, the coordinates (u, v) of the ML plane is used for angular sampling and the coordinates (s, t) of the MLA plane for spatial sampling. The meaning of this coordinates convention may not be easy to understand, if we only look at the rays inside of the plenoptic camera. By projecting the captured rays back onto the object plane, the reason behind this coordinates convention would become more explicit. The figure 2.4 (b) depicts that the rays captured by a certain microlens, namely (s, t) fixed, originate from the same position on the object plane. In the figure 2.4 (c), the rays recorded at the identical position in each micro-images derive from the same point of the ML, namely (u, v) fixed, which is equivalent to image the object at a certain point of view.

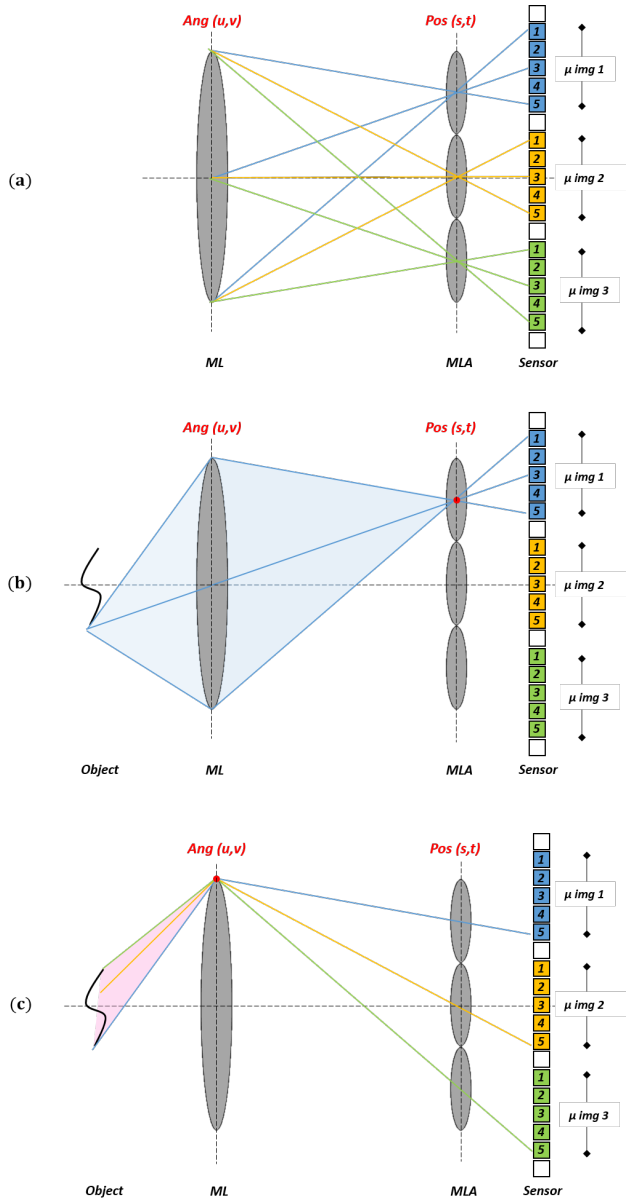

Figure 2.4: (a) Geometric ray-tracing diagram of a plenoptic camera based on MLA. Each microlens, simplified to a pinhole, only acquires the light rays of the ML with a certain direction and forms a micro-image (noted as μ image in the figure) on the sensor. (b) The MLA plane represents the spatial information: the rays captured by a certain microlens((s,t) fixed) come from the same point on the object plane.(c) The ML plane represents the angular information: the rays recorded at the identical position on each micro-images originate from the same point on the ML ((u,v) fixed), equivalent to image the object at a certain point of view.

2.6 Light field image captured by plenoptic camera

Through the plenoptic camera, the 4D light field from a scene is compressed onto a 2D light field image. The schematic representation of a raw light field image is shown in figure 2.5 (a). For clarity, each micro-image is represented with a square formed with only 4 pixels. And the pixels from the same point of view are filled with the same color and noted with the same number.

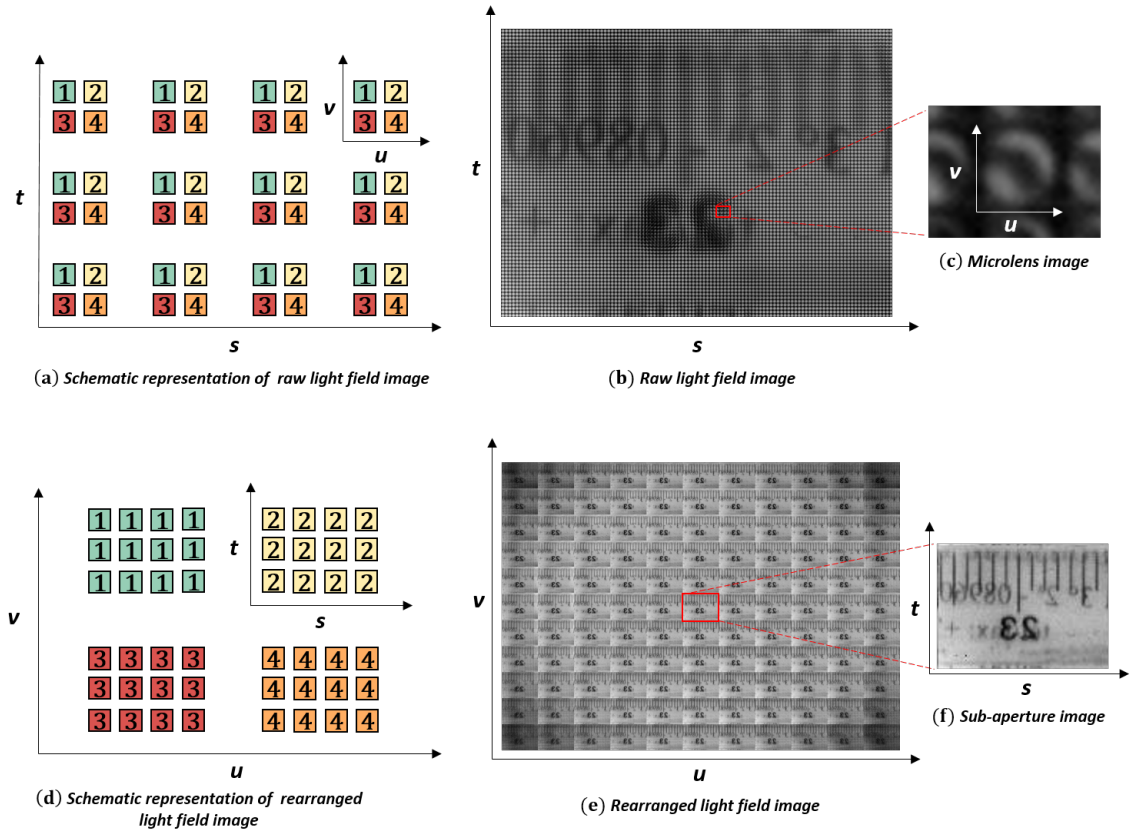

Figure 2.5: 4D light field recorded on 2D image: (a) A schematic representation of the raw light field image captured by a senor-side structured plenoptic camera. It contains 3×4 micro-images. Each image consists of 2×2 pixels colored according to the incident angle. (b) A real raw light field image from a home-made plenoptic camera using MLA, and (c) An image of a single microlens of the plenoptic camera. (d) A schematic representation of the light field image arranged by angular coordinates. The light field image in (a) becomes an array of 2×2 sub-aperture images with 3×4 pixels each after the angular arrangement. (e) The rearranged light field image corresponding to (b) is equivalent to an array of shifted perspective views of the scene. (f) The central view image of (e).

In the raw light field image, the pairs of the coordinates on the UV and ST planes inside the plenoptic camera respectively correspond to the indexes of the micro-images and the local indexes of the pixels within a micro-image. As a result, there is also an inevitable trade-off between spatial and angular resolutions due to the limited number of pixels in the detector.

The raw light field image can also be considered as a collection of images arranged by the spatial coordinates (s, t), as each micro-image is from one single microlens and contains the rays from all the sampling angles. A real raw light field image with a zoomed micro-image is displayed in figure 2.5 (b) and (c). This raw light field image consists of 79×109 micro-images, taken by a home-made plenoptic camera, of which the MLA is in the image plane of the ML and the distance between the MLA and the detector is equal to the focal length of the MLA.

Obviously, the raw light field image can be visualized by the angular coordinates (u, v) as well. By post digital processing, regrouping the pixels from the same angle generates an image of a certain view of the scene, commonly known as a sub-aperture image. The schematic drawing of the rearrangement of figure 2.5 (a) is displayed in details in figure 2.5 (d). Every sub-aperture image is created by gathering the pixels in the same color of each micro-image by the order of the spatial coordinates (s, t), each color representing a point of view. Consequently, the quality of the sub-aperture image is limited by the MLA, which pixel number is identical to the microlens number. The multi-view image array extracted from the real light field image in figure 2.5 (b) is given in figure 2.5 (e) and the central sub-aperture image with 79×109 pixels zoomed is in figure 2.5 (f).

2.7 Epipolar plane images

Another representation of the light field data is extracted from the epipolar planes. The notion of epipolar plane comes from the stereo vision. Using pair of cameras to image a point P and representing the cameras by their central points C_1, C_2, these three points form a triangle as shown in figure 2.6 (a). The plane where this triangle is located is so-

called epipolar plane. The line joining the two camera centers is known as the baseline, the red line in figure 2.6. And the intersection line between the epipolar plane and the camera image, the dotted line in figure 2.6, is called the epipolar line. A particular case of epipolar geometry occurs when all the epipolar lines are parallel to the baseline.(see figure 2.6 (b)) In other words, all the cameras have the same orientation and their images are in a common plane. This particular geometry facilitates the calculation of the disparity for extracting depth and structure.

The sub-aperture images from the plenoptic camera can be considered equivalent to this geometry, but composed of a camera array rather than two cameras. Taking advantage of the dense points of view, the light field image can be arranged in a more abstract way, the so-called epipolar plane image. The epipolar plane images (EPI) is formed by 2D slices of the sub-aperture images on the same epipolar line. There are two kinds of EPI: the horizontal ones that fix v and t while varying u and s, and the vertical ones that fix u and s while varying v and t.

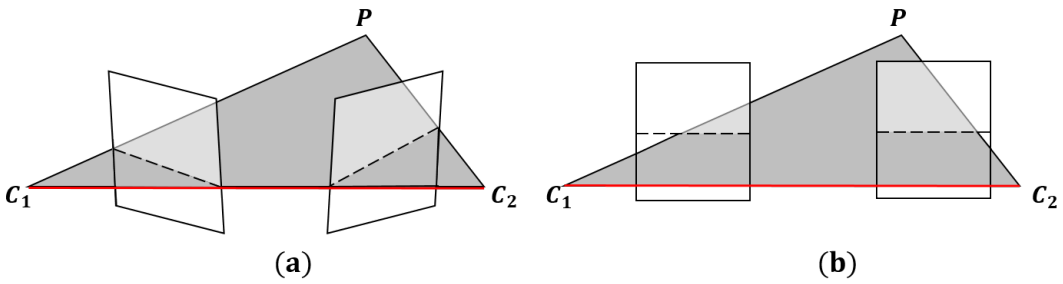

Figure 2.6: The notion of epipolar plane: (a) Imaging a point in space P with two cameras considered as two points C_1, C_2, the epipolar plane is the plane where these three points are co-planer. The dotted lines are the intersection lines between the epipolar plane and the camera images, as known as the epipolar line. And the red line joining C_1, C_2 is named as the baseline. (b) A particular geometry in which the epipolar line is parallel to the baseline, simplifies the calculation for extracting depth and structure of object.

The figure 2.7 illustrates more specifically the relationship between the sub-aperture images and the EPI with an example.

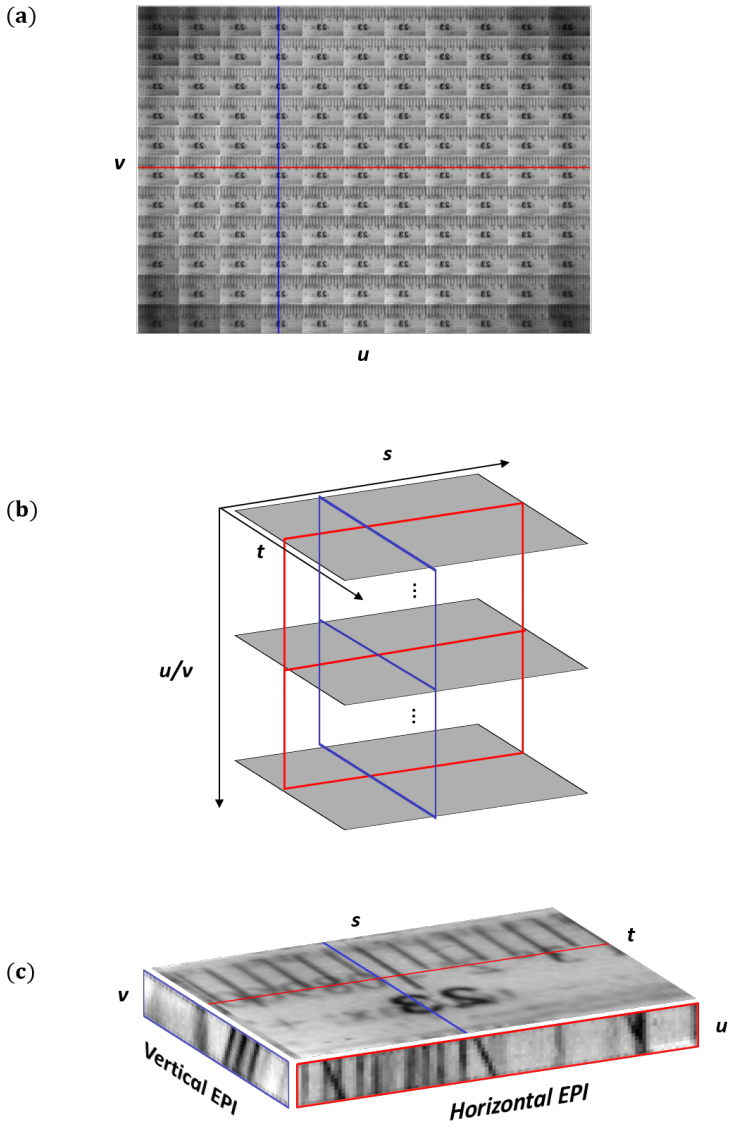

Figure 2.7: Epipolar plane image: (a) The red and blue lines mark respectively some horizontal and vertical epipolar lines on the sub-aperture images captured by a plenoptic camera. (b) Stacking up all the sub-aperture images of the row or the column covered by the epipolar lines in the order of u or v, the horizontal and vertical EPIs can be considered as the cross sections of the images volume represented by the red and blue squares, respectively. (c)The real horizontal and vertical EPIs extracted from (a) respectively have the equal length and width of the sub-aperture image.

To extract the EPI of a horizontal or vertical epipolar line, the red or blue line in figure 2.7(a) as example, we firstly stack up all the sub-aperture images of the row or the column in the order of the angular coordinates u or v, respectively. The corresponding EPIs can be considered as the cross sections of the image volume along the horizontal or vertical epipolar lines, the red and the blue squares in the figure 2.7(b). Thus, the horizontal and vertical EPI have equal length and width of the sub-aperture image, respectively. The other dimensions of the horizontal and vertical EPI are respectively equal to the number of horizontal and vertical points of view u and v, as shown in figure 2.7(c). The linear repetitive patterns in EPI are formed by the shifts of the object on the sub-aperture images from different points of view (i.e., disparity). The slope of these linear structure is related to the depth of object, which will be discussed in more details in section 3.2.

2.8 Representation of light field in phase space

The above illustrations of the plenoptic camera are based on geometrical optics. It employs the concept of light ray to describe the light behaviour propagating through a large scene without the wave character. And the rays propagating inside the plenoptic camera showed in the previous sections are all drawn in line space, where each ray is represented by an oriented line. While many properties of light fields are easier to understand in line space, the representation of light field in phase space is the more common way to perform the analysis of plenoptic camera.

In 2D phase space consisting of angular and spatial axes, a ray turns to a single point instead of a line. Due to the MLA and the pixelation of the photosensor, the light field captured by the plenoptic camera is a discrete spot array in phase space, as shown in figure 2.8 (a). Figure 2.8 (b) shows the collection of rays focused on a point in the MLA plane equivalent to a vertical line in phase space. From the captured light field, focusing the rays back to a certain depth becomes a projection with a corresponding slope in phase space, which will be further discussed in the section 3.2 (see figure 2.8 (c) and (d)). Accordingly, the phase-space diagram provides concise insight and an overview of the plenoptic camera performance. More importantly, the phase-space diagram visualises

the sampling performance of different optical designs in a uniform manner, allowing to compare different optical designs and rendering algorithms and their resolutions.

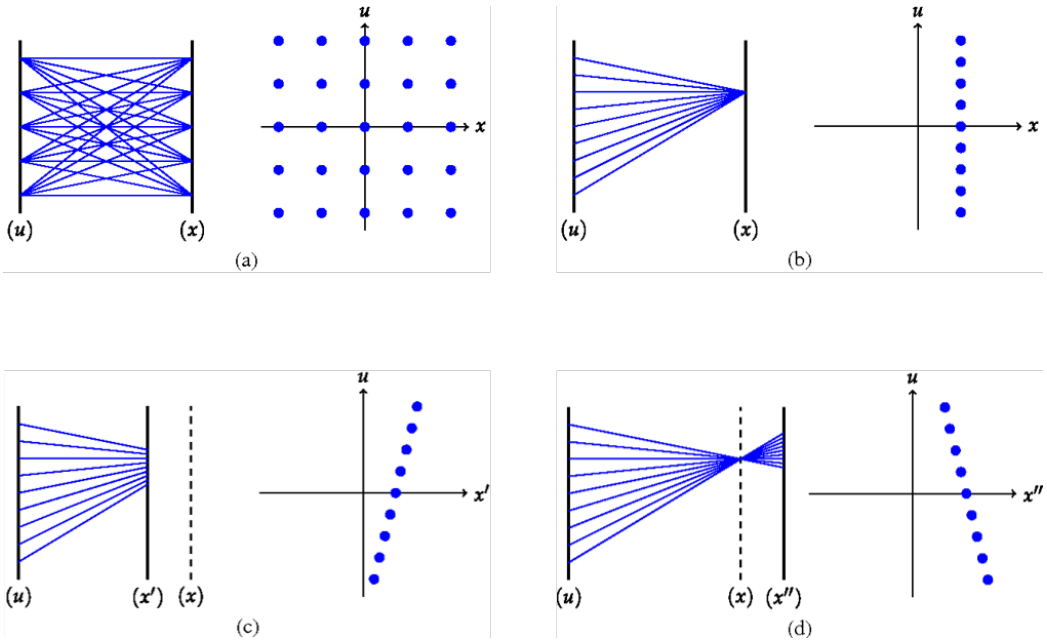

Figure 2.8: Representation of light field in line space and phase space respectively displayed on the left and the right in each sub-graphs: (a) the light field captured by the plenoptic camera is a discrete points array in phase space. (b) The rays focused on a point in the MLA plane are transformed to a vertical line in phase space. (c) and (d) illustrate that refocusing the captured light field to a certain depth is equivalent to a projection with a corresponding slope in phase space. The x axis in the figure is equal to s axis in the text. (image from [16])

2.9 Conclusion

This chapter first introduces the conception of light field and how to parameterize the light field in 3D space. Then, we briefly retraced the development of imaging devices for recording light field. We described in detail a sensor-side structured plenoptic camera and the specific image it captures, on which the work of this thesis is based. This chapter helps the readers to understand the background of the work presented in subsequent chapters.

Chapter 3

Light Field Reconstruction

In this chapter, we will review the computational post-processing of the capture light field data, including camera calibration, image refocusing and depth estimation. In particular, we explicitly present three basic refocusing algorithms of light field and illustrate their interconnections based on the geometric optic. We also relate these three algorithms to the different representations of the captured light field data. For comparison purposes, the refocusing images from the same light field data of the three algorithms are also provided.

3.1 Light field image calibration

The light field image stores the 4D information of the light ray by the coordinates of the micro-image and its pixels, and the reconstructed images are numerically synthesized from the elemental images. The quality and accuracy of the extracted micro-images are crucial to the final reconstructed results. To reconstruct the light field, the fundamental step is selecting the micro-images and locating their centers from the raw light field image in order to well establish the relationship between the pixel location and the spatial information of the light ray. This process, also referred to as "decoding" in some literature, can be a challenging task. Because the captured micro-images inevitably have geometric and intensity distortions in practice, due to the deviations in manufacturing and installation from the initial design, as well as the optical aberrations of the components. Therefore, a considerable amount of research work about the light field

camera extends to the correction of the raw image and the calibration of the system in pre-processing phase.

A common issue of the raw micro-images is the reduction of intensity from the center of the image to the border, the so-called vignetting. This phenomenon can be better observed in the sub-aperture image array in figure 2.5 (e). The image closer to the border of the sub-aperture image array is darker, because it is composed of the border pixels in each micro-image that are more affected by the vignetting. The off-axis incident rays partially blocked by the microlens aperture result in the vignetting on the image, which can be modeled by a cosine fourth law.[17] The vignetting can be approximately corrected by the intensity normalization that each pixel is divided by the fraction of its intensity to the sum of the entire micro-image.[18] A more precise correction approach with the aid of a reference white image, widely used in the traditional photography correction, has been adopted on light field image as described in [19] [20]. The general idea of this method is attempting to determine a vignetting function from the white image with various parametric models, e.g.polynomial model [21], exponential polynomial model [22], Gaussian function [23]. Meanwhile, with the basic properties as the radial symmetry and the intensity attenuation profile, the vignetting is also used to address another key issue, detection of micro-image center [24] [25] [26].

There exist other alternative approaches for estimating the center of each single micro-image as well as the entire center grid. The classical methods of image processing such as image moments and Hough circle transform have been applied to the white image of the MLA in [27] and [24], respectively. In contrast to the mentioned approaches all based on the active zones of the photosensor, the novel strategy relaying on the dark gap between micro-images to detect the centers are introduced in [28] and [29].

More precise approaches improve the micro-image correction by calibrating the plenoptic camera, attempting to obtain the intrinsic parameters of the system geometry and to correct the errors generated during the assembling, such as orientation and rotation errors of the MLA and misalignment between the ML and the MLA. These approaches usually employ a known-feature reference to compare with the projection image through

the system. Dansereau et al.[30] presented a 15-parameter geometric model refined with the corner feature of checkerboard. Similarly, Johannsen et al.[31] followed by Zeller, Noury et al. [32] investigated 3D calibration methods referring the known depth. Bok et al. [33] proposed a calibration method with line feature observed on the raw images, avoiding the errors introduced in the reconstruction step.

In general, several methods are usually combined to ensure the robustness and accuracy of the decoding process. Additional enhancements of the micro-image, such as color correction, demosaicing and denoising will not be discussed here. More details can be found in [20], [34] and [35].

3.2 Image refocusing

After discussing about how the light field image records the 4D information of the light rays from a scene in Chapter 2, this section turns the attention to the core stage, the recovery of the scene from the captured light field. One of the important qualities of the light field, which makes the plenoptic camera attractive, is the ability of refocusing at different depths after capture. The refocusing is achieved through the computational post-processing. For the plenoptic camera using MLA, the majority of the refocusing algorithms are based on the ray tracing from the two-planes paremeterized light field. Considering the symmetry of the propagation of light in the u-z plane and v-z plane, we model the plenoptic camera in the u-z plane and illustrate the refocusing reconstruction only in the 2D u-z phase space.

3.2.1 Integral method

The classical algorithm of refocusing, mainly investigated in [8], assumes that each microlens represents a refocused point. As shown in figure 3.1, the reconstruction of the refocused image is considered by moving the MLA to the virtual refocused plane and summing up the rays passing the new positions of the microlenses centers. z' and z_0 are the distances of the virtual refocused plane and the MLA plane with respect to the ML plane, respectively. And b is the distance between the MLA and the photosensor. The

ray arriving at s in the MLA plane intersects the virtual plane at s'. By the side-splitter theorem (similar triangles), the relationship between s, s', z_0 and z' is

$$\frac{s-u}{z_0} = \frac{s'-u}{z'} \tag{3.1}$$

Expressing s' in the term of s, the refocusing can be written by the equation in [8]

$$\overline{E}(s',t') = \iint L_F((1-\alpha)u + \alpha s,\ (1-\alpha)v + \alpha t,\ u,\ v)\, du\, dv, \tag{3.2}$$

where $\alpha = \frac{z'}{z_0}$. According to the equation 3.2, refocusing at a depth is an integration along a certain direction of the angular coordinates (u, v) at fixed spatial coordinates (s', t') in the phase space, and the integral direction depends on the target depth.

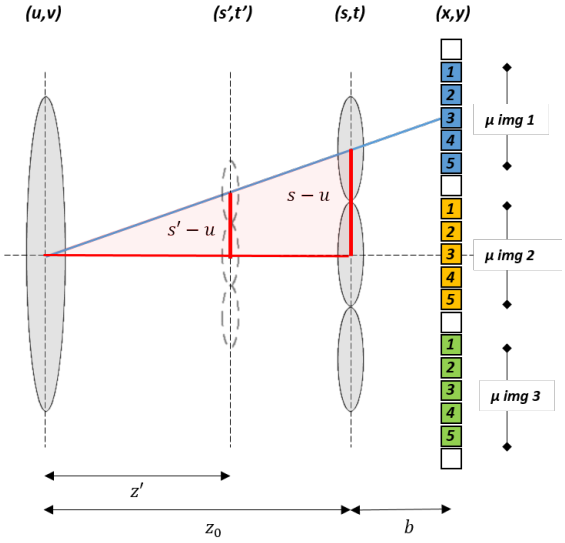

Figure 3.1: Coordinates transforming in virtual refocusing plane: The blue line is an arbitrary light ray captured by the plenoptic camera, intersecting the ML and the MLA plane at u and s, respectively. For a virtual plane at z', the intersection of the ray with the virtual plane can be found by the similarity between the red triangles.

Figure 3.2 displays the refocusing results from the raw light field image in figure 2.5 (b), which are reconstructed based on the equation 3.2. The raw light field image was taken of a transparent ruler and the business card behind it. The image of the business

card formed by the ML was in focus in the MLA plane. The ruler was closer to the ML than the business card. From the equation 3.2, the integral direction at z' is given by

$$\frac{\Delta s'}{\Delta u} = 1 - \alpha \tag{3.3}$$

The inverse of the equation explains the slope variation of the points at different depth in u-s phase space shown in the figure 2.8. When the slope is converging to infinity ($\alpha = 1$), namely integrating vertically in phase space, we reconstruct the image focused at the plane of the MLA. When the slope is positive ($\alpha < 1$), we refocus to the virtual plane closed to the ML before the MLA. In reverse, when the slope is negative ($\alpha > 1$), we refocus to the virtual plane farther to the ML after the MLA.

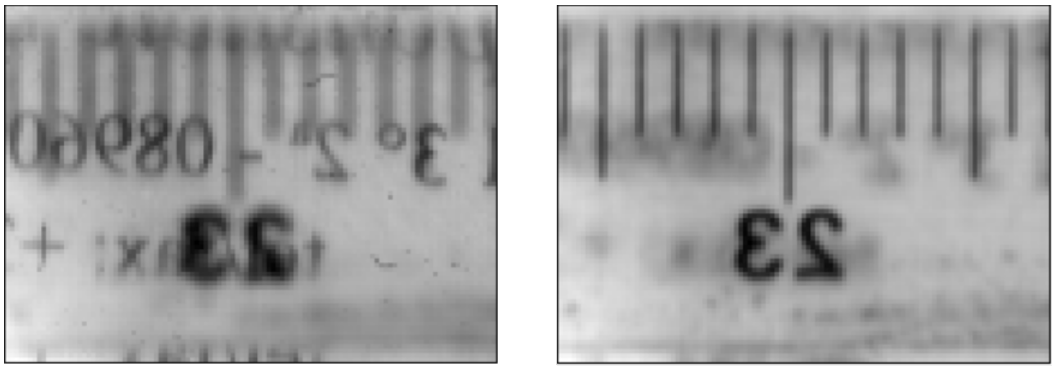

(a) **(b)**

Figure 3.2: Refocused images rendered based on the equation 3.2: (a) refocuses on the business card behind a transparent ruler rendered with $\alpha = 1$, while (b) focuses on the scale of the ruler rendered with $\alpha = 1.73$. Both reconstructed images have 79×109 pixels, the same as the microlens number used in the acquisition.

The integral direction in the phase space is visualized in the EPIs mentioned in the section 2.7. The integral direction is related to the slope of the linear structure in the EPI. The linear structure is formed by the disparity in s from the adjacent sub-aperture images along adjacent viewpoints represented by the local pixel position in micro-image p ($p = 1, 2, 3, 4, 5$ in the schematic sketches like figure 3.3). Through the similarity of

the red triangles between the MLA plane and the detector plane, illustrated in figure 3.3, the slope of the linear structure is given by

$$\frac{\Delta s}{\Delta p} = \frac{z_0 - z'}{b} \tag{3.4}$$

Furthermore, considering the similarity of the triangles on the two sides of the s'-t' plane at depth z' in figure 3.3, Δp and Δu has the relationship such that

$$\Delta p = \frac{b\Delta u}{z'} \tag{3.5}$$

Substituting this equation into the equation 3.4, we can obtain

$$\frac{z'\Delta s}{\Delta u} = z_0 - z' \tag{3.6}$$

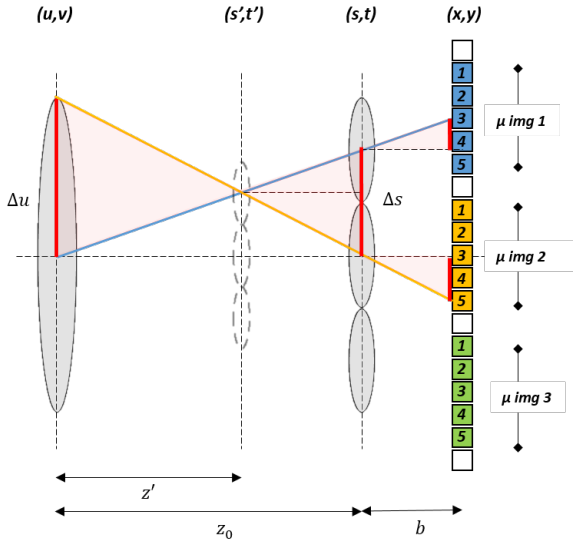

Figure 3.3: The geometric relationship between Δu, Δs and Δp: The blue and yellow lines are two rays from different viewpoints but crossing at the same point in the virtual refocusing plane. The two red triangles formed by the rays with the ML plane and the MLA plane are similar, and similar to the ensemble of two small triangles between the MLA and the detector.

Dividing the both sides of this equation by z_0, with $\Delta s' = \alpha \Delta s$, we finally end up with the same equation as equation 3.3.

$$\frac{z'}{z_0}\frac{\Delta s}{\Delta u} = \frac{z_0 - z'}{z_0} \tag{3.7}$$

$$\frac{\Delta s'}{\Delta u} = 1 - \alpha$$

The derivation from the equation 3.4 to the equation 3.7 mathematically interprets the relation between the integral direction in phase space and the slope of lines in the EPI. Meanwhile, the slope of lines in the EPI reveals the physical meaning of the integral direction in phase space. Let us consider two points that have the same size of one pixel but at different depths. These two points thus become two lines with different slopes in the schematic of EPI (see figure 3.4). Only when we integrate the EPI with the appropriate direction, we can reconstruct the point with the focused size of one pixel; if not, the point in the reconstructed image will become wider like going out of focus.

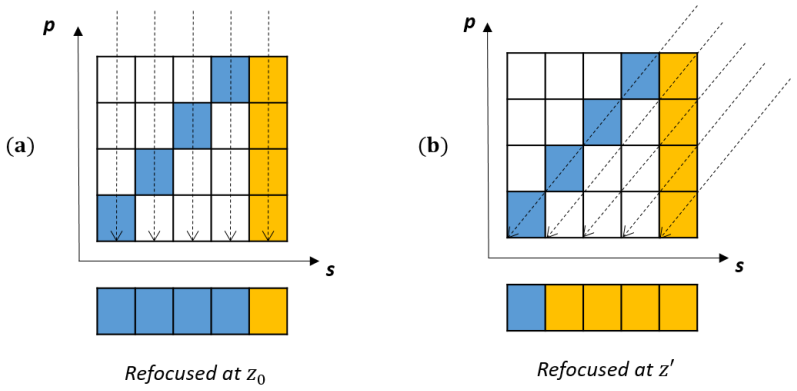

Figure 3.4: Integral direction meaning in EPI: The blue and yellow squares represent two points with the size at focus of one pixel but at different depths. They formed two lines with different slopes in the schematic of EPI. The slope is related to the depth of the point. (a) and (b) integrate the EPI with the slopes of the yellow and the blue lines, resulting in two reconstructed images focused on the yellow and blue points, respectively. The dashed arrows indicate the integral direction. Only with the appropriate slope, the point at the corresponding depth can be reconstructed back to its size at focus, while points at other depths become wider and blurred.

3.2.2 Back propagation method

Since the plenoptic image records the spatial and angular information of every light ray, the more intuitive refocusing method is to propagate every ray back to the target reconstruction plane. Consider each pixel on the photosensor plane as a ray noted by the vector $\begin{bmatrix} x \\ \theta \end{bmatrix}$, and note the outcome of back propagation to a virtual plane at z' as $\begin{bmatrix} x' \\ \theta' \end{bmatrix}$. x and θ are the position and angle coordinates of each pixel in a plane.

The transformation of the rays can be mathematically performed by the ABCD ray transfer matrix under paraxial approximation. From the virtual plane to the photosensor, the rays propagate a distance $z_0 - z'$ in free space, then pass through the microlens modeled as thin lens with a focal length f_2 (thin lens model) or as a pinhole (pinhole model), and travel another distance b in free space, yielding the transfer matrix T

$$T = \begin{bmatrix} 1 & b \\ 0 & 1 \end{bmatrix} L \begin{bmatrix} 1 & z_0 - z' \\ 0 & 1 \end{bmatrix}$$

$$where\ L = \begin{cases} \begin{bmatrix} 1 & 0 \\ -\frac{1}{f_2} & 1 \end{bmatrix} & thin\ lens\ model \\ \begin{bmatrix} 1 & 0 \\ 0 & 1 \end{bmatrix} & pinhole\ model \end{cases} \tag{3.8}$$

Refocusing the plenoptic image back to the virtual plane is the reverse process of the above propagation and is thus expressed as

$$\begin{bmatrix} x' \\ \theta' \end{bmatrix} = T^{-1} \begin{bmatrix} x \\ \theta \end{bmatrix} \tag{3.9}$$

where T^{-1} is the inverse of T.

In addition, each ray actually represents the small range of pixel size d_p on the detec-

tor, which will become the range of $\frac{(z_0-z')}{b}d_p$ in the reconstructed plane. The image refocused at z' is reconstructed by integrating the rays with different directions u' but arriving within the range of $\frac{(z_0-z')}{b}d_p$ around the same position s'.

From the same raw light field image used in figure 3.2, the images refocusing on the planes of the business card and the ruler reconstruct by the ABDC ray transfer matrix under thin lens and pinhole models are shown in figure 3.5. The images in the upper and lower row are rendered under pinhole model and thin lens model, respectively.

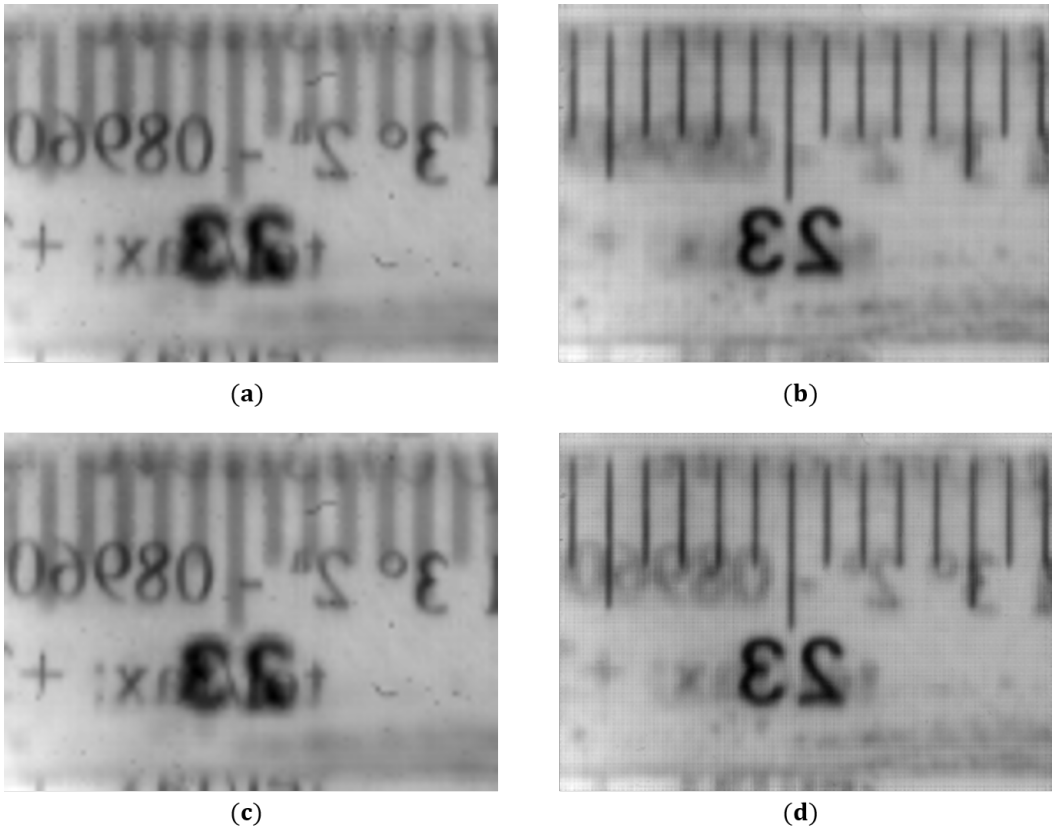

Figure 3.5: Refocused images rendered based on the equation 3.9: (a) and (b) are reconstructed under pinhole model, whereas (c) and (d) are reconstructed under thin lens model. The left and right column images respectively refocus on the business card and the ruler. (a) and (c) contains 79×109 pixels, which is equal to the microlens number, while (b) contains 147×201 pixels and (d) contains 203×279 pixels, much more than the microlens number.

Compared with figure 3.2, the images refocusing on the plane of the business card reconstructed by two different methods, integral and back propagation, have the same qualities and the same pixel numbers. But in the plane of the ruler, we can observe a remarkable improvement in the image quality due to the increase of the pixel number in the image rendered by the ABCD ray transfer matrix. Because unlike the integral method, which considers only the centers of the microlens as the refocused points, the back propagation method takes into account the intersections of all the rays with the virtual plane. In addition, the more accurate thin lens model lead to a growth of the pixel number and an enhancement of the image quality compared to the pinhole model.

Figure 3.6 (a) illustrates more visually the differences between these two methods with a simplified plenoptic camera consisting of three microlenses modeled as pinhole and five pixels in each microlens image.

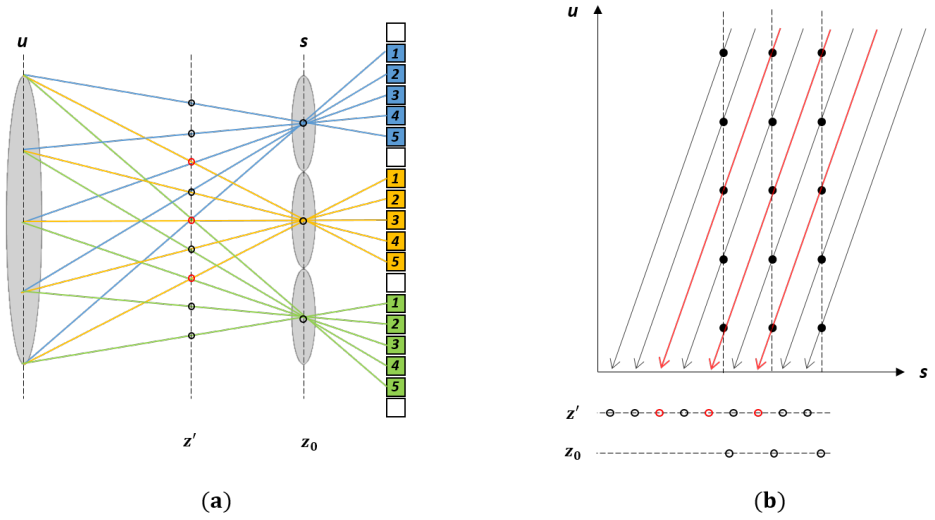

(a) (b)

Figure 3.6: Integral method vs. back propagation method with pinhole model: (a) the red spots represent the centers of microlens in a virtual plane at z', which are considered as the refocused points in the integral method. The black spots, the other intersections of rays with the plane at z', are the additional pixels complemented by the back propagation method for the same reconstruction plane. (b) interprets this difference in the phase space. The red and black arrows represent the integration along the direction corresponding to the plane at z', explaining the formation of the red and black spots in (a) in the phase space, respectively. The back propagation method will reconstruct the same number of pixels as the integral method only with the vertical direction, i.e. in the MLA plane.

For a certain virtual plane at z', the red spots in the figure 3.6 (a) represent the pixels in the image reconstructed with the integral method, and the black spots are the extra pixels complemented by the back propagation method in the reconstructed image. It is worth noting that the intersections of the rays with a virtual plane at z', which we are able to reconstruct, exceed the microlens number, except for the plane of the MLA at z_0. Figure 3.6 (b) interprets this fact in the phase space with the same model and the reconstruction plane in figure 3.6 (a).

In the phase space, the back propagation method is also equivalent to an integration along a direction depending on the reconstruction depth. From the equation 3.9 under pinhole model, we can derive

$$\begin{bmatrix} x' \\ \theta' \end{bmatrix} = \begin{bmatrix} 1 & -(z_0 - z' + b) \\ 0 & 1 \end{bmatrix} \begin{bmatrix} x \\ \theta \end{bmatrix} \tag{3.10}$$

As light ray travels in straight line and its propagation direction does not change through a pinhole, $\begin{bmatrix} x \\ \theta \end{bmatrix}$ and $\begin{bmatrix} s \\ u \end{bmatrix}$ have the relationship such that

$$\begin{bmatrix} x \\ \theta \end{bmatrix} = \begin{bmatrix} 1 & -\frac{b}{z_0} \\ 0 & -\frac{1}{z_0} \end{bmatrix} \begin{bmatrix} s \\ u \end{bmatrix} \tag{3.11}$$

The minus sign between θ and u originates from the inversion of the coordinates on the two sides of pinhole. Rewriting x' in equation 3.10 in terms of s and u, we obtain

$$x' = s + \frac{z_0 - z'}{z_0} u \tag{3.12}$$

Thus, the integral direction in the phase space is given by

$$\frac{\Delta x'}{\Delta u} = \frac{z_0 - z'}{z_0} = 1 - \alpha \tag{3.13}$$

We obtain the same relationship between the integral direction and the reconstruction depth as that derived from the integral method expressed in equation 3.3, but the in-

tegral result from the back propagation method is a function of x' instead of s' from the integral method. The arrows in figure 3.6 (b) indicate the integral direction corresponding to the virtual plane at z'. Every arrow leads to a reconstructed pixel in the virtual plane, represented by the spots below the phase space diagram. The red spots stand for the integration results of the integral method, whose amount is constant in any reconstructed plane and equals to the number of microlenses. The entirety of the red and black spots is the integration result of the back propagation method, the amount of which depends on the direction of integration related to the reconstructed plane. Only with the vertical direction, namely in the MLA plane, the integration of the back propagation method yields the same number of reconstructed pixels as the number of microlenses.

3.2.3 Patch method

Under the assumption that each ray is represented by a pixel on the detector, both of the two above mentioned methods reconstruct the post-refocused image in a virtual plane ray by ray. A more holistic reconstruction method, proposed in [36], considers a bundle of rays instead of a single one. For the sake of continuity, we illustrate the principle of this method with the same model and reconstruction plane in figure 3.6. In the virtual plane, a reconstructed point could be crossed by several rays with different directions, namely a fixed s' has more than one u'. Assuming that the plenoptic camera images a Lambertian surface that has the same radiance when viewed from any angle, each ray passing through the reconstructed point carries the same intensity information. Since the reconstructed image is a map of intensity, the plenoptic camera actually captures redundant rays for the angular information. In other words, for each point in the reconstructed image, we only need to consider one of the rays that pass through that point. Meanwhile, this kind of reconstructed points are also the junctions of sub-images of adjacent microlens images. Therefore, the reconstructed image can be decomposed to a set of sub-images of microlens images, the so-called patch. Instead of integrating the rays according to their position, we can render the image by merging the patches

like puzzle pieces (see in Figure 9 in [37]).

Each patch consists of $m \times m$ contiguous pixels cropped from the microlens image and its size m is related to the depth z' of the reconstructed plane. With the pinhole modeled MLA shown in figure 3.7 (a), the size of microlens image in the detector plane depends on the diameter of the ML d_1, the ML-MLA distance z_0 and the MLA-sensor b. Expressing the size of microlens image by the product of the pixel size d_p and the pixel number M, the relationship among the three variables is given by

$$d_1 = \frac{M d_p}{b} z_0 \tag{3.14}$$

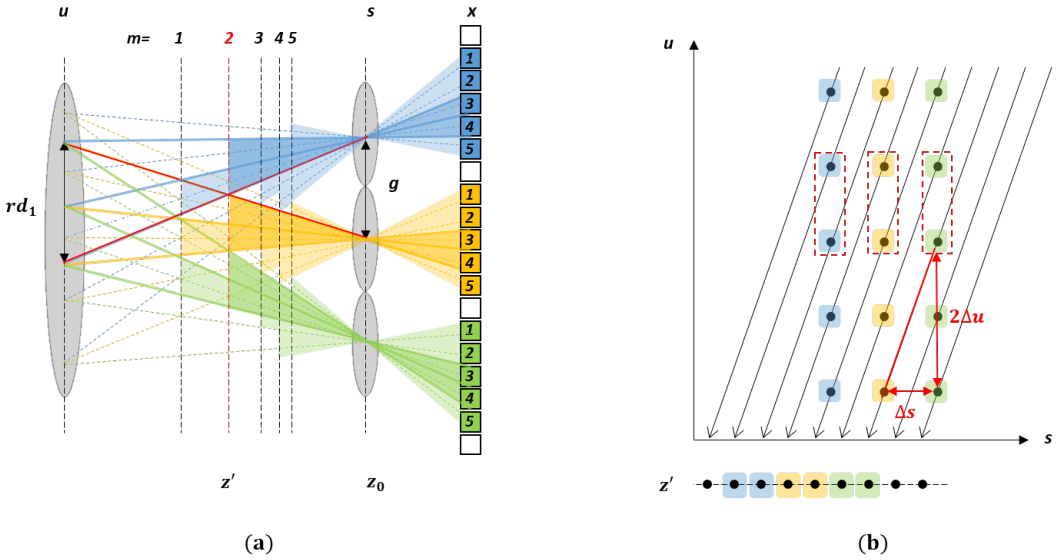

Figure 3.7: Patch reconstruction method: (a) The same model in figure 3.6 is used to illustrate the principle of the patch method. Reconstructing the same plane at z' in figure 3.6 is equivalent to merge the patches of two pixels cropped from each microlens image. The solid and dashed lines in blue, yellow and green are the borders of pixel and the central rays of pixel from the different microlenses. The dashed lines labeled with numbers indicate all the reconstructable planes with patches. The colored area represents the different patch sizes at different depths. (b) interprets the reconstruction of the plane at z' in (a) with patches in the phase space. The patches used in the reconstruction are marked by the red dashed squares. And the red triangle shows the relationship between the patch size m and the integral direction.

Choosing a patch size m ($m = 1, 2, ..., M$) corresponds to a partial aperture of the ML with the size of rd_1 and $r = \frac{m}{M}$. Figure 3.7 (a) depicts an example with $m = 2$, equivalent to the same reconstructed plane at z' in figure 3.6. If the patches of adjacent microlenses are exactly one next to another in the plane at z', then the aperture size in the ML plane and the spacing between two adjacent microlenses g in the MLA plane form two similar triangles enclosed by the red lines in figure 3.7 (a), yielding

$$\frac{g}{\frac{md_p}{b}z_0} = \frac{z_0 - z'}{z'} \tag{3.15}$$

Thus, the relationship between the patch size m and the depth z' is

$$z' = \frac{z_0}{1 + \frac{gb}{md_p}} \tag{3.16}$$

It is important to note that the above equation 3.16 is derived from the case that the virtual plane to reconstruct is between the ML and the MLA. For the case that the virtual plane is behind the MLA, the relationship between the patch size m and the depth z' becomes

$$z' = \frac{z_0}{1 - \frac{gb}{md_p}} \tag{3.17}$$

From the equation 3.16, we can find that a linear change in patch size m leads to a nonlinear change in depth z'. If we take patches of the same size in all microlens images to reconstruct a plane, the number of reconstructable planes is limited to the maximum pixel number of the microlens image M. Especially, the patch reconstruction method is not suitable to reconstruct the planes close to or in the ML plane and the MLA plane. With our simplified model in figure 3.7 (a), all the planes that we are able to reconstruct in this way marked by dashed lines labeled with numbers. And the colored areas indicate the patches of different sizes used in each plane. It is clear that there are reconstructable planes that are not covered by this method, and that the resulting images partially contain reconstructable points in a plane.

As $g = \Delta s$ and $\frac{d_p z_0}{b} = \Delta u$, the equation 3.15 can be rewritten to

$$\frac{\Delta s}{m \Delta u} = \frac{1 - \alpha}{\alpha} \tag{3.18}$$

Referring to the equation 3.18, choosing a patch size m is equivalent to fixing an integral direction in the phase space, which corresponds to a depth. Figure 3.7 (b) illustrates the patches used to reconstruct the plane $m = 2$ and the relationship between the patch size and the integral direction in the phase space.

Applying the patch reconstruction method on the same raw light field image that has been already processed by the other two methods, the reconstructed images are shown in figure 3.8. Figure 3.8 (a) and (b) reconstruct the two planes closest to the business card plane and the ruler plane, respectively. The refocusing results in figure 3.8 are not comparable to those in figure 3.2 and figure 3.5. As mentioned earlier, the reconstructable planes of the patch reconstruction method are limited and discrete, and the business card and ruler planes are not exactly included.

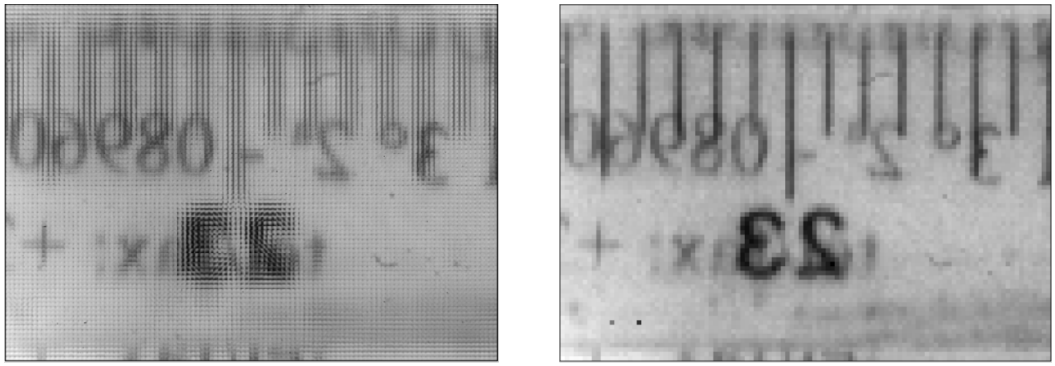

(a) **(b)**

Figure 3.8: Refocused images rendered by patches: (a) and (b) are the refocused images of the planes closest to the plane of the business card and the plane of the ruler. (a) and (b) are rendered with the patch size $m = 1$ and $m = 9$. Accordingly, (a) and (b) respectively contains 79×109 pixels and 981×711 pixels.

It is worth highlighting a special property of the patch reconstruction method, that choosing a patch size is equivalent to numerically change the Numerical Aperture (NA)

of the ML, and subsequently the Depth of Field (DoF). For the definitions and equations of NA and DoF, refer to appendix 7.A. In contrast to the other two methods, the change of focus in the reconstructed images with different patch sizes comes from the change of the DoF. A smaller patch size corresponds to a smaller NA, leading to a longer DoF, which brings all the planes within the DoF around the MLA into focus, rather than refocusing on a specific one.

This property of patch-reconstructed images is evident by comparing the insets in figure 3.9. The left and right column images are reconstructed by the integral method and the patch method, respectively.

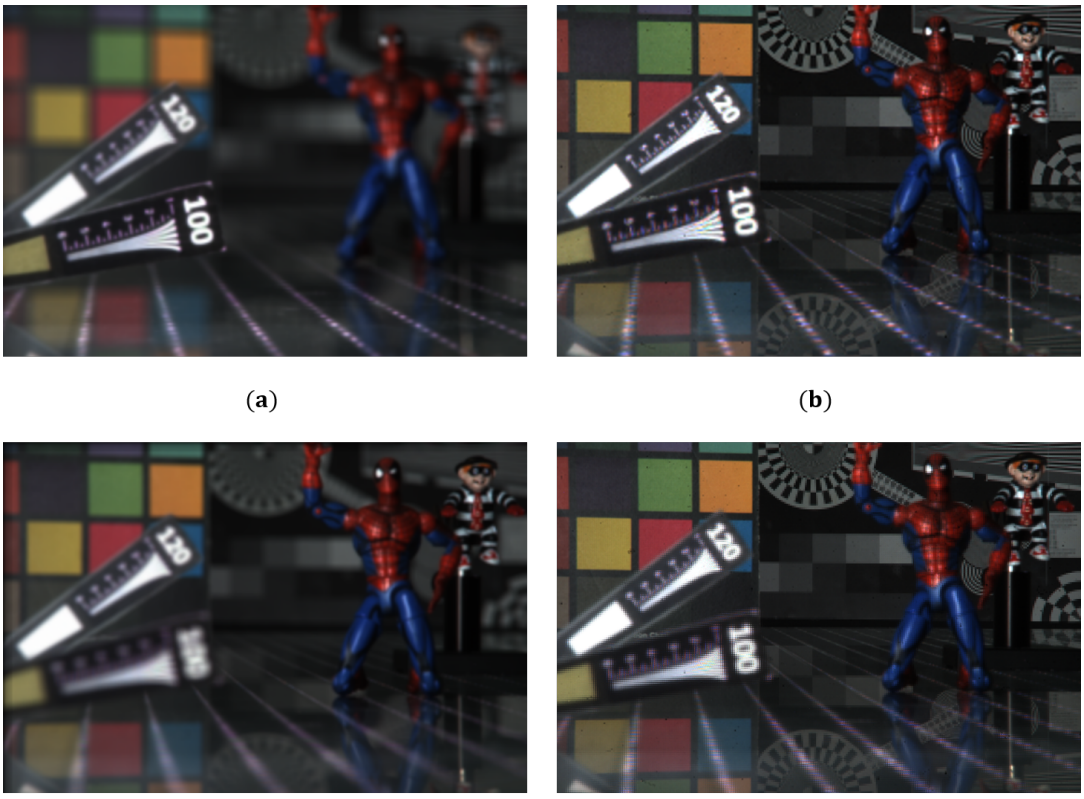

(**a**) (**b**)

(**c**) (**d**)

Figure 3.9: Property of patch-reconstructed image: The left and right column images are reconstructed by the integral method and the patch method, respectively. The top and bottom row images refocus on the same object, the label with the number 100 and the figurines. (b) and (d) are rendered with patch size $m = 1$ and $m = 3$. Original dataset is from [38].

The original dataset processed in figure 3.9 is acquired from [38]. The top and bottom row images refocus on the same object, the label with the number 100 and the figurines. Comparing the images in the same row of figure 3.9, we can find that only the target reconstruction objects, the label with the number 100 or the figurines, are in focus in the images (a) and (c) rendered by the integral method, while the objects within a certain DoF are all clear and sharp in the patch-reconstructed images (b) and (d). On the other hand, we can note that (d) has a shorter DoF than (b), because (d) is reconstructed with larger size patch than (b), corresponding to a larger NA. The raw light field image used in figure 3.9 is taken from [39].

3.3 Depth estimation

The previous section has discussed how to reconstruct the post-refocused images from the light field image, which are still two-dimensional representations of the scene. In order to create 3D model of the scene, it is necessary to estimate the third dimension of space, the depth. This section will briefly describe several depth estimation methods developed specifically for light field images. We begin with two basic categories of methods used in the later work: focal stack-based approach and EPI-based approach.

- **Focal stack-based approach**

Focal stack is a series of images focused at multiple planes. In conventional photography, focal stack is captured by physically changing the imaging distance or the focal distance of the optics. Instead of exposure stack, light field image allows us to numerically render a focal stack after a single acquisition. As previously illustrated, each reconstructed image of the numerical focal stack is rendered with a certain depth. For the object in focus at a certain depth, we can observe the evolution of its focus level along the depth in the focal stack. The sharpest image of the object (the most focused image) should be found in the focal stack frame reconstructed with the proper depth. Therefore, the corresponding depth of the in-focus focal stack frame of the object can be used as a clue to the real object depth. The depth estimation of the object is then converted to the focus level measurement of the object in the focal stack.

The focus level measurement has been widely addressed and covered in autofocusing and edge detection field, and a variety of algorithms and operators have been proposed. The straightforward and widely used methods are based on the variance of grayscale pixel intensity [40]. The focus level of the object can also be reflected by the contrast with its neighborhood [41]. Due to the fact that in-focus image of the object has sharp edge, the object focus level can be evaluated by the rapidity of intensity change at the edges, quantified by the gradient of the edges. Such measurements can be implemented on the basis of the Laplace, Sobel and Scharr operators[40] [42] [43]. In addition to the methods in the spatial domain, the sharpness of the edge can also be analysed from a frequency perspective by wavelet transform as investigated in [44] [45]. Under the assumption that an image is a result of the convolution between the Point Spread Function (PSF) of the imaging system and the ideal image of the object, the focus level of the object can be extract by estimating the width of the PSF[46]. More methods have been reviewed and compared in [47]. In practical, the results of several different methods are commonly considered and synthesized to ensure the robustness and accuracy of the depth.

- **EPI-based approach**

Even without reconstructing the images refocused on different planes from the light field image, the depth information of the scene are still contained in the slopes of the linear structures in the EPI due to the dense angular sampling, as explained in the previous section. Thus, another important category of depth estimation methods takes advantage of this property of EPI and measure the slopes of the linear structures from different perspectives.

As line detection is a fundamental task in the fields of image processing and computer vision, various algorithms have been developed such as Structure Tensor and Hough Transform. The application of these two classical algorithms on light field EPIs are respectively described in [48] and [49]. The combination of these two algorithms allows to achieve a better result [50].

The slope of the linear structure in the EPIs can also be detected by the matching cost aggregation method, whereby the slope measurement becomes the minimization of

matching cost in different directions [51] [52]. Although the definition of the matching cost function varies in different literature, it is mainly based on the consistency of the pixels on the same line in terms of grayscale values, colors, derivative and gradient. Another similar method measures the slope of the linear structures by shearing EPI with different angles, and the optimal angle of each structure is then evaluated and selected via the defocus and correspondence response [53].

The above methods are dedicated to provide a better detection method for the linear structure slope, using only the horizontal and vertical EPIs of the light field image. Other methods further improve the accuracy and robustness of the depth estimation by exploiting multi-orientation EPIs, no longer limited to horizontal and vertical directions [54] [55]. These methods increase the use of light field data and in the meantime deal with the occlusion issue, which is the reason they are usually named as occlusion-aware methods.

Instead of working on one of these two categories approaches, Lin et al. proposed an iterative optimization framework that synthesizes the results of both methods, resulting in better noise tolerance [56]. Besides these two categories approaches, the block matching techniques originating from the stereo vision are also compatible to the multi-view image rendered from the light field image, as investigated in [57]. Jeon et al. brought the block matching method between sub-aperture images to sub-pixel accuracy by phase shift theory [58]. At present, there is a great trend to adopt machine learning algorithms into the depth estimation of light field images, such as convolutional neutral networks, deep learning, and sparse coding [59] [60] [61].

3.4 Conclusion

After the introduction on how to capture the light field data, we focused on, in this chapter, the reconstruction $3D$ information from the acquisition. We reviewed and summarized the various approaches developed in previous literature for different light field image processing, such as calibration, refocusing and depth estimation. In particular, we focused on three basic light field refocusing algorithms. We mathematically

illustrated the interconnection between the three algorithms and compared the differences in their refocusing results. Meanwhile, we also showed the relationship between different representations of light field data. The studies on the post numerical processing of light field data in this chapter contributes to a better understanding of the light field principle.

Chapter 4

Numerical Study of Fresnel Zone Plate for X-ray Light Field Imaging System

4.1 Background

Existing light field imaging systems have been developed for the visible light range. The purpose of this thesis is to extend such a system to the X-ray range and to build up a prototype. Visible light and X-rays, as both electromagnetic waves, propagate in space in the same way. However, due to much higher photon energy of X-rays, the real part of the complex refractive index of X-rays is close to unity[62]. In other words, when X-rays interacts with matter, it tends to penetrate and be absorbed, rather than being redirected. This property makes it much more difficult to manipulate X-rays with respect to visible light. Therefore, to build a X-ray light field imaging system, we need to search the adapted optical components for the ML and the MLA.

Based on refraction, reflection and diffraction, a variety of optics have been designed to deal with X-ray redirection and focusing, such as refractive X-ray lenses, X-ray mirrors and Fresnel zone plates. In particular, Fresnel zone plate (FZP) has been widely used in X-ray microscopes built for various applications, such as the soft X-ray microscopes for biological imaging [63] [64] [65], the scanning transmission X-ray microscopy for atmospheric aerosol research [66] and the scanning X-ray fluorescence microscopy for trace analysis of materials [67]. The structure and characteristics of

FZP will be described in detail in the following sections. One of the advantages of the FZP is that it is compact and follows the imaging equation of a visible lens. A more important advantage of FZP is its demonstrated ability to achieve high spatial resolution image [68]. FZP seems to be a suitable optics to implement the concept of light field imaging system in X-ray range. Keeping the common configuration of the visible light field system unchanged, we prototyped a X-ray light field system by replacing visible refractive lenses with FZP. Figure 4.1 illustrates the principal structure of the FZP based X-ray light field system.

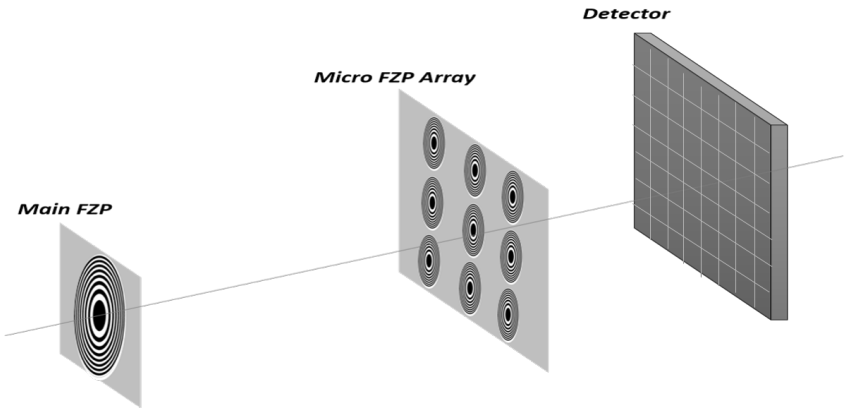

Figure 4.1: Principal structure of a FZP based X-ray light field system: Maintaining the same structure as the visible light plenoptic camera, the refractive main lens and the refractive lens array are respectively replaced by a main FZP and a micro-FZP array.

Due to different application contexts, research efforts on FZP imaging performance have been made in different aspect, such as efficiency [69], resolution [70] [71] and working energy range [72] [73]. As mentioned earlier, a light field system relays on micro-scale lens array to realize a dense spatial and angular sampling of the scene. Under this context, our goal is to design a dense FZP array. Accordingly, the size of each FZP in the array is quite small. One problem arises that the limited size of FZP leads to a low number of zones, which might reduce its imaging performance. We will discuss in more detail the geometry and properties of the FZP in the following sections. In order to design a dense FZP array for X-ray light field system, we will numerically investigate

the impact of FZP number of zones on its imaging performance, especially the case of very small number of zones.

4.2 Fresnel zone plate structure

FZP is a diffractive optic that conventionally consists of alternating transparent and opaque zones. This allows the incident X-rays constructively interfere at the desired focus. A schematic diagram of a conventional FZP is shown on the left and the optical path on the right in figure 4.2.

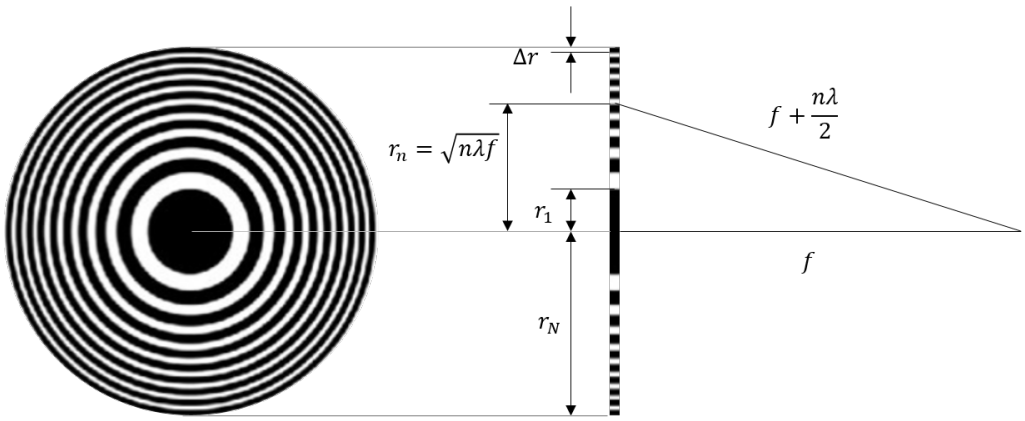

Figure 4.2: Fresnel zone plate: Schematic diagram of FZP with alternatively transparent and opaque zones is shown on the left. And the optical path of rays passing through the FZP on side projection is displayed on the right.

In order to maximize the interference at a designed focal length f on the optical axis, the optical path difference between the ray passing through the center and that passing through the nth zone should be an integer multiple n of the half-wavelength $\frac{\lambda}{2}$ at f (see the right part of figure 4.2). Thus, the radius of nth zone transition ring r_n and the f satisfy the relationship that

$$\sqrt{f^2 + {r_n}^2} - f = n\frac{\lambda}{2} \tag{4.1}$$

where n is the sequence number of zone. Rewriting equation 4.1, all the zone boundary are given by

$$r_n = \sqrt{nf\lambda + \frac{n^2\lambda^2}{4}},\ n = 1, 2, ..., N \tag{4.2}$$

The total size of FZP depends on the zones number N. For the FZP of low numerical aperture (focal length much larger than the radius), which is usually the case for the FZPs in X-ray range, equation 4.2 can be simplified to

$$r_n = \sqrt{nf\lambda},\ n = 1, 2, ..., N \tag{4.3}$$

We can derive the width of each zone from the equation 4.3

$$r_n - r_{n-1} = (\sqrt{n} - \sqrt{n-1})\sqrt{f\lambda} \tag{4.4}$$

The width of zone decreases with the increase of the number of zone n. Although the tone of adjacent zones alternates, the tone of the first zone is arbitrary and could be transparent or opaque, which will not affect the FZP performance. The outermost zone of width Δr is the finest structure of FZP and also an important parameter of FZP. Rewrite equation 4.4 for the outermost two zones N and $N-1$ as

$${r_N}^2 - {r_{N-1}}^2 = f\lambda \tag{4.5}$$

Substituting $r_{N-1} = r_n - \Delta r$ in equation 4.5, it gives

$$2r_N\Delta r - \Delta r^2 = f\lambda \tag{4.6}$$

Since $\Delta r \ll r_N$, the second order term of Δr is neglectful in equation 4.6, yielding

$$\Delta r = \frac{f\lambda}{2r_N} = \frac{\lambda}{2NA} \tag{4.7}$$

The radius and NA of FZP can be both written in term of Δr as $r_N = \frac{f\lambda}{2\Delta r}$ and $NA = \frac{\lambda}{2\Delta r}$, respectively. Moreover, according to the Rayleigh criterion, the resolution is defined as $0.61\frac{\lambda}{NA}$. Substituting the NA of FZP, the theoretically achievable resolution of FZP (the smallest separation to distinguish two individual points) Res_{FZP} can be expressed in terms of Δr as

$$Res_{FZP} = 1.22\Delta r \tag{4.8}$$

From the above derivation about FZP structure, we can see that the width of the outermost zone Δr determines the resolution of FZP. The FZP with a larger zones number N has a smaller Δr, then it is advantageous for high quality imaging. However, the large zones number and nanoscale zone width bring challenges to the FZP fabrication. Furthermore, as a diffractive optics, the focal length of FZP greatly depends on the wavelength. Thus, for precise imaging, FZP requests a narrow spectral bandwidth of the source, i.e., $\frac{\Delta\lambda}{\lambda} \leq \frac{1}{N}$ [74].

4.3 Imaging property of Fresnel zone plate

Using a FZP of focal length f for imaging, the relationship between the object distance q and the imaging distance p approximately is

$$\frac{1}{q} + \frac{1}{p} = \frac{1}{f} \tag{4.9}$$

The equation 4.9 can also be derived from the important property of FZP, that is, the difference of optical path between neighbouring zones successively adds $\frac{\lambda}{2}$. For the complete derivation, refer to the literature [74]. The equation also suggests that a FZP can be used as an ordinary visible lens for imaging. However, there is a significant difference between the FZP imaging and the visible lens imaging, and that is FZP produces multi-order images. The interference of rays passing through transparent zones occurs not only when the optical path difference is $n\frac{\lambda}{2}$, but also an integer times of it, i.e., $mn\frac{\lambda}{2}$. The integer m is also called diffraction order, $m = 0, \pm1, \pm2, ...$
The equation 4.9 is developed from the first order diffraction ($m = 1$). Following the same derivation of equation 4.9, the corresponding high order focal length f_m can be given in terms of the first order focal length f

$$f_m = \frac{f}{m},\ m = 0,\ \pm1,\ \pm2, ... \tag{4.10}$$

The equation 4.10 indicates that FZP has multiple foci and forms multi-order images. The zeroth order ($m = 0$) is the direct beam without diffraction, and the first order

focal length is equal to the designed focal length. Passing through a FZP, the positive-order beams converge, while the negative-order beams diverge. Figure 4.3 illustrates the optical paths of different orders resulting from a parallel beam passing through a FZP.

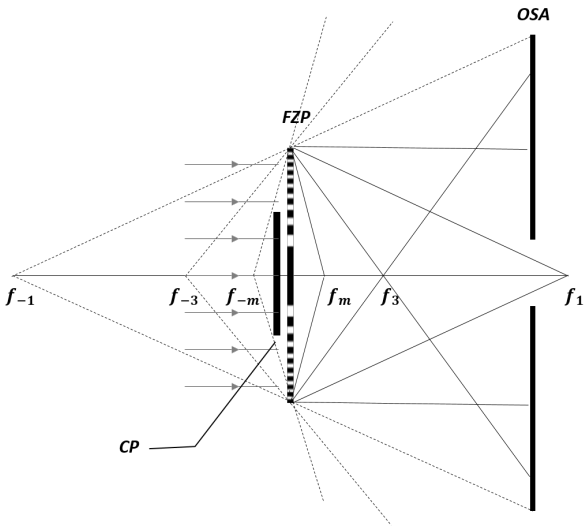

Figure 4.3: FZP imaging property: The figure illustrates the optical paths of a parallel beam passing through the FZP. As a diffractive optics, FZP diffracts the beam to different orders. The positive order beams converge, while negative order beams drawn in dotted line diverge. And the zeroth order beam is not diffracted. The accompanying center stop (CP) and order sorting aperture (OSA) are also shown in the figure, in the case of imaging with the first order of FZP.

Diffraction of all the orders occurs simultaneously but with different intensity. For a conventional FZP of alternatively transparent and opaque zones, the diffraction efficiencies of various orders with respect to the incident beam are

$$\eta_m = \begin{cases} \frac{1}{4} & \text{if m=0} \\ \frac{1}{m^2\pi^2} & \text{if m is odd} \\ 0 & \text{if m is even} \end{cases} \tag{4.11}$$

It must be firstly pointed out that 50% of the incident beam is blocked by the opaque

zones. 25% of the incident beam is transmitted forward by the zeroth order without diffraction. The intensity of odd orders decreases sharply as order m increases, about 10% for the first order, about 1% for the third order, etc. In particular, the even orders do not contribute to the energy transmission and will not be present after FZP.

Due to the multiple foci property, when using the FZP for imaging purpose, it is usually accompanied by blocker to eliminate the effects of other orders. The blocker typically consists of two parts: the center stop (CP), a disc to block the major disturbance from the direct flux (the zeroth order); and the order sorting aperture (OSA), a small enough diaphragm near the focus of the order of interest to block all the other orders.

4.4 Simulation method

The imaging properties of FZP can be well analyzed by the scalar diffraction theory. Figure 4.4 represents a generalized schematic of a FZP optical system.

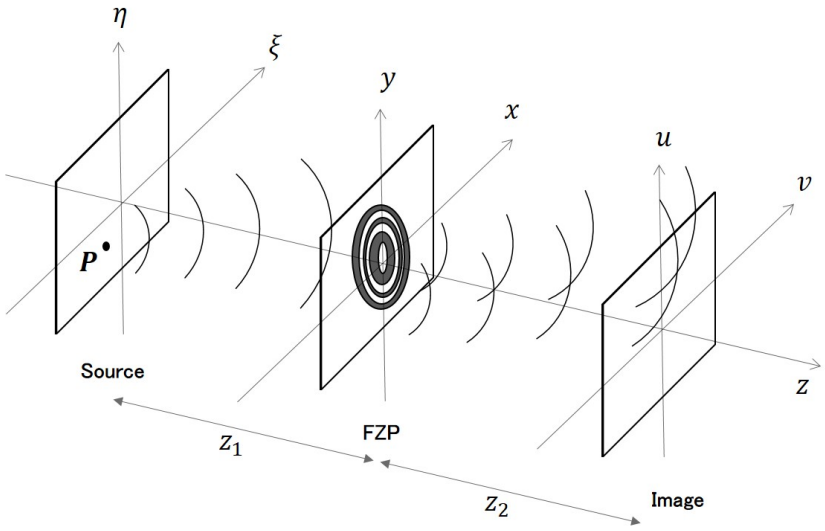

Figure 4.4: Generalized schematic of Fresnel Zone Plate (FZP) optical system: the point source $\boldsymbol{P}$ on the plane (ξ, η) emitting a spherical wave is intercepted and diffracted by the FZP on the plane (x, y). The image of the source is formed on the plane (u, v). z_1 and z_2 represent respectively the source–FZP distance and the FZP–image distance.

Considering a monochromatic point source P (ξ,η), whose wave field distribution at a distance r is given by

$$U_0 = \frac{e^{ikr}}{r} \tag{4.12}$$

where $r = \sqrt{{z_1}^2 + (x-\eta)^2 + (y-\xi)^2}$.

Under the paraxial approximation, keeping the first two terms of the binomial expansion of r, r becomes

$$r = z_1 + \frac{(x-\eta)^2}{2z_1} + \frac{(y-\xi)^2}{2z_1} \tag{4.13}$$

Assuming the point source illuminates the entire FZP at distance z_1 on the plane (x, y), neglecting a pure phase factor, the incoming wave field U_{zp} at the plane of FZP becomes

$$U_{zp} = \frac{1}{i\lambda z_1} \exp\left\{\frac{ik}{2z_1}[(x-\xi)^2 + (y-\eta)^2]\right\} \tag{4.14}$$

After passing through the FZP, the new wave field U'_{zp} distribution can be written as

$$U'_{zp} = t(x,y) \times U_{zp} \tag{4.15}$$

where $t(x, y)$ is the transmission function of the FZP.

Then according to Huygens–Fresnel principle, at a distance z_2 behind the FZP ($z_2 \gg x, y$ and $z_2 \gg u, v$), the wave field distribution in the image plane (u, v) is given by summing all the secondary sources propagation from the FZP plane

$$U_{zp} = \frac{1}{i\lambda z_2} \iint U'_{zp} \times \exp\left\{\frac{ik}{2z_2}[(u-x)^2 + (v-y)^2]\right\} dxdy \tag{4.16}$$

On account of the linearity of the optical system [75], we can find the impulse response $h(\xi, \eta, u, v)$ of the FZP, also known as the Point Spread Function (PSF), by setting $\xi = \eta = 0$ in the above expression. The PSF is thus expressed as

$$\begin{aligned} h(0,0,u,v) = {} & \frac{z_2}{z_1} \exp\left[\frac{ik}{2z_2}(u^2+v^2)\right] \\ & \times \iint t(x,y) \exp\left[\frac{ik}{2}\left(\frac{1}{z_1}+\frac{1}{z_2}\right)(x^2+y^2)\right] \exp\left[-\frac{ik}{z_2}(ux+yv)\right] dxdy \end{aligned} \tag{4.17}$$

The integral term of the impulse response expression can be considered as a Fourier transform with appropriate substitution of variables, yielding

$$h(0,0,u,v) = \frac{z_2}{z_1}\exp\left[\frac{ik}{2z_2}(u^2+v^2)\right] \times \mathcal{F}\Big\{t(\lambda z_2 x', \lambda z_2 y')\exp\left\{\frac{ik}{2}\left(\frac{1}{z_1}+\frac{1}{z_2}\right)\left[(\lambda z_2 x')^2+(\lambda z_2 y')^2\right]\right\}\Big\} \quad (4.18)$$

with $x' = \frac{x}{\lambda z_2}$, $y' = \frac{y}{\lambda z_2}$.

The transformation of the expression in the previous step allows performing an efficient numerical calculation with the help of Fast Fourier Transform (FFT) algorithm.

Above we derive the amplitude impulse response of FZP in the image plane from a single point source. The image formed can be considered as the integrated result of the amplitude impulse response generated by each object point in the image plane. Thereby, the image $Img(u,v)$ can be obtained by the convolution of the image predicted by geometrical optics $img(u,v)$ with the impulse response $h(\xi,\eta,u,v)$ [76]. It is worth noting that the statistical relationship of the source in phasor amplitude influences the interaction of the amplitude impulse responses in the image plane, which then greatly affects the final image intensity distribution. The statistical relationship of the source in phasor amplitude is known as the coherence of the source. Here, we consider two extreme cases, the fully coherent case, where every source points vary in perfectly correlated way, and the opposite case fully incoherent. For the fully coherent case, the amplitude impulse responses of imaging system is linear in complex amplitude, whereas a fully incoherent is linear in intensity. Thus, the intensity distribution of image $Img(u,v)$ can be written as

$$Img(u,v) = \begin{cases} |h(\xi,\eta,u,v) \otimes img(u,v)|^2 & fully\ coherent \\ |h(\xi,\eta,u,v)|^2 \otimes |img(u,v)|^2 & fully\ incoherent \end{cases} \quad (4.19)$$

According to the convolution theorem, the equation 4.19 can be further converted to

$$Img(u,v) = \begin{cases} \mathcal{F}^{-1}\Big\{|\mathcal{F}\{h(\xi,\eta,u,v)\} \times \mathcal{F}\{img(u,v)\}|^2\Big\} & fully\ coherent \\ \mathcal{F}^{-1}\Big\{\mathcal{F}\{|h(\xi,\eta,u,v)|^2\} \times \mathcal{F}\{|img(u,v)|^2\}\Big\} & fully\ incoherent \end{cases} \tag{4.20}$$

This conversion reduces the complexity of the computation and allows greatly increasing the computation speed thanks to the use of FFT.

This method is flexible for the definition of FZP and the adjustment of imaging system structure, allowing to study the effects of different parameters on the FZP imaging performance.

4.5 Simulation sampling and parameter decisions

The core of the simulation of FZP imaging is the calculation of its PSF via the equation 4.18, which is a Fourier transform. In other words, the PSF generated in image plane is actually the Fourier transform of FZP structure. In practice, equation 4.18 is digitally calculated by Discrete Fourier Transform (DFT), a sampled Fourier transform. The use of discrete sequence to approximate continuous function introduces errors. We can compare the difference between DFT and FT with a rectangular window, which may be defined by

$$w(n) = \begin{cases} 1, & -n_0 \le n \le -n_0 + (K-1) \\ 0, & else \end{cases} \tag{4.21}$$

The length of the rectangular window is $K-1$ and sampled by K points, as shown in figure 4.5.

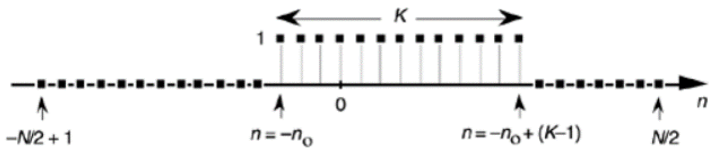

Figure 4.5: Rectangular window example: The rectangular window is defined via the equation 4.21.

The analytical result of the FT of $w(n)$ is equivalent to the sinc function,

$$FT\{w(n)\} \triangleq sinc(\frac{\pi m}{N}) = \frac{sin(\frac{\pi m}{N})}{\frac{\pi m}{N}} \tag{4.22}$$

The DFT of $w(n)$ is equal to

$$\begin{aligned} DFT\{w(n)\} &= \sum_{n=-n_0}^{n=-n_0+(K-1)} 1 * e^{\frac{-i2\pi nm}{N}} \\ &= e^{\frac{-i2\pi n_0 m}{N}} \sum_{0}^{K-1} e^{\frac{-i2\pi nm}{N}} \\ &= e^{\frac{-i2\pi n_0 m}{N}} \frac{1 - e^{\frac{-i2\pi Km}{N}}}{1 - e^{\frac{-i2\pi m}{N}}} \\ &= e^{\frac{-i2\pi n_0 m}{N}} \frac{e^{\frac{-i\pi Km}{N}}(e^{\frac{i\pi Km}{N}} - e^{\frac{-i\pi Km}{N}})}{e^{-\frac{i\pi m}{N}}(e^{\frac{i\pi m}{N}} - e^{-\frac{i\pi m}{N}})} \\ &= e^{\frac{-i2\pi n_0 m}{N}} e^{\frac{-i\pi(K-1)m}{N}} \frac{sin(\frac{\pi Km}{N})}{sin(\frac{\pi m}{N})} \end{aligned} \tag{4.23}$$

We can factor out linear phase terms from the above expression and get

$$DFT\{w(n)\} = \frac{sin(\frac{\pi Km}{N})}{sin(\frac{\pi m}{N})} \triangleq asinc_K(\frac{\pi m}{N}) \tag{4.24}$$

where $asinc_K(\frac{\pi m}{N})$ denotes the aliased sinc function [77]:

$$asinc_K(\frac{\pi m}{N}) = \frac{sin(\frac{\pi Km}{N})}{K * sin(\frac{\pi m}{N})} \tag{4.25}$$

The aliased sinc function 4.24 approaches the sinc function 4.22, as the sampling number goes to infinity, i.e. $\frac{\pi m}{N} \to 0$ [78].

Therefore, the accuracy of PSF depends on the sampling in the FZP plane. Assuming that we define a FZP plane of side length $L \times L$ in arbitrary units, sampled by $N \times N$

points, the sampling intervals Δ_s in x and y direction in the FZP plane are the same and equal to

$$\Delta_s = \frac{L}{N} \tag{4.26}$$

Then the sampling interval of equation 4.18 Δ' become

$$\Delta'_s = \frac{\frac{L}{N}}{\lambda z} \tag{4.27}$$

where z is the propagation distance between the FZP plane and the image plane. The inverse of the sampling interval Δ'_s in the FZP plane corresponds to the highest frequency f_{max} in the image plane,

$$f_{max} = \frac{1}{\Delta'_s} = \frac{\lambda z}{\frac{L}{N}} \tag{4.28}$$

Because the sampling number remains constant after DFT, the frequency interval Δ_f, which is also the sampling interval in the image plane, is

$$\Delta_f = \frac{f_{max}}{N} = \frac{\lambda z}{L} \tag{4.29}$$

The equations 4.26 and 4.29 imply that the sampling intervals in the FZP plane and the image plane Δ_s and Δ_f have opposite changing tendencies. High sampling in the image plane leads to low sampling in the FZP plane, and vice versa. To avoid aliasing and get a satisfactory simulation results, we need to pay attention to the choice of the side length L and the sampling number N in the FZP plane. The sampling intervals Δ_s and Δ_f should be able to describe the smallest detail in each plane, i.e. the outermost zone width in the FZP plane and the FZP resolution in the image plan. As discussed before, for a FZP, its outermost zone width is approximately equal to its resolution. Therefore, the simulation parameters L and N can be set by

$$\begin{aligned} \Delta_s = \Delta_f &= \Delta r \\ \frac{L}{N} = \frac{\lambda z}{L} &= \Delta r \end{aligned} \tag{4.30}$$

4.6 Simulation results

We simulated, using the method described in the previous section, FZP imaging in different cases. We first validated the method by verifying whether the simulation results conform to the basic properties of the FZP imaging. Then, we investigated the effects of several parameters on the image quality, such as the detection distance, the coherence of source and the number of zones of FZP. The following numerical results are all obtained with an X-ray source at $11keV$, and accordingly the wavelength is 1.127Å.

4.6.1 FZP multiple foci imaging

As described previously in the section 4.3, a distinctive feature of the FZP imaging is that FZP focuses the beam to multiple focal points and forms different orders images, due to its nature of diffraction grating. The focal length of each order f_m is given by the equation 4.10. According to the equation 4.10, for a parallel incident beam, the radii of different orders formed at the first focal length f have such relation that

$$R_m = \begin{cases} (m-1)R, \ m > 0 \\ (1-m)R, \ m \leq 0 \end{cases} \tag{4.31}$$

where R is the radius of FZP.

We can use this relationship 4.31 to validate the simulation method. Hence, we modeled a single point source situated at a distance of $100f$ to approximate the parallel beam. The beam passes through a thin FZP with focal length $f = 8.98\ cm$, radius $R = 20\ \mu m$ and number of zones $N = 40$, and then reaches on the detector located at f. The transmission function of the FZP in the equation 4.17 is defined as

$$t(r) = \begin{cases} 1, \ r_n < r < r_{n+1} \\ 0, \ else \end{cases} \tag{4.32}$$

where the n_{th} zone radius r_n refers to the equation 4.3.

Figure 4.6 (a) displays the resulting numerical image and its central intensity profile is

shown in (b). As in theory, different orders appear and overlap in the simulation result. The centre bright spot is the first order focus, which corresponds to the peak in the intensity profile. The disks with sharply decreasing intensity around the $1st$ focus, from the center towards the edge of the figure, are the $0th$ order, the $3st$ and $-1th$ orders and the $5th$ and $-3th$ orders, etc. Their radii measured from the simulation image are $20\mu m$, $40\mu m$, and $80\mu m$, respectively. Except the 1st order focal spot, the ratio of radii between $0th$, $3rd/-1st$, and $5th/-3rd$ order is 1:2:4. This ratio of radii between different orders measured from the simulation image agrees well with that calculated from the equation 4.31.

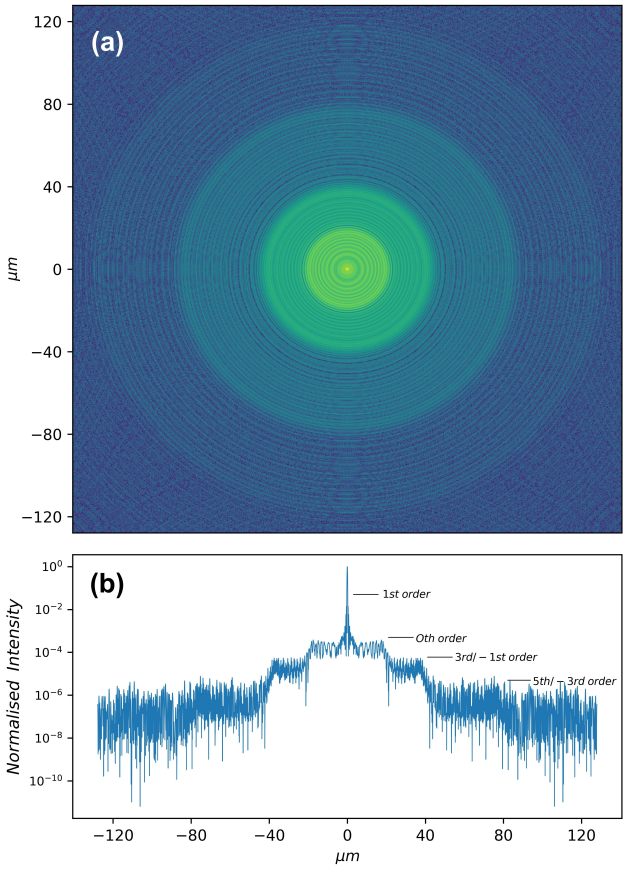

Figure 4.6: (a) False color image of the intensity distribution at the first focal plane of a FZP. The intensity is shown in logarithmic scale. (b) Central intensity profile of (a): the radii of 0th order, 3rd/-1st order, and 5th/-3rd order are, respectively, $20\mu m$, $40\mu m$, and $80\mu m$.

4.6.2 Point spread function of FZP

Recall that PSF is the impulse response of an optical system, mentioned in section4.4. The radius of PSF (the distance between the central maximum and the first minimum) can reflect the imaging performance of the optical system. A further validation test of the proposed simulation method has been achieved by comparing the PSF radius measured from the numerical output with the theoretically calculated value. For this simulation, a point source that emits a pure spherical wave is placed at $3f$ from the FZP. Accordingly, the detector is located in the image plane at $1.5f$. Keeping the same focal length of the FZP ($f = 8.98\ cm$), we performed a series of simulations with the number of zones varying from 5 to 200 and measured the PSF radius in each numerical result.

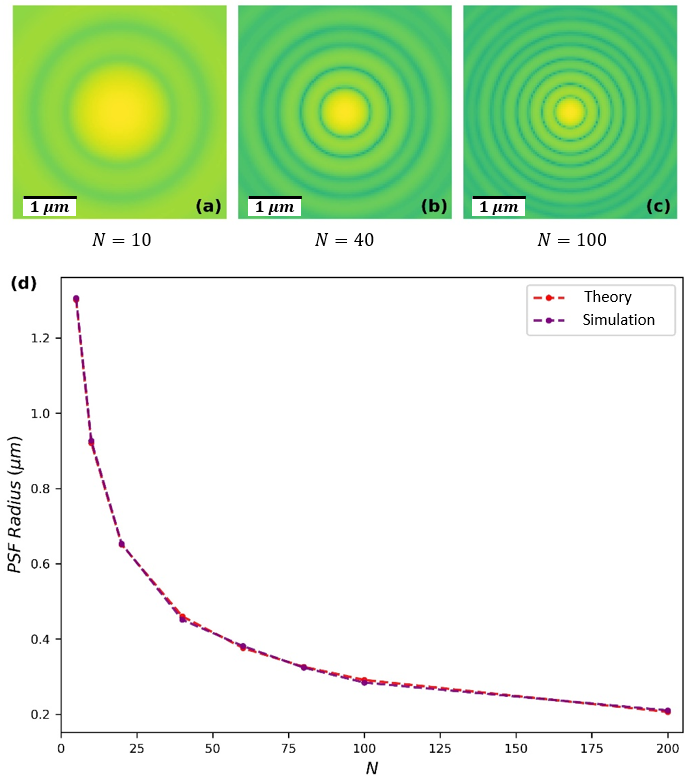

Figure 4.7: (a–c) False color images of simulated Point Spread Function (PSF) in logarithmic scale, when the number of zones N equals to 10, 40, and 100. (d) Theoretical and simulated PSF spot radius versus N.

Three example images of numerical outputs with the number of zones 10, 40 and 100 are displayed in figure 4.7 (a–c). The plot of PSF spot radius versus the number of zones N is displayed in figure 4.7 (d). The theoretical PSF spot radius calculated by the classical formula set by the diffraction theory (see the equation (4.33)) is reported and compared to the numerical results.

$$theoretical\ spot\ radius = \frac{1.22\lambda}{D} \times z_2 \tag{4.33}$$

where D is the FZP diameter and z_2 is the distance between the FZP and the image plane.

The plot in figure 4.7 (d) shows clearly that the PSF spot radius decreases with the increasing N, which is consistent with the fact that larger FZPs have better imaging performance. In general, the PSF spot radii measured from the numerical results agree very well with the theoretical values, with an error within 2.4%. The errors are introduced not only from measurement bias, but also from the application of FFT in computational implementation. The errors and accuracy of numerical simulation due to the discrete sampling of FFT have been discussed in more detail in [79] [80].

4.6.3 Variation of detection distance

After the tests with single point source, we performed the optical simulation of the full imaging model with a classical resolution test target and different detection positions. In the simulation, the test target is defined by a resized bitmap image of 1951 USAF test chart composed by 0 and 1. The rescaling of test target is for the convenience of the convolution between the PSF and the ideal image in the algorithm. The parameters of the FZP used are $f = 8.98\ cm$, $R = 20\ \mu m$ and $N = 40$. We assume that the source is totally incoherent. The test chart to FZP distance is $3f$, leading to the creation of an image at $1.5f$, namely the focus. The detector is placed at five positions from $-2\ cm$ to $+2\ cm$ with respect to the focus. Figure 4.8 displays the numerical images of these five positions. From Figure 4.8, we can clearly see the focusing process of FZP along the distance, i.e., the improvement of the image contrast and its worsening, as well as the

halo around the 1st order image caused by the other diffraction orders. We may also observe the expected magnification of the image size for the increasing FZP–detector distance.

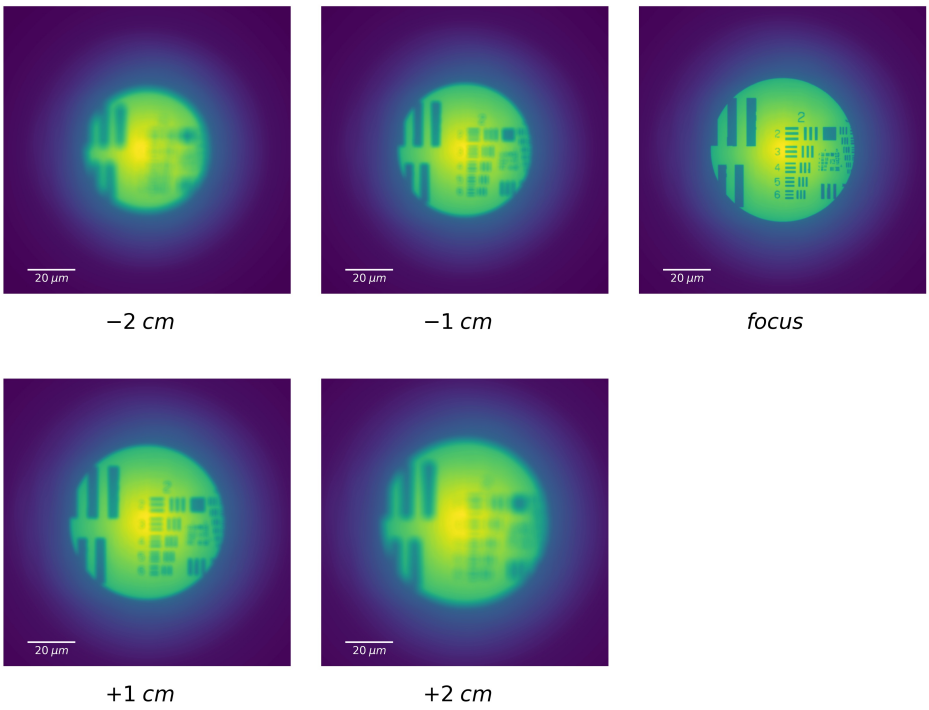

Figure 4.8: False color numerical images of a USAF 1951 test chart are recorded at various distances from the image plane in focus (marked as focus in the figure). The relative distance of each figure with respect to the focus plane is indicated at the bottom of the figure. The negative and positive signs represent the directions closer and further to the FZP, respectively. The dimension of each image is $120 \times 120 \mu m^2$.

4.6.4 FZP imaging performance versus number of zones

To our best knowledge, the quality of the image formed by a FZP versus the number of zones has never been studied. The purpose of this study is to find the FZP with acceptable resolution but with the smallest possible size, in order to design a dense FZP array for X-ray light field system. In this section, by the method presented in section 4.4, the images of the FZP with different N were simulated and compared to

the images formed by the refractive lens, respectively, under fully incoherent and fully coherent illuminations. The effect of the number of zones on FZP imaging performance is then discussed. The numerical results are performed from the FZP imaging model with the same geometry and parameters studied in the section 4.6.3.

- **Fully incoherent FZP imaging**

The set of simulation images displayed in figure 4.9 (a–e) represents the effect of changing the number of zones ($N = 5, 20, 40, 60, 100$). The part of interest on the test chart is zoomed in figure 4.9 (f). It is apparent from figure 4.9 (a–e) that as N increases, the image becomes sharper. As the radius of FZP is meanwhile broadened, the field of view is enlarged.

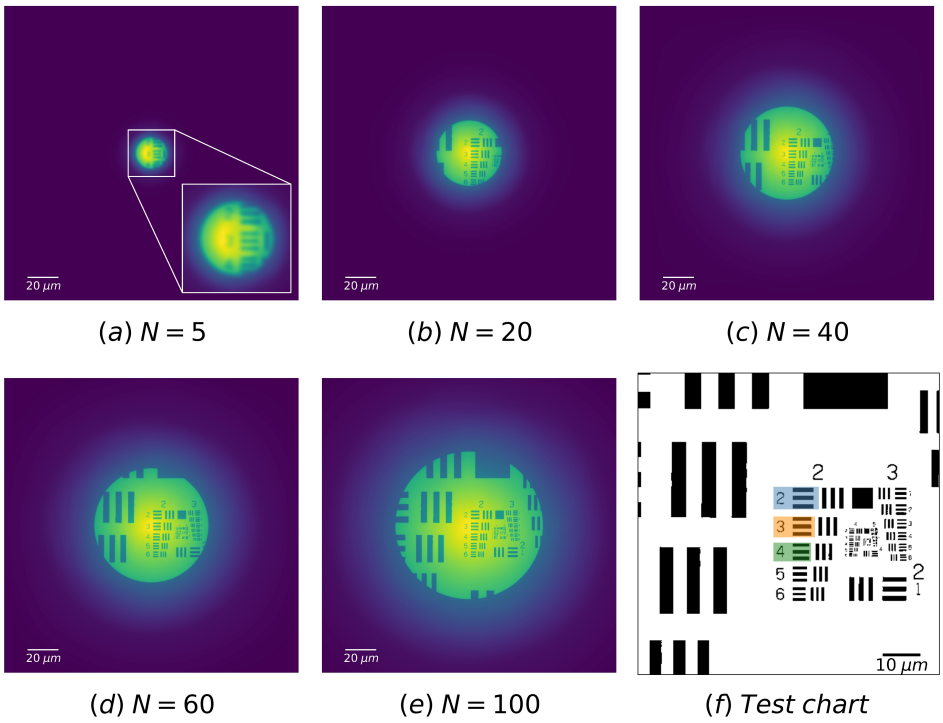

Figure 4.9: (a–e) False color numerical images of the USAF 1951 test target imaged by FZP with different number of zones. Each image dimension is $200 \times 200 \mu m^2$. (f) Zoomed part of interest on the test chart: for the following part, the blue, orange and green colored elements of bars in group 2 are respectively noted as elements *2.2*, *2.3*, and *2.4*. Their widths in the object plane are 2.72 μm, 2.36 μm, and 1.98 μm, respectively.

The effect of the number of zones on the final image quality is even more obvious in the intensity profile plot of bars. For example, the intensity profile of three groups of bars on the test chart (the blue-, orange-, and green-colored parts in figure 4.9 (f) are, respectively, named as elements *2.2*, *2.3*, and *2.4* in the following text) are plotted in figure 4.10, for different number of zones N. For the ease of comparison of the profile shape, the intensity plots have been normalized. While N increases, the plot shape of a bar approaches to a rectangle, which indicates the decrease in the PSF spot size of FZP (see in the insets at the lower part of figure 4.10).

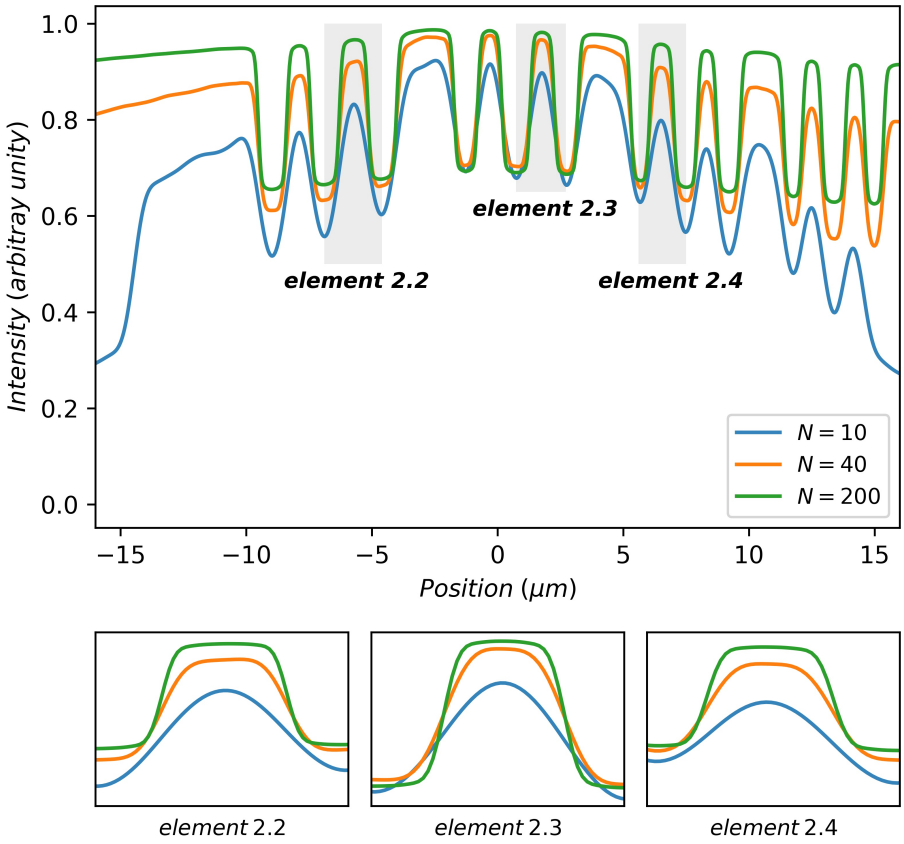

Figure 4.10: Intensity profile plots of images in focus with various numbers of zones: the images are simulated under the same conditions of Figure 4.8. Three zoomed parts of plot corresponding to different groups of bars are given below the main plot.

Comparing the three plots with different N in figure4.10, we can find that the intensity is not uniform across the image, being much greater near the center. And this effect is more notable for the FZP with smaller numbers of zones. The non-uniform distribution of intensity in the image originates from the particular geometry of FZP, that the width of zone is much wider near the center. And the first zone (central part) of the FZP used in the simulation is defined as transparent. Figure 4.11 shows two examples of FZPs with 10 and 40 zones. Hence, the direct beam (the 0th order) mainly comes from the central part of FZP, leading to the non-uniform distribution of intensity in the image. We remind that the image formed by a FZP is an integral image of different orders, and the two important intensity contributions are the 0th and the first order. When N is small, the intensity of the direct beam from the central transparent part is significant compared to the intensity of the 1st order diffraction. While N increases, the intensity of the 1st order diffraction is enhanced and less affected by the 0th order.

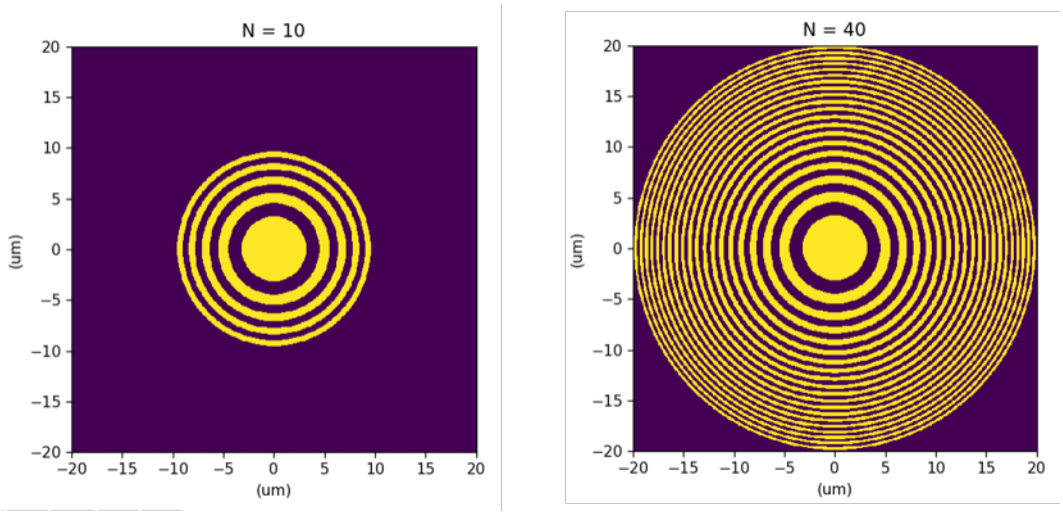

Figure 4.11: Geometry of FZP used in the simulation: The left and right parts display the FZPs with 10 and 40 zones. The transmission of yellow and purple parts are set to 1 and 0, representing transparent and opaque zones, respectively. Near the central part of FZP, the widths of zones are much wider and more different from each other.

In order to quantify the evolution of the image quality versus the number of zones in figure 4.9, several criteria might be use. One of the classical criteria is the contrast. It is defined as

$$Contrast = \frac{I_{max} - I_{min}}{I_{max} + I_{min}} \tag{4.34}$$

where I_{max} and I_{min} represent the highest and lowest intensities in a studied zone, respectively.

We measured the contrast of three sets of bars of USAF1951 test chart (see in figure 4.9 (f)) from the numerical images formed with the FZPs of different N. The results are plotted in figure 4.12. The contrast plots increase very quickly for the small N then evolve slowly. The trend of the contrast plots is consistent with the variation of the theoretical resolution of FZP with N.

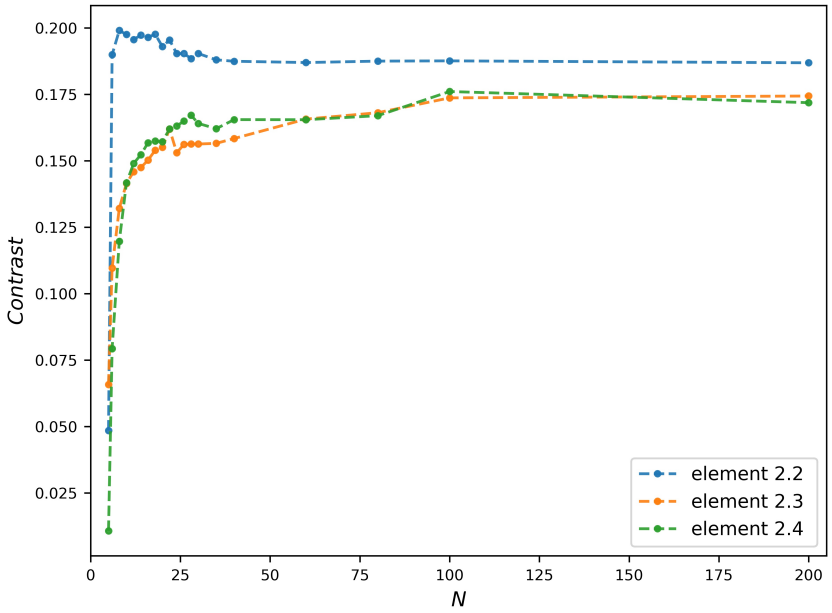

Figure 4.12: Contrast plots of different width bars versus number of zones N: the images are simulated under the same conditions of figure 4.9, the studied bars of test chart are shown in figure 4.9 (f).

Moreover, the stabilization starting points of contrast plot vary with the width of bars. The contrast plots reach stabilization with a larger N than that corresponding to the required resolution (equal to the width of bar). Taking the 2.36 μm wide bars of Element 2.3 as an example, the radius of theoretical PSF spot of the FZP with $N = 7$ (1.1 μm referring to the equation 4.33) is already below the bars width 1.18 μm in the image plane, but the contrast plot roughly reaches stabilization at $N = 27$. This delay of N is due to the fact that the stabilization of contrast requires the complete separation of points without overlap, which is stricter than the Rayleigh criterion used in the equation 4.33.

Another important remark from figure 4.12 is that the contrast value has a maximum value of only 0.2. In order to study its origin, we modeled the image formation with a theoretical perfect refractive lens. Supposed that the FZPs used for figure 4.9 can be replaced by the refractive lenses with the same numerical aperture (NA), the transmission function of refractive lens $t_{Lens}(x, y)$ is defined as

$$t_{lens}(x,y) = \begin{cases} \exp[-\frac{ik}{2f}(x^2+y^2)], & \sqrt{x^2+y^2} < R \\ 0, & else \end{cases} \tag{4.35}$$

where R and f are the radius and focal length of lens, respectively.

A group of images formed by the refractive lens is simulated under the same structure of figure 4.9, displayed in figure 4.13. For the ease of comparison with figure 4.9, the NA of refractive lens is represented by the corresponding number of zones N.

Figure 4.14 assembles the contrast plots of the same three sets of bars measured from refractive lens images. The contrast value of refractive lens images can reach a maximum of 0.94, much higher than that of FZP images. Furthermore, the contrast plots of refractive lens are more continuous and smoother. This is because the first order image of FZP overlaps with the other orders, resulting in a brightened and complex background.

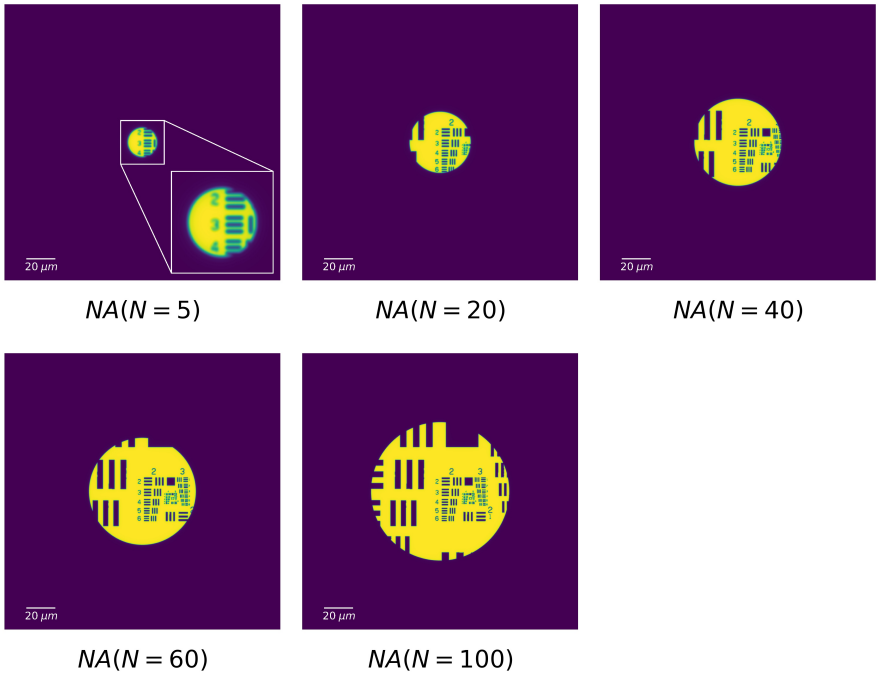

Figure 4.13: False color numerical images of the USAF 1951 test target imaged by refractive lens. The NA of the refractive lens equals to the NA of the FZP when the number of zones of FZP is 5, 20, 40, 60, and 100. Each image dimension is $200 \times 200\ \mu m^2$.

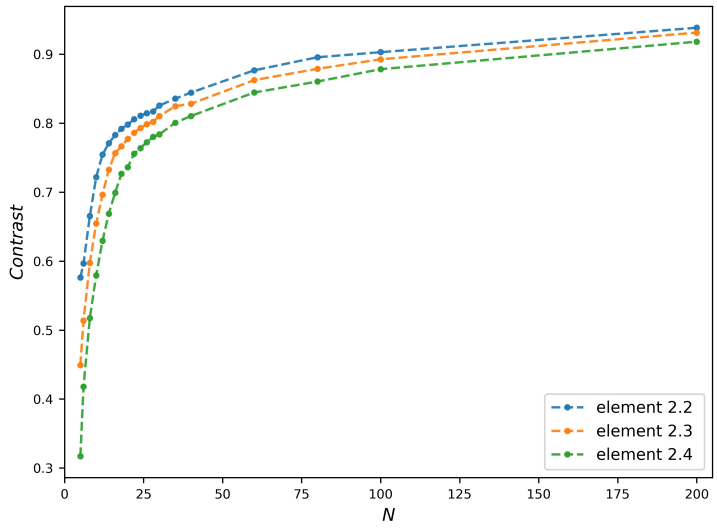

Figure 4.14: Contrast plots measured from the images formed by refractive lens: For the sake of clarity, the horizontal axis displays the number of zones of the FZP having the same NA than the refractive lens.

- **Fully coherent FZP imaging**

Keeping the same configuration as mentioned in the fully incoherent case, we discuss FZP imaging performance under fully coherent illumination in this section. The simulation images of FZP versus the number of zones N are shown in figure 4.15. As N increases, the first order image of FZP becomes more resolved. While the other orders images become much more intense in the fully coherent images than in the fully incoherent images, when N gets large. For this reason, the contrast plot can no longer reflect the evolution of FZP imaging performance with N as in the fully incoherent case.

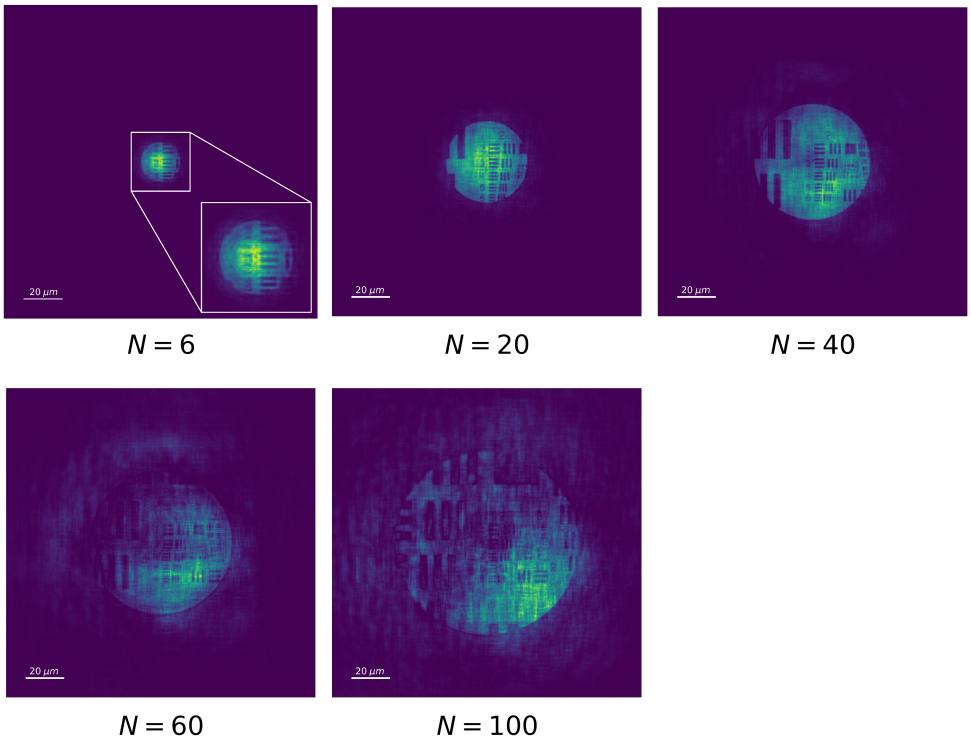

Figure 4.15: False color numerical images of the USAF 1951 test chart imaged by FZP with different number of zones under fully coherent illumination. The object—FZP distance is $3f$ and the FZP–image distance is $1.5f$, as same as for figure 4.9. Each image dimension is $160 \times 160\ \mu m^2$.

To visualize more directly the differences in FZP images under different coherence conditions, figure 4.16 displays side by side the fully incoherent and fully coherent images formed by the same FZP with $N = 100$. Unlike the other orders images with recognizable details in the fully coherent case, we can only see a diffuse halo overlapping on the first order image in the fully incoherent case. Indeed, the overlap of different orders images substantially degrades the quality and visibility of the first order image compared to the fully incoherent case.

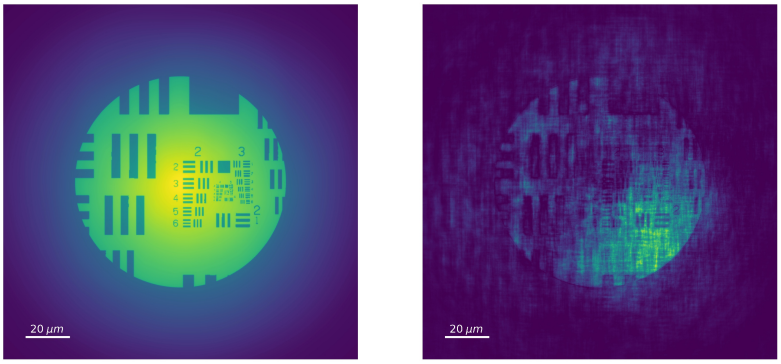

(*a*) *Fully incoherent* (*b*) *Fully coherent*

Figure 4.16: Comparison between fully incoherent and fully coherent images formed by FZP. The other orders images become more visible in the fully coherent case than the fully incoherent case, greatly degrading the first order image quality. N is equal to 100. Each image dimension is $160 \times 160\ \mu m^2$.

To bring out the characteristics of a FZP image, we also simulated a set of images formed by the refractive lens. The simulation model remains the same as the one used in figure 4.15, except that the FZPs with different N has been replaced by the refractive lenses with corresponding NA. The resulting numerical images are displayed in figure 4.17 and the NA are noted by the corresponding N for comparison purposes. Without the influence of different orders images, the refractive lens images are clearer and more visible than FZP ones. On the other hand, we can see in figure 4.17 that the diffraction patterns of each element of the test chart appear under fully coherent illumination, which shows the impact of coherence in imaging. On closer observation,

we can also find the diffraction pattern changes with different N, which is related to the divergence of the source in our model. The images can be regarded as a result of collective interference between each point of the test chart. The variation of the diffraction pattern then leads to the oscillation of the image intensity along N. In the fully coherent case, strong interference results in more complex images. It is also complicated to quantify the evolution of the image by the contrast as used in the fully incoherent case.

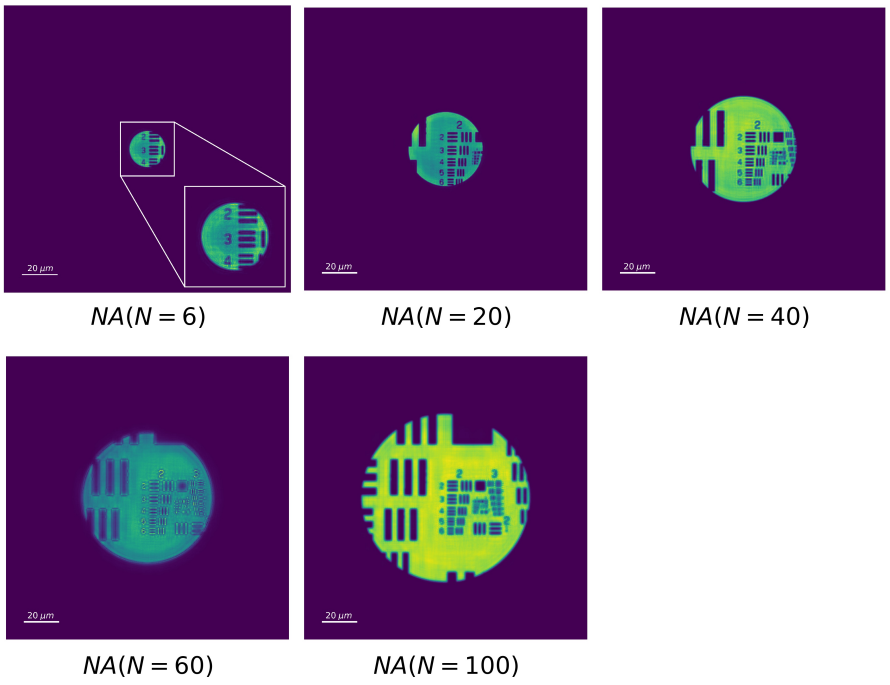

Figure 4.17: False color numerical images of the USAF 1951 test chart imaged by refractive lens under fully coherent illumination. The NA of the refractive lens equals to the NA of the FZP in figure 4.15 when the number of zones of FZP is 6, 20, 40, 60, and 100. Each image dimension is $160 \times 160\ \mu m^2$.

4.7 Conclusion

In this chapter, we suggested a X-ray light field imaging system based on FZP. The imaging performance of the FZP is dominated by its geometry parameters such as the number of zones and the outermost zone width. These parameters are interrelated, and

the FZP with larger size in general has higher resolution. To make a dense array for an X-ray light field imaging system, the size of each FZP in the array is greatly limited. To address this issue, a simulation method based on scalar diffraction has been introduced. The presented method is validated and capable of simulating the images formed by FZP with different parameters and under different coherence conditions. The effect of the number of zones on image formation has been discussed under fully incoherent and fully coherent conditions, especially the case of very small number of zones. The results have shown that surprisingly image can be formed with a number of zones as low as 5. However, due to the overlap of different orders of FZP, the images have relatively low contrast, and this influence of the other orders becomes more important in the fully coherent case than in the fully incoherent case. The reported simulation results in this chapter bring helpful information for the design of FZP array for an X-ray light field imaging system.

Chapter 5

Curved Crystal Study Towards X-ray Light Field Imaging

5.1 Background

Similar to the use of pixels to represent the resolution of a 2D image, voxel is defined as $Res_{lat} \times Res_{lat} \times Res_{depth}$ to reflect the resolution of a reconstructed 3D image. Res_{lat} and Res_{dep} are the lateral and depth resolutions of the imaging system in the sample plane. The Res_{lat} and Res_{dep} are proportional to $\frac{1}{NA}$ and $(\frac{1}{NA})^2$, respectively, where NA is the numerical aperture of the imaging system in the sample plane (see Appendix 7.A). For NA smaller than 1, the depth resolution decreases more rapidly than the lateral resolution with a factor of $\frac{1}{NA}$, leading to an elongated voxel.

However, due to the weak interaction of X-rays with matters, the NA of X-ray optics is generally small. Table 5.1 lists the NA of several common X-ray optics in low and high X-ray energy range reported in different literature. We can note from the table 5.1 that this issue is more problematic in the higher X-ray energy range, where the NA of X-ray optics drops sharply to below 10^{-3}. Consequently, the voxels become very elongated with aspect ratio length/width of 1000, greatly degrading the 3D Reconstruction quality. As the X-ray energy increases, the X-ray optics with decreasing NA, especially for the use as the main lens, will be a major bottleneck for the development of hard X-ray light field imaging system. Compared to the other X-ray optics in the table 5.1, diffracting

curved crystal with relative large NA seems to be a practical solution for the use as the main lens of X-ray light field imaging system.

Soft X-ray range Water Window (0.285-0.535 keV)		**Higher X-ray energy range** energy detailed in each case	
Optics	***NA***	**Optics**	***NA***
FZP [81]	0.048	FZP*	3×10^{-4} $(11\ keV)$
Mirror (Wolter type-I) [82]	0.05	Mirror (Wolter type-I) [83]	5×10^{-4} $(10\ keV)$
Multilayer toroidal mirror [84]	0.25	Compound refractive lens [85]	$few\ 10 \times^{-4}$ $(10\ keV)$
Curved crystal [86]	~ 0.5	Multilayer Laue lens [87]	6×10^{-3} $(16.3\ keV)$
		Curved crystal*	0.15 $(8\ keV)$

Table 5.1: Numerical aperture (NA) of X-ray optics in low and high X-ray energy range reported in different literature. The NA of the asterisked items are based on the studies in this thesis.

A crystal is a regular array of atoms with atomic plane spacing of the same order of magnitude as X-ray wavelength, and it is therefore a natural diffraction grating of X-ray. Moreover, the X-ray that satisfies the Bragg condition are intensely reflected by the crystal, due to the diffraction with internal lattice [88]. Because of this feature, a crystal is mainly used as monochromator in the study and the application of X-rays, selecting the X-ray beam of the desired narrow energy band [89] [90]. Besides monochromatization, by being manufactured into specific geometry, the crystal enables the focusing and imaging of X-rays. The concept of using single curved crystals for X-ray imaging, cylindrically bent in one dimension, was introduced as early as the 1930s [91]. With the development of the precise forming techniques in 1970s and 80s, doubly curved crystals, featuring different surface curvatures in two dimensions were demonstrated to be able to focus a point X-ray source onto a small spot, which offer a larger aperture and a higher resolution of imaging than singly curved crystals [92] [93]. Therefore, we present a prototype of plenoptic camera composed of a curved crystal as main lens, a FZP array and a detector (see figure 5.1). This curved crystal based plenoptic camera is proposed for the prospect of a light field scanning system operating in the hard X-ray for larger samples such as mice and their organs.

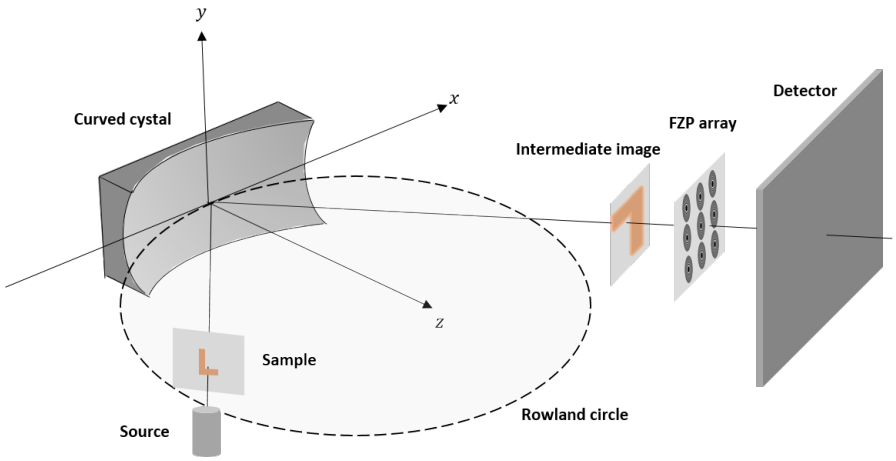

Figure 5.1: Principal structure of a curved crystal based X-ray light field system: Maintaining the same structure as the FZP based X-ray light field system described in Chapter 4 , the main FZP is replaced by a curved crystal.

In this chapter, the works on the design, measurement and focusing performance testing of the curved crystals for the use as main lens are reported. This chapter first introduces the basic of crystal imaging. Next, a ray-tracing algorithm developed for the study of crystal geometry is described in detail. Following the numerical investigation of the effect of crystal geometry on its imaging performance, three crystals of our customized design have been purchased. The verification of the internal and external structures of the three crystal performed on a 4-circle diffractometer is also presented. Finally, the experimental images of focal spot formed by one of the three crystals, a toroidal crystal, are displayed.

5.2 Bragg diffraction and rocking curve

X-ray imaging with curved crystal is based on Bragg diffraction of X-rays from crystal planes. An illustration of Bragg diffraction is shown in figure 5.2. X-ray hitting onto a crystal, of which the lattice spacing is comparable to the wavelength of X-ray, undergoes constructive interference at a certain incident angle and is scattered in a specular way with the same angle. The angle of incidence that produces intense reflection of X-ray is the so-called Bragg angle. The constructive interference occurs when the differences

in the travel path between X-rays are equal to integer multiples of the wavelength.

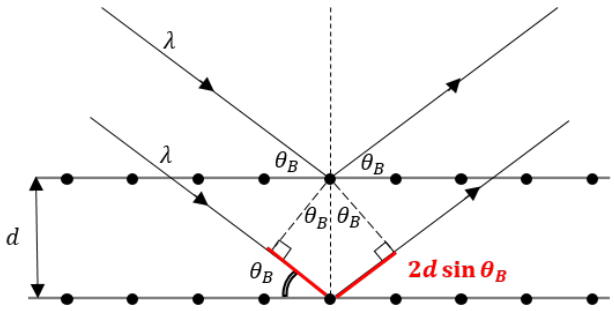

Figure 5.2: Bragg diffraction: when the difference in path between X-rays (red line section) is an integer number of wavelength, the incident X-ray will be scattered with the same angle as the reflection, due to constructive interference.

The general relationship between the wavelength λ of the incident X-ray, Bragg angle θ_B and spacing d between the crystal lattice planes of atoms is known as Bragg's Law, expressed as [94]

$$n\lambda = 2d \sin \theta_B \tag{5.1}$$

where n is an integer (the order of diffraction). In this chapter, we only consider the first-order diffraction, i.e. $n = 1$.

In real crystals, the presence of various defects leads to local irregularities in the crystal lattice, which makes the incident angle corresponding to strong diffraction different from the Bragg angle. The diffraction efficiency or reflectivity plot describing the diffraction response of the crystal at different incident angles of X-rays is known as rocking curve. For monochromatic X-rays, the rocking curve of a near-perfect crystal is a sharp peak, while that of an imperfect crystal it contains multiple peaks with larger width. As examples, the rocking curves of the near-perfect crystal $Ge(220)$ and the imperfect crystal $LiF(200)$ for X-rays with a wavelength of 1.540 Å are given in figure 5.3 (a) and (b), respectively.

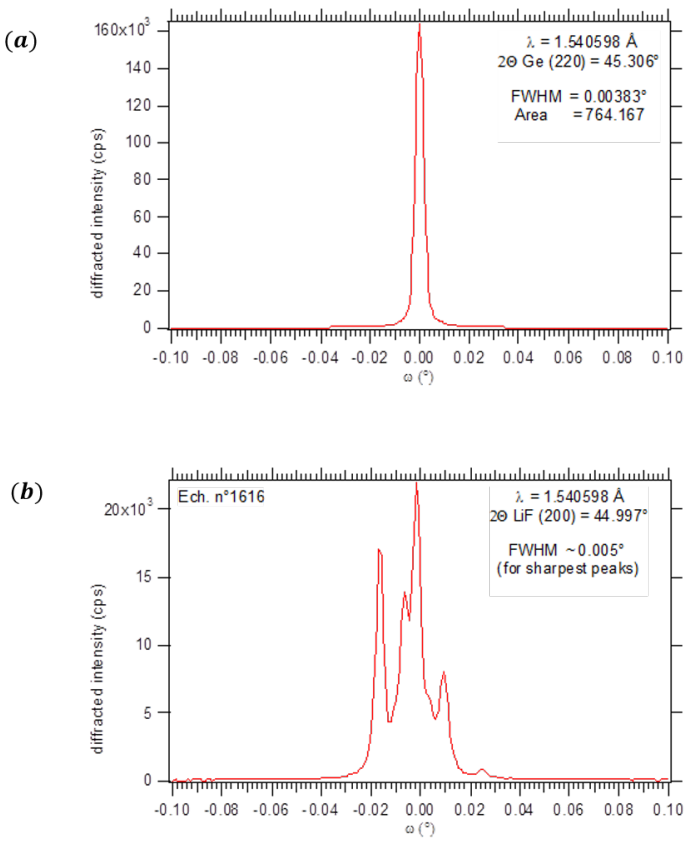

Figure 5.3: Rocking curve of crystal: (a) and (b) are the rocking curves of the near-perfect crystal $Ge(220)$ and the imperfect crystal $LiF(200)$. These rocking curves are obtained from the crystal manufacturer.

5.3 Rowland circle and imaging equation

Due to Bragg diffraction, the curved crystal behaves like a curved mirror for X-rays. The curved crystals discussed in this chapter refer specifically to concave curved crystals. The single curved crystal has a "focus circle" in the horizontal plane tangent to its center point, whose radius is equal to half the radius of curvature of the crystal. This circle was deduced by Rowland in 1883 for the concave grating in visible light, thus it is known as the Rowland circle [95]. If a point source lies on the Rowland circle of a concave curved crystal, it will be brought to a focus at another point on this circle, as shown in figure 5.4.

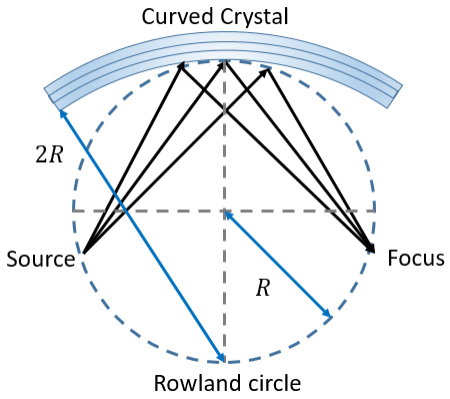

Figure 5.4: Rowland circle of concave curved crystal: A point source can be focused to a spot by a single curved crystal. The point source, the center point of crystal and the focus point lie on a common circle, the Rowland circle, of which the radius is equal to half the radius of curvature of the crystal.

Considering a more generalized model, doubly curved crystal, its meridional (horizontal) and sagittal (vertical) radii of curvature are denoted as R_m and R_s, respectively. The imaging geometry of the doubly curved crystal can be approximately described in the form of a thin lens equation :

$$\frac{1}{p} + \frac{1}{q} = \frac{1}{f} \tag{5.2}$$

where p is the object distance from the crystal, q is the image distance from the crystal and f is the focal length. The doubly curved crystal has two focal lengths, the meridional one f_m and sagittal one f_s, respectively given by

$$f_m = \frac{R_m \sin\theta}{2}$$

$$f_m = \frac{R_s}{2\sin\theta} \tag{5.3}$$

where θ is the angle between the incident ray and the tangent line to the vertex of the curved crystal. The curved crystal has the effect of optical magnifying. The magnification is defined as $M = \frac{q}{p}$.

The imaging equation of curved crystal has been derived from the Fermat's principle

with certain approximations, initially to minimizing the lowest order aberration of the focus. The demonstration is lengthy and has been discussed in great detail in other literature [96] [97], so it will not be repeated here.

5.4 Geometry of curved crystal

The curved crystal geometry can be divided into two main aspects: the curvature of the internal lattice planes and the curvature of the surface. Both can affect the imaging quality of crystal, such as aberration, image fluence and numerical aperture.

Adjusting the curvature of internal lattice planes can optimize the focusing performance of the crystal. Referring to the equation 5.3, the focal lengths of the crystal in the meridional and sagittal planes are different for $\theta \neq 90°$ and strongly diverge for $\theta \to 0$. Therefore, imaging with a spherically curved crystal will lead to astigmatism. Astigmatism can be reduced when the two focal lengths are equal, leading to

$$R_s = R_m \sin^2 \theta \tag{5.4}$$

To obtain the highest reflectivity, θ is commonly set to Bragg angle θ_B. A toroidal crystal, whose lattice planes have different curvatures in the meridional and sagittal, can achieve such geometry as described by the equation 5.4 and provide better focusing. Let us now consider the focusing property of a curved crystal in meridional plane. There is a monochromatic point source on the Rowland circle of the curved crystal, and the connection of the source with the crystal center point forms the corresponding Bragg angle with the tangent line of the crystal surface. The surface of the curved crystal is parallel to its lattice planes, which is called as Johann geometry [98].

Even though the divergence of the point source is large enough to illuminate the entire crystal, only the chief ray arriving at the crystal center satisfies the Bragg condition and can be intensely reflected (see figure 5.5 (a)). Although the crystal has certain tolerance on the incident angle according to its rocking curve, the rocking curve width is very narrow (0.0029° for a near-perfect crystal and 0.029° for an imperfect crystal [99]). Consequently, the effective diffracting zone is very small and the reflection efficiency

of the crystal is quite low. The diffracting zone of a curved crystal can be expanded by Johansson geometry [100], which involves a crystal bent to a radius of $2R$ with a ground inner surface of its Rowland circle radius R, as shown in figure 5.5 (b). Due to the inscribed angle theorem of a circle, such geometry allows the rays from the source to arrive on the entire crystal surface at the Bragg angle.

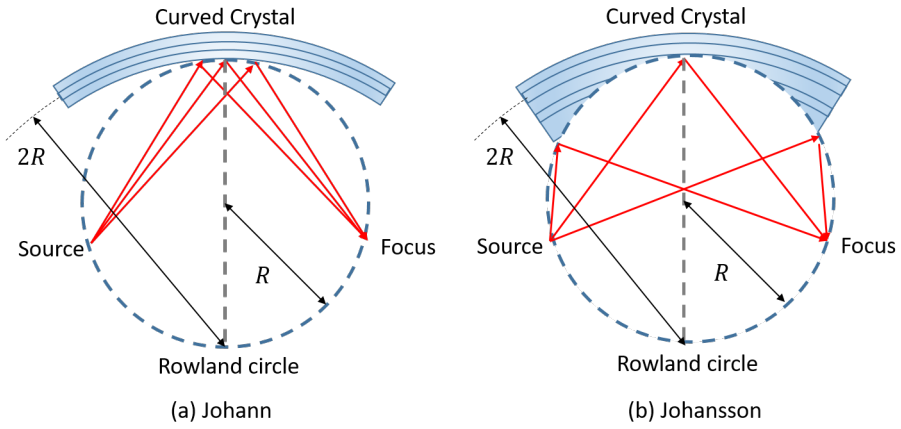

Figure 5.5: Johann geometry and Johansson geometry: (a) the radii of the crystal surface and lattice plane are the same, so only the rays reaching near the centre of crystal meet the Bragg condition. (b) The radius of the inner surface of the crystal is equal to half the radius of its lattice plane. The rays arrive on the entire crystal at Bragg angle.

5.5 Ray-tracing algorithm for the study of crystal geometry

As previously described, the imaging performance of curved crystal is highly dependent on its geometry. There are various possibilities for the geometry of curved crystals, and their realisation is difficult and costly. Therefore, we developed a numerical approach to design the geometry of the crystal and to study its imaging properties. The core of this numerical approach is to track each ray arriving on the curved crystal under the geometrical optic model.

A schematic of the horizontal cross section of the curved crystal diffraction system illustrates the principle of the algorithm (see figure 5.6).

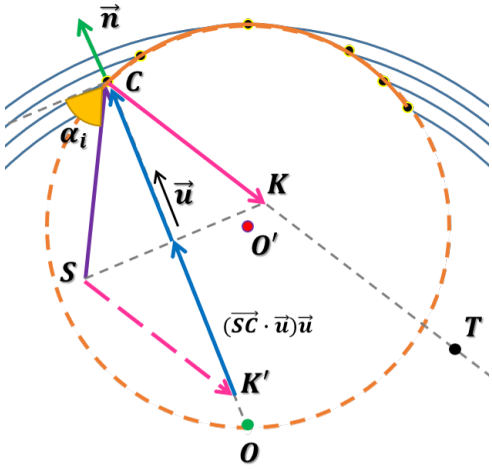

Figure 5.6: Horizontal cross section of a curved crystal diffraction system: The bent lattice planes of crystal are represented by the blue arcs. Its inner surface ground along the Rowland circle is drawn in orange arc. An arbitrary indent ray $\overrightarrow{SC}$ hitting on the crystal is diffracted to the direction $\overrightarrow{CK}$. The diffracted direction vector $\overrightarrow{CK}$ has been translated to join the tail of incidence vector $\overrightarrow{SC}$ to help understand the vector operation. $\vec{n}$ is the normal vector of the lattice plane at the incident point C. T is a arbitrary point of the diffracted ray.

The blue and orange arcs represent the lattice planes and the surface of crystal. The orange dashed circle is the Rowland circle of the curved crystal. The points O and O' denoted the centers of the lattice planes and the Rowland circle, respectively. Figure 5.6 shows an example of a curved crystal with the surface ground along its Rowland circle, i.e. Johansson geometry. In fact, by defining the functions of the lattice planes and the surface, the curved crystal can be modeled to any designed geometry in the simulation. The algorithm performs ray tracing by means of vector calculations. Assuming one arbitrary incident ray emitted by the source S hits at point C on the crystal, the incident angle α_i can be calculated from the scalar product of the normal vector $\vec{n}$ of the lattice planes at C and the incident vector $\overrightarrow{SC}$, written as

$$\alpha_i = \arcsin\left(\frac{\vec{n}\cdot\overrightarrow{SC}}{|\vec{n}||\overrightarrow{SC}|}\right) \tag{5.5}$$

The normal vector $\vec{n}$ of the curved lattice planes $F(x, y, z) = 0$ at point $C(x_c, y_c, z_c)$ is given by the gradient

$$\vec{n} = \nabla F(x, y, z)|_{C(x_c, y_c, z_c)} \tag{5.6}$$

The incident angle of each ray hitting on the crystal can be calculated by the equation 5.5, then the rays that can be diffracted are selected according to the rocking curve width.

Referring to Bragg diffraction, the diffracted direction $\overrightarrow{CK}$ should be symmetric to the incident direction $\overrightarrow{SC}$ with respect to the normal vector $\vec{n}$, where K is the symmetry point of S. Thus, the diffracted direction $\overrightarrow{CK}$ can be calculated by vector operation

$$\overrightarrow{CK} = \overrightarrow{SC} - 2(\overrightarrow{SC} \cdot \vec{u})\vec{u} \tag{5.7}$$

where $\vec{u}$ is the unit vector of $\vec{n}$, $\vec{u} = \frac{\vec{n}}{|\vec{n}|}$. And $(\overrightarrow{SC} \cdot \vec{u})\vec{u}$ is the projection vector of $\overrightarrow{SC}$ to the direction of the vector $\vec{n}$. An arbitrary point T on the ray diffracted by the point C of the crystal can thereby be described by a line equation

$$T = t\,\overrightarrow{CK} + C \tag{5.8}$$

where t is a magnitude number.

Furthermore, the image of the curved crystal can be considered as the set of the intersections of the all diffracted rays and the detector plane. We define the detector plane by its center point P_0 and its normal vector $\overrightarrow{n_p}$ as

$$(P - P_0) \cdot \overrightarrow{n_p} = 0 \tag{5.9}$$

where P is an arbitrary point contained by the detector plane. The intersection of each diffracted ray with the detector plane must satisfy both its definition line equation and

the detector plane equation. Substituting the line equation 5.8 into the detector plane equation 5.9, the intersection of a diffracted ray is given by

$$t = \frac{(P_0 - C) \cdot \overrightarrow{n_p}}{\overrightarrow{CK} \cdot \overrightarrow{n_p}} \tag{5.10}$$

Applying the above calculation to all diffracted rays, we can obtain the coordinates of all intersection on the detector. Finally, plotting all the intersections in the local coordinate system of the detector forms the image achieved by the curved crystal.

5.6 Effective diffracting area of curved crystal

As the main lens of an imaging system, the curved crystal must have a large solid angle (equivalent to the numerical aperture of lens) to collect the rays. In addition, the incident angle of the collected rays should be equal to the Bragg angle within the tolerance given by the rocking curve width, which is a major restriction of crystal optics. Limited by the angular condition of the rocking curve, not every point on the crystal surface is efficiently diffracting for a given point source. The set of points on the crystal surface that forms with the given point source an incidence angle within the range of rocking curve is called the effective diffracting area. The numerical aperture of crystal is highly depending on its effective diffracting area. The study of the effective diffracting area is of particular interest for the design of the crystal as the main lens, since a bigger effective diffracting area means a higher collection efficiency and a larger numerical aperture.

The effective diffracting areas of crystals with different geometries have already been studied by Wittry and coworkers. To validate the introduced algorithm in the previous section, we will compare our numerical results to two analytical results from Wittry's article [101]. The curvatures of the lattice planes and inner surface of the crystal in arbitrary unit of the two cases in Wittry's article are summarized in the table 5.2.

	Radii of the inner surface		**Radii of the lattice planes**	
Case	R_{r_xy}	R_{r_yz}	R_{c_xy}	R_{c_xy}
Johansson	0.5	∞	1	∞
Spherical planes **Toroidal surface**	0.5	1	1	1

Table 5.2: Crystal parameters in arbitrary unit of two cases considered in Wittry's article.

The point source is set on the Rowland circle and the beam incidence angle at the center of crystal is exactly equal to the Bragg angle that ranges from 15° to 75°. The width of the rocking curve is supposed to be ±0.006°. Wittry's analytical results of the two cases are displayed in figure 5.7 (a) and (c). Our corresponding numerical results are shown in figure 5.7 (b) and (d).

In figure 5.7, the numerical results are basically identical to Wittry's analytical results, except that the simulation results are more asymmetrical about y-z plane than Wittry's ones. The differences are caused by the neglected high order terms and the approximation of normal vector in Wittry's analysis.

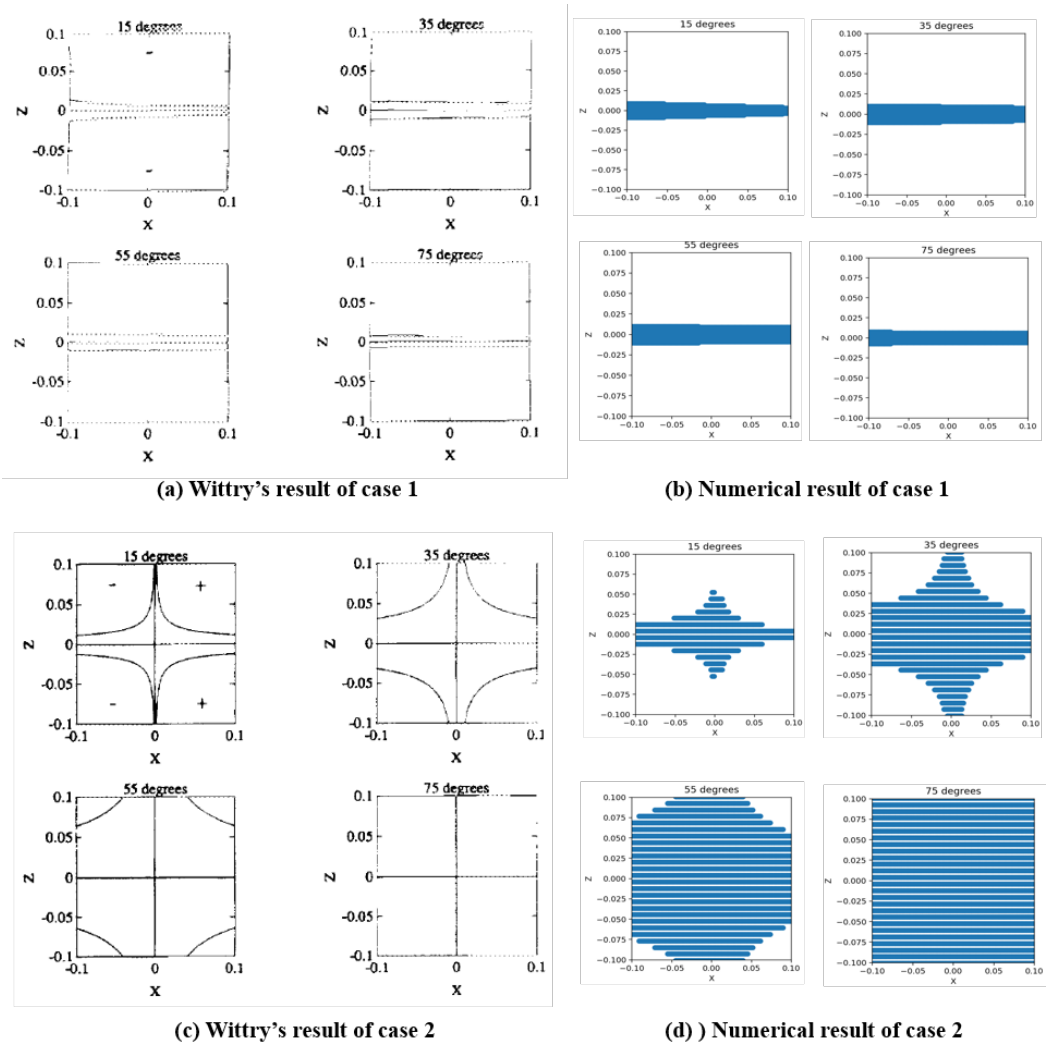

Figure 5.7: Comparison between Wittry's analytical results and our numerical results: (a) and (c) are Wittry's analytical results in the article [101]. (b) and (d) are the numerical results obtained by our ray tracing algorithm.

5.7 Numerical investigation of toroidal crystal

In addition to the geometries examined above, the toroidal crystal, of which the surface and the lattice plane are both toroidally shaped, is of greater interest as main lens. Because it can theoretically provide point-to-point focusing. With the validated algorithm, we firstly numerically investigated the effect of Bragg angle and the effect of rocking curve width on the effective diffracting area of toroidal crystal. The structural parameters of the toroidal crystal (toroidally bent lattice planes and toroidally ground surface) used in this study are given in the table 5.3.

Case	R_{r_xy}	R_{r_yz}	R_{c_xy}	R_{c_yz}
Toroidal planes **Toroidal surface**	150 cm	$R_{c\_xy}\sin^2\theta_B$	300 cm	$R_{c\_xy}\sin^2\theta_B$

Table 5.3: Structural parameters of the toroidal crystal investigated

We consider two cases: (1) the width of rocking curve fixed at $\pm 0.005°$, Bragg angle ranges from 15° to 75°, (2) Bragg angle fixed at 15°, the width of rocking curve ranges from $\pm 0.005°$ to $\pm 0.02°$. The corresponding simulation results are displayed in figure 5.8 (a) and (b). Note that the scale of graph in figure 5.8 (a) is three times larger than in figure 5.8 (b).

The results shown in figure 5.8 indicate that both the Bragg angle and the width of the rocking curve have an impact on the effective diffracting area of toroidal crystal. The increase of Bragg angle expands the entire effective diffracting area (the x-direction enlargement is limited by the given crystal length in the simulation), while the increasing width of rocking curve mainly dilates the horizontal part of the cross-shaped in z direction. In the cross-sectional comparison, the effect of Bragg angle is more prominent compared to the rocking curve width on the effective diffracting area of toroidal crystal. In other words, large Bragg angle helps to increase the numerical aperture of toroidal crystal and thus the collection efficiency of X-rays, which provides a clue to the choice of material. However, as the Bragg angle increases, the spacing between the incident

and reflected beams decreases, resulting in difficulties in the installation of the other components of the imaging system.

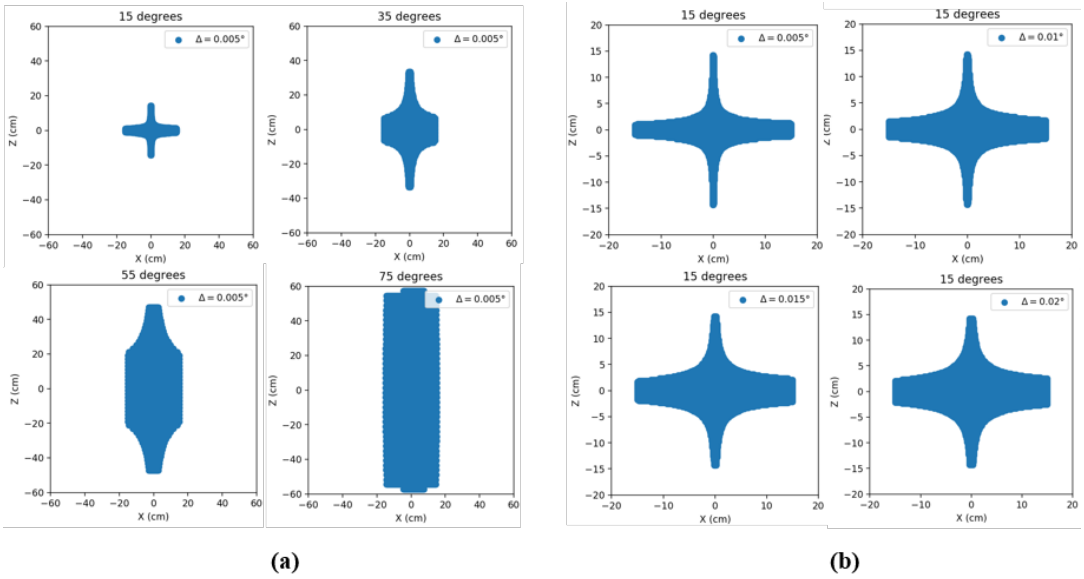

Figure 5.8: Effective diffracting area of toroidal crystal: (a) Effect of Bragg angle: the width of rocking curve fixed at ±0.005°, Bragg angle ranges from 15° to 75°; (b) Effect of rocking curve width: Bragg angle fixed at 15°, the width of rocking curve ranges from ±0.005° to ±0.02°. Note that the scales of (a) and (b) are different.

With the help of the ray-tracing algorithm, we also verified the focusing performance of the toroidal crystal and compared it to the curved crystals of other geometries. Here, three different curved crystals are considered. They have the same ground surface of Johansson geometry and the same horizontal radius of the lattice planes, except that the vertical curvature of their lattice planes varies. The structural parameters of the three curved crystal are summarized in the table 5.4. In the simulation, the point source is situated on the Rowland circle in the meridional plane. The chief ray emitted from the source arrives at the center point of the curved crystal with Bragg angle. The width of rocking curve is ±0.02°.

Case	R_{r_xy}	R_{r_yz}	R_{c_xy}	R_{c_yz}
Cylindrical planes **Toroidal surface**	150 cm	$R_{c\_xy}\sin^2\theta_B$	300 cm	∞
Spherical planes **Toroidal surface**	150 cm	$R_{c\_xy}\sin^2\theta_B$	300 cm	300 cm
Toroidal planes **Toroidal surface**	150 cm	$R_{c\_xy}\sin^2\theta_B$	300 cm	$R_{c\_xy}\sin^2\theta_B$

Table 5.4: Structural parameters of three curved crystals investigated with the same diffracting surface but different lattice planes.

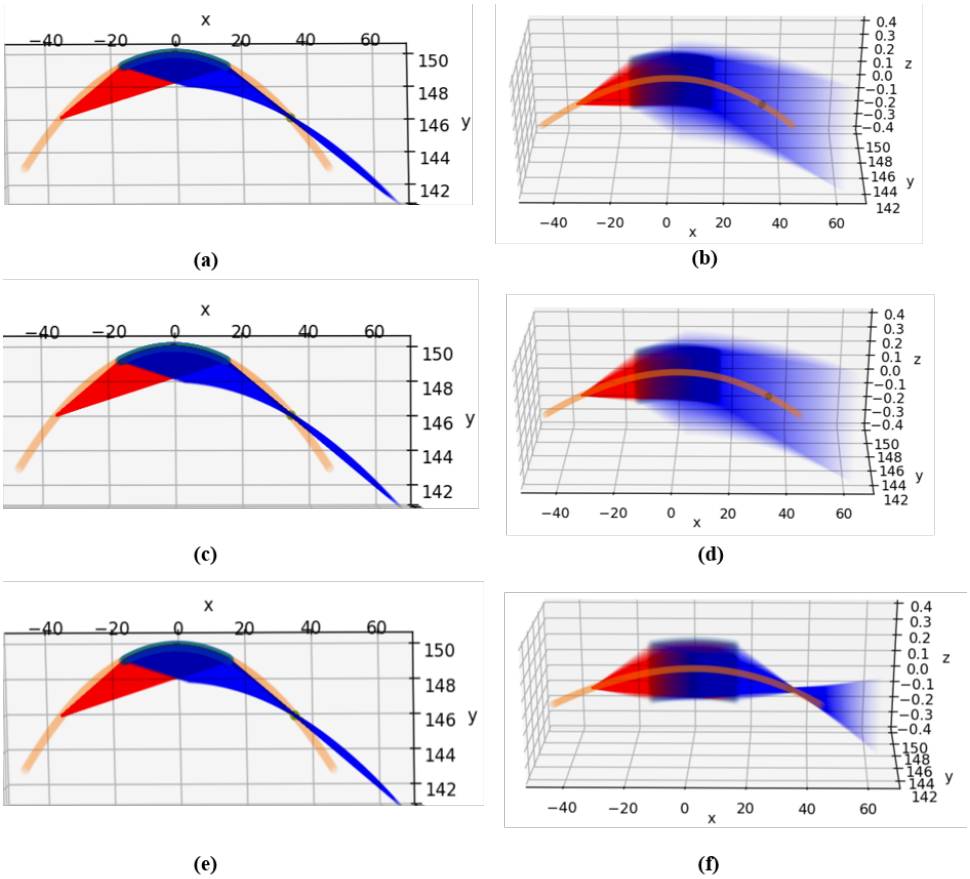

Figure 5.9: Focusing performance simulation of different crystal geometries: (a) and (b) Top view and front view of the crystal with cylindrical planes and toroidal surface; (c) and (d) Top view and front view of the crystal with spherical planes and toroidal surface; (e) and (f) Top view and front view of the crystal with toroidal planes and toroidal surface.

The top view and the front view of the simulation results are shown in the left and right columns of figure 5.9, respectively. The incident and the diffracted beams are colored in red and blue, respectively. The orange arc represents the Rowland circle. Apparently, all the three crystal geometries are capable of focusing the diverging rays from a point source in the meridional plane. Nevertheless, only the toroidal crystal, of which the horizontal and vertical radii of the lattice plane satisfy the equation 5.4 for the reduction of astigmatism, can focus the rays in both the meridional and sagittal planes. Furthermore, even though the three crystals have the same toroidal ground surface, again, only the crystal with the toroidal lattice planes provides the point-to point focusing. This reveals that the focusing performance of the curved crystal is dominated by its internal structure.

Figure 5.10 provides the simulation image of the focal spot formed by this toroidal crystal. The detector plane is centered at the focus on the Rowland circle and perpendicular to the diffraction direction of the chief ray.

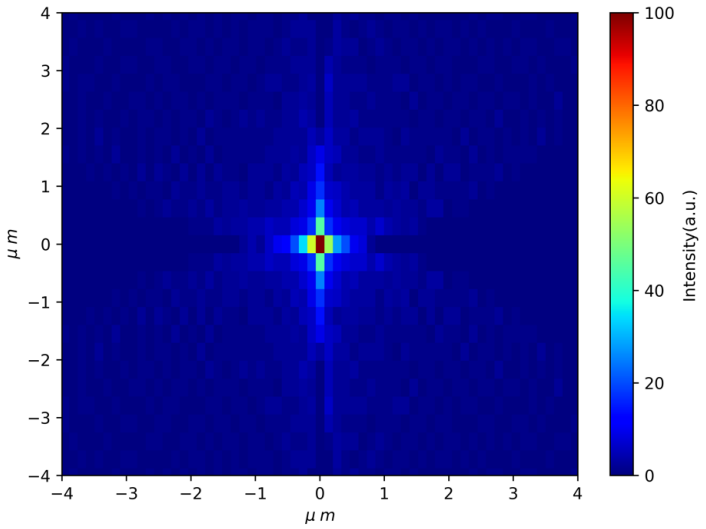

Figure 5.10: Simulation image of focal spot formed by the toroidal crystal: The point source, the toroidal crystal and the detector are all on the Rowland circle. The orientations of the point source and the detector both enclose the Bragg angle with the tangent line of the crystal center.

The simulation result confirms the point-to point focusing ability of the toroidal crystal. With a closer inspection of the simulation focal spot, we can see the strong focusing by the toroidal crystal in the horizontal and vertical direction, producing a cross shape instead of a circular focal spot.

5.8 Three crystals designed and fabricated

Following the above theoretical investigations, three crystals have been designed and fabricated for the wavelength 1.542 Å (the average wavelength of copper $K\alpha_1$ and $K\alpha_2$ radiations, equivalent to the source energy 8 keV): two toroidal germanium (400) crystals with meridian and sagittal radii satisfying the equation 5.4 for the use as the main lens and one cylinder germanium (111) crystal for the use as the monochromator and condenser. The fabrication of the crystals was carried out by Saint-Gobain. All the three crystals are of Johansson geometry, i.e. the diffracting surface has been ground along the Rowland circle. The table 5.5 lists in detail the relevant parameters for the three crystals. The photos of a toroidal crystal and the cylindrical crystal are shown in figure 5.11 (a) and (b), respectively.

	Toroidal 1 (Ge 400)	Toroidal 2 (Ge 400)	Cylindrical (Ge 111)
R_m	336 mm	336 mm	1000 mm
R_s	100 mm	100 mm	∞
$2d$	2.829 Å	2.829 Å	6.532 Å
θ_B (1.542 Å)	33.03°	33.03°	13.67°
Dimensions	40 $mm \times 20$ mm	39.6 $mm \times 19.6$ mm	50 $mm \times 20$ mm

Table 5.5: Parameters of three crystals designed and fabricated.

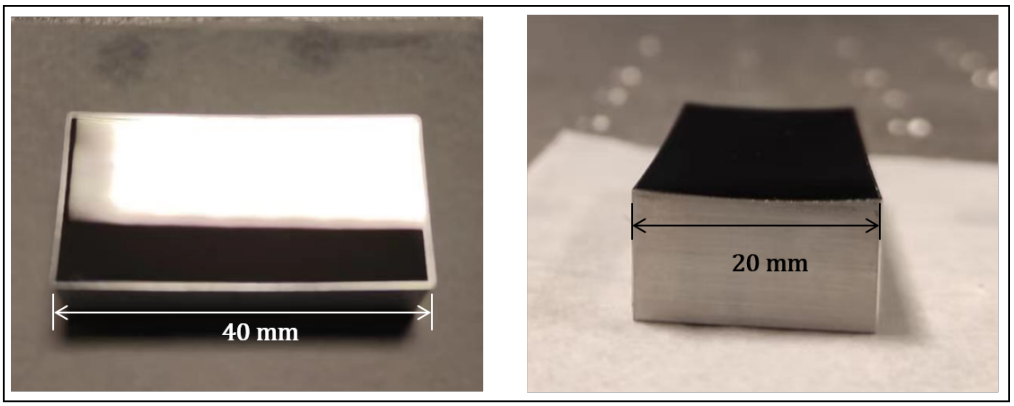

(*a*) Toroidal crystal

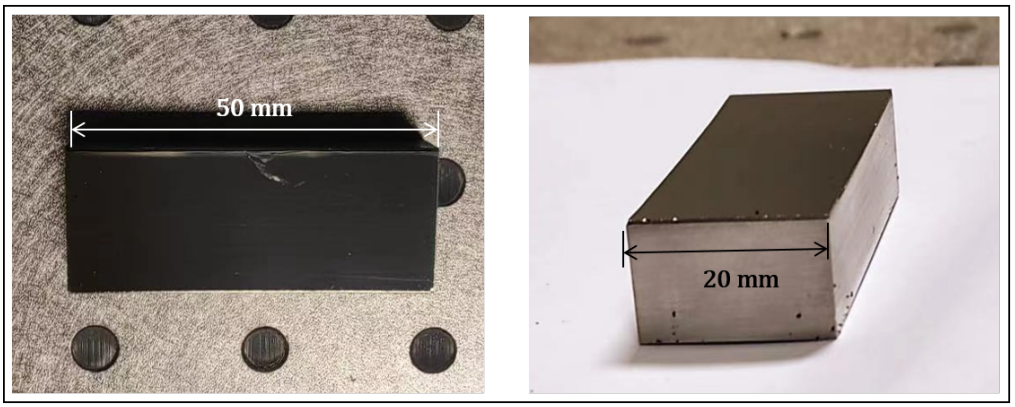

(*b*) Cylindrical crystal

Figure 5.11: Photos of the fabricated crystals: (a) Toroidal crystal (b) Cylindrical crystal. The left and right columns of the figure show the top and side views of the crystal respectively. The crystals are glued on an approximately 10 *mm* thick aluminium substrate.

5.9 Experimental measurements of the three crystals

Inevitably, there are deviations between the practical fabrication of curved crystals and their theoretical design, which affect the optical parameters and imaging performance of curved crystals. Therefore, checking the curvature of the curved crystal and measuring its rocking curve is essential for its successful application in imaging system.

For this purpose, X-ray diffraction (XRD) is a suitable method, which is a commonly used technique for the non-destructive analysis of crystal properties and structures. We performed the XRD measurements of the three crystals fabricated with Dr. Vincent

Jacques on a 4-circle diffractometer in the Laboratoire de Physique des Solides (LPS), Orsay, France. The 4-circle diffractometer used and the schematic of its main structure are shown in figure 5.12 (a) and (b), respectively.

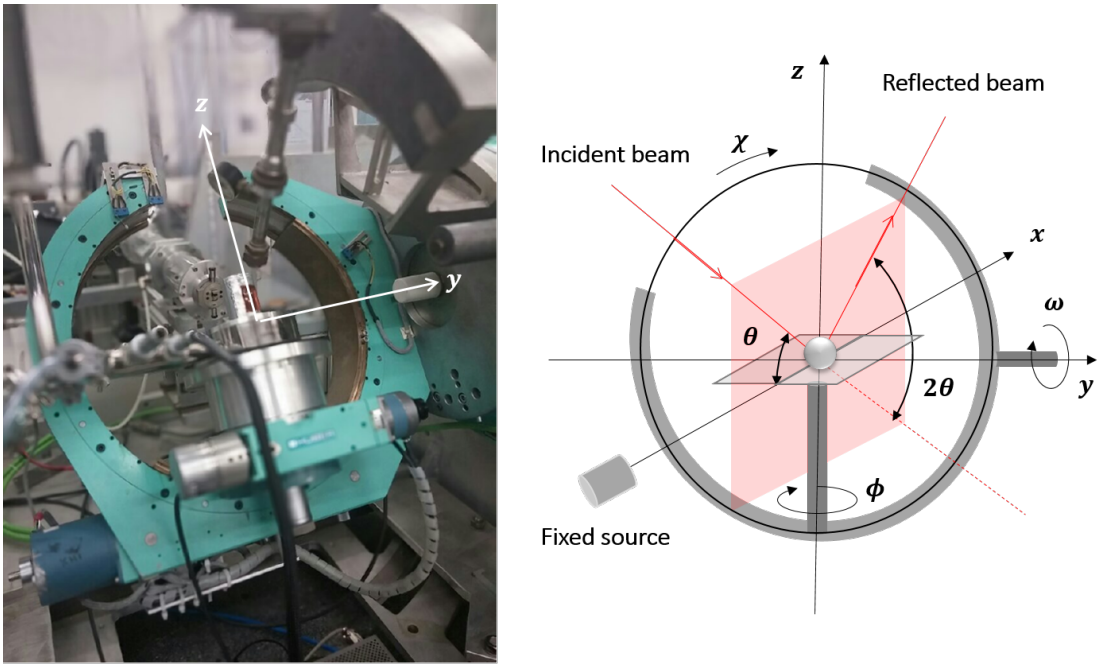

(*a*) (*b*)

Figure 5.12: XRD measurement set-up in LPS: (a) experimental 4-circle diffractometer (image from [102]) (b) main structure schematic of (a). Note that the incident angle of beam θ is changed by rotating the sample instead of the source. The incident beam in red in (b) indicates the relative position of the source to a rotated sample in the coordinate system centred on the sample.

The 4-circle diffractometer allows the sample to be rotated in 3 axial directions. The incident direction of X-ray beam of the 4-circle diffractometer is fixed (x direction in figure 5.12 (b)), and the incident angle θ on the sample can be changed by the rotation of the sample about the y axis. The angle of y-axial rotation ω and the incident angle θ has the relationship $\omega = \theta$. The other two angles of rotation about the x and z axes are denoted as χ and ϕ. To better relate the schematic of the main structure and the experimental set-up in figure 5.12, two corresponding axes are drawn in figure 5.12 (a).

Besides the three rotation circles of the sample, the last one of the 4-circle diffractometer refers to the rotation of the detector in the $x-z$ plane. For the clarity of illustration, the rotation circle of the detector is not drawn in figure 5.12 (b). To catch the theoretical reflected beam, the rotation angle of the detector, with respect to the extension of the incident beam, need to be equal to 2θ.

Using the 4-circle diffractometer, we performed three different XRD scans on five different positions of each crystal. These scans are realized with the filtered Cu anode source of 8 keV, consisting of 2 wavelengths, 1.540 Å and 1.544 Å. The five test positions (hereafter denoted as $Pos1 - Pos5$) are around the centre of crystal and the same for each crystal, shown in figure 5.13.

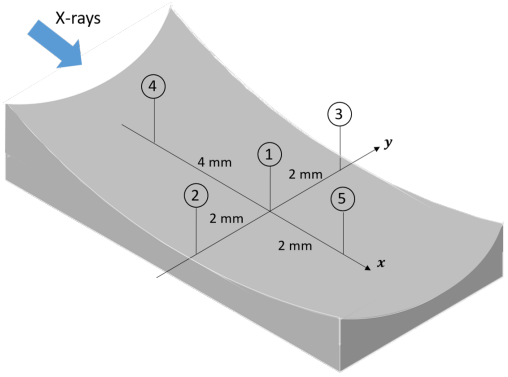

Figure 5.13: XRD scan positions: The $Pos1$ is situated in the center of each crystal. $Pos2$ and $Pos3$ are in the sagittal plane, and $Pos4$ and $Pos5$ are in the meridional plane. The distances between them are marked on the figure.

In the following, each of the three scan is firstly described, then the corresponding results are reported. Again, the position and the direction of the X-ray source remain the same for all scans.

- **ω scan**

The detector is fixed in the theoretical reflection direction of Bragg diffraction ($2\theta_B$), while the sample rotates about the y axis, i.e. only ω changes (See figure 5.14). The result is an X-ray intensity plot versus ω.

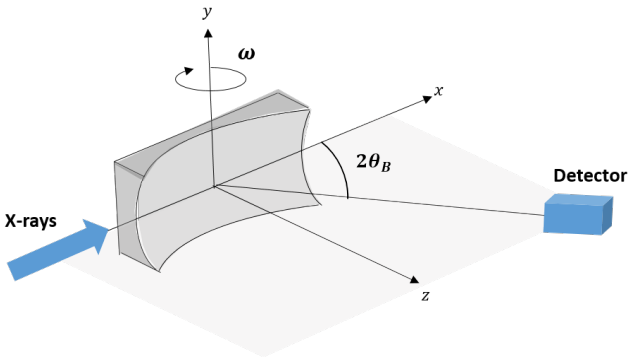

Figure 5.14: Schematic of ω scan configuration: The X-ray source is fixed. the detector is at the angle of $2\theta_B$ form the incident direction of X-ray. The crystal rotates about the y-axis. The rotation angle is ω.

The rocking curve of the crystal, the plot of the reflection efficiency of crystal with the incident angle of beam, can be obtained by dividing the measured plot by the intensity of direct beam. The measured rocking curves of the three crystals are displayed in figure 5.15.

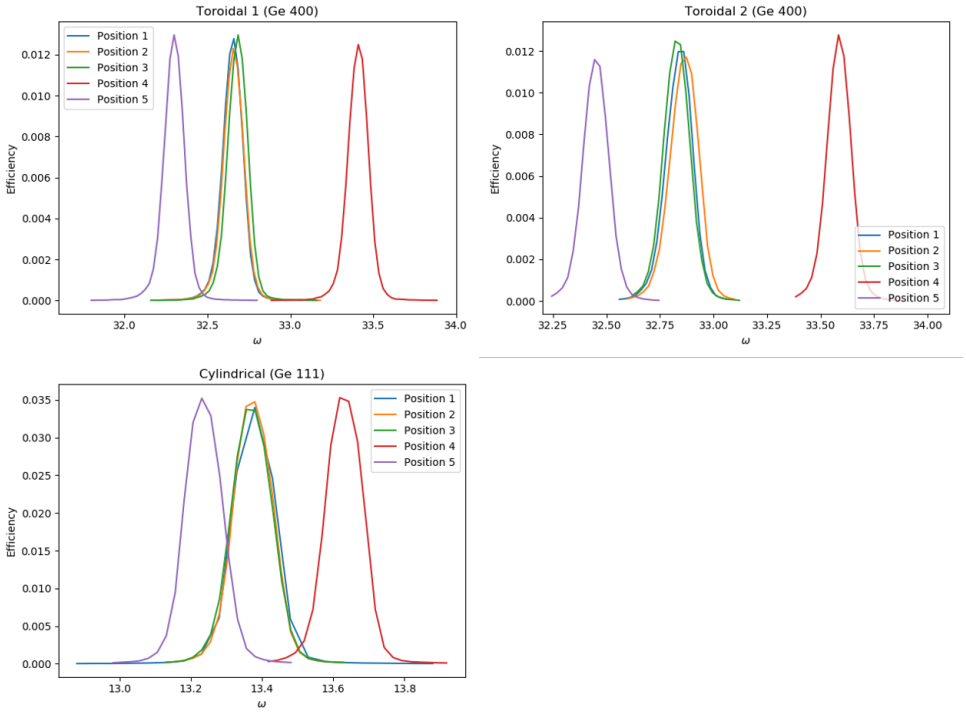

Figure 5.15: Plots of the ω scan, namely the rocking curve, measured at five different positions on each of the three crystals.

We will first individually examine the rocking curve at different positions. The peak deviation between different positions will then be discussed. The incident angle that maximizes the reflection of crystal is the Bragg angle. The Bragg angle, the maximum reflection efficiency and the full width at half maximum (FWHM) of the rocking curves measured from the three crystals are provided in the table 5.6. The experimental values given are the average of five positions scans for each crystal. The theoretical values of θ_B and the bias between the theoretical and experimental values are also given in the table 5.6. Note that the theoretical values of θ_B are calculated with the source wavelength 1.540 Å and thus slightly differ from the designed values in the table 5.5

	Toroidal 1 (Ge 400)	Toroidal 2 (Ge 400)	Cylindrical (Ge 111)
Theoretical θ_B	32.98°	32.98°	13.72°
Experimental θ_B	$32.67 \pm 0.015°$	$32.84 \pm 0.03°$	$13.38 \pm 0.01°$
Bias	0.9%	0.4%	2%
FWHM	0.13°	0.13°	0.14°
Max. efficiency	1.25%	1.2%	3.4%

Table 5.6: Characteristics parameters of the three crystal measured by the ω scan.

From the table 5.6, we can see that the theoretical and experimental values of θ_B of the three crystals are in agreement. The rocking curve width of the three crystals is about 0.13°. The maximum reflection efficiencies of the toroidal and cylindrical crystals are 1.2% and 3.4%, respectively.

On the other hand, ω scans can also be used to check the meridional radius of curvature of crystal via the peak deviations $\delta\omega$ of the plots measured at different positions along the x axis, i.e. $Pos1$, $Pos4$ and $Pos5$. As illustrated in figure 5.16, the translation along x axis of a curved crystal results in the change of the orientation $\vec{n}$ of its lattice plane. Hence, to achieve the same Bragg angle at another position after the translation, an extra angle $\delta\omega$ of the rotation about the y axis is needed to compensate the orientation change, which leads to the peak deviation in the ω scan plot. The peak deviations $\delta\omega$ is related the meridional radius R_m of the curved crystal and the translation distance l. The relationship between the $\delta\omega$ in degrees, R_m and l is $\delta\omega = \frac{l}{2\pi R_m} \times 360°$. Conversely,

the R_m of curved crystal can be measured from the $\delta\omega$ of the ω scan plots. The $\delta\omega$ measured from the ω scan plots in figure 5.15 are given and compared to the theoretical value in the table 5.7.

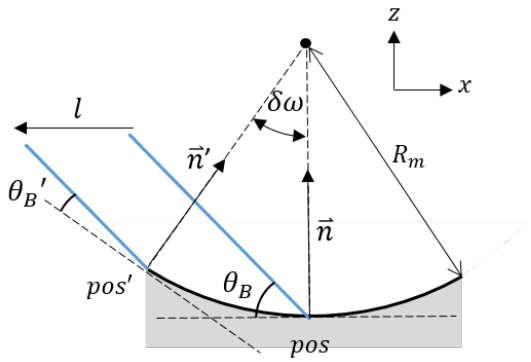

Figure 5.16: The original of the peak deviation $\delta\omega$ between different positions along the x axis: The translation l in the meridional plane leads to the orientation change of the lattice plane for a curved crystal, thus adding an offset to the relationship between ω and θ at the center of the crystal.

Toroidal 1 (Ge 400)		
	$Pos1/Pos4$	$Pos5/Pos1$
Theoretical $\delta\omega$	0.34°	0.68°
Experimental $\delta\omega$	0.37°	0.74°
Error	9%	9%
Toroidal 2 (Ge 400)		
	$Pos1/Pos4$	$Pos5/Pos1$
Theoretical $\delta\omega$	0.34°	0.68°
Experimental $\delta\omega$	0.39°	0.73°
Error	15%	7%
Cylindrical (Ge 111)		
	$Pos1/Pos4$	$Pos5/Pos1$
Theoretical $\delta\omega$	0.11°	0.22°
Experimental $\delta\omega$	0.14°	0.26°
Error	27%	18%

Table 5.7: Radii of curvature in the meridional plane of the three crystal measured by the ω scan.

The table 5.7 reflects that the meridional radii around the center of the three fabricated crystals are all in error with the designed values. Among them, the toroidal crystal 1 has the lowest error.

- χ **scan**

In this scan, the crystal is first rotated with an angle ω to make the incident angle of X-rays equal to the Bragg angle. The orientation of the detector remains $2\theta_B$. Then the crystal is tilted about the x axis with an angle χ. Figure 5.17 schematically illustrates the χ scan.

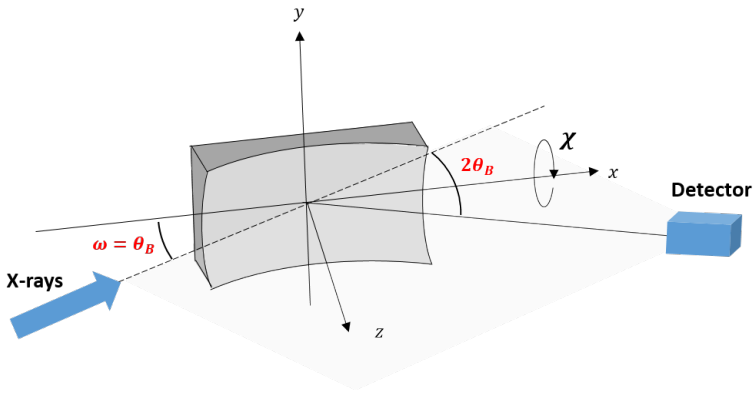

Figure 5.17: Schematic of χ scan configuration: The orientation of the detector is $2\theta_B$ with respect to the incident direction of X-ray. The crystal is rotated with an angle ω equal to the Bragg angle. During the scan, the crystal is tilted about x-axis. The rotation angle is χ.

The purpose of the χ scan is to check the radius of curvature in the sagittal plane. As the measurement of the meridional radius with the ω scan, the sagittal radius R_s can be measured from the peak deviation $\delta\chi$ of the χ plots detected at different positions along the y axis, i.e. $Pos1$, $Pos2$ and $Pos3$. The χ scan plots of the three crystals are shown in figure 5.18. Since the cylindrical crystal has not been curved in the sagittal plane, there is no deviation between its χ plots measured at different positions. The analysis about the sagittal radius R_s are given in the table 5.8.

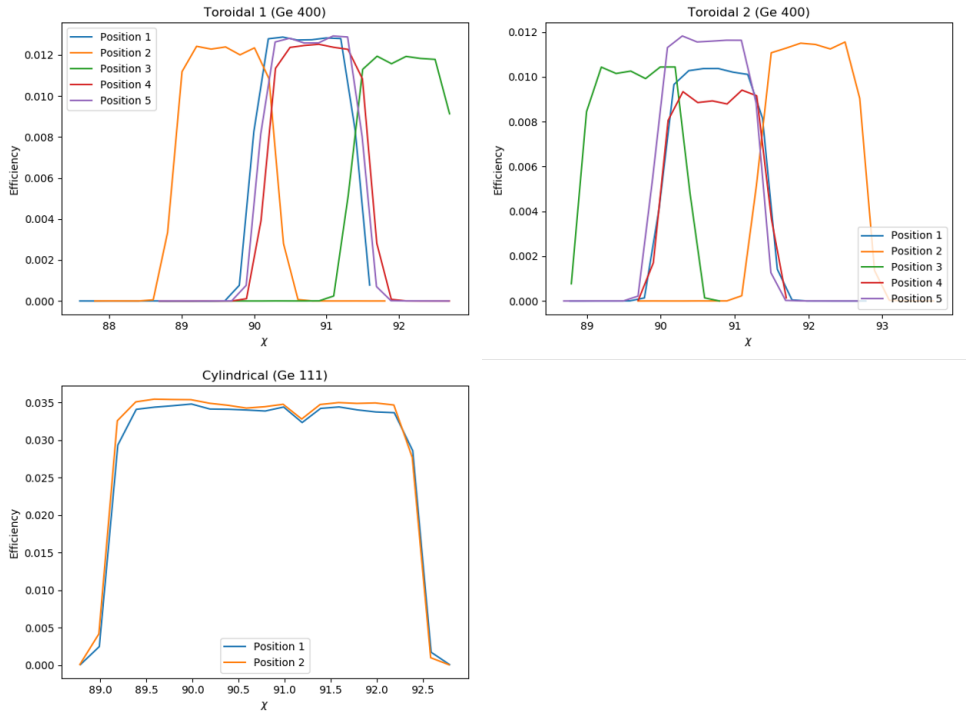

Figure 5.18: Plots of the χ scan measured at different positions on each of the three crystals.

Toroidal 1 (Ge 400)		
	$Pos1/Pos2$	$Pos3/Pos1$
Theoretical $\delta\chi$	1.14°	1.14°
Experimental $\delta\chi$	1.20°	1.20°
Error	5%	5%
Toroidal 2 (Ge 400)		
	$Pos1/Pos2$	$Pos3/Pos1$
Theoretical $\delta\chi$	1.14°	1.14°
Experimental $\delta\chi$	1.10°	1.25°
Error	4%	10%
Cylindrical (Ge 111)		
	$Pos1/Pos2$	$Pos3/Pos1$
Theoretical $\delta\chi$	0°	0°
Experimental $\delta\chi$	0°	0°
Error	0%	0%

Table 5.8: Radii of curvature in the sagittal plane of the three crystal measured by the χ scan.

As displayed in the table 5.8, the theoretical and the experimental $\delta\chi$ between different positions along y axis are close to each other for all the three crystals, indicating that the sagittal radii of the three crystals are consistent with the design value.

- $\theta - 2\theta$ **scan**

Similar to the ω scan in figure 5.14, the crystal rotates about the y axis, leading to the change of the incident angle θ. And the detector is no longer fixed, but rotates with the incident beam of an angle 2θ, the corresponding reflection direction. The purpose of this scan is to verify the lattice of crystal. The experimental $\theta - 2\theta$ plots at the five positions of the three crystals are given in the figure 5.19.

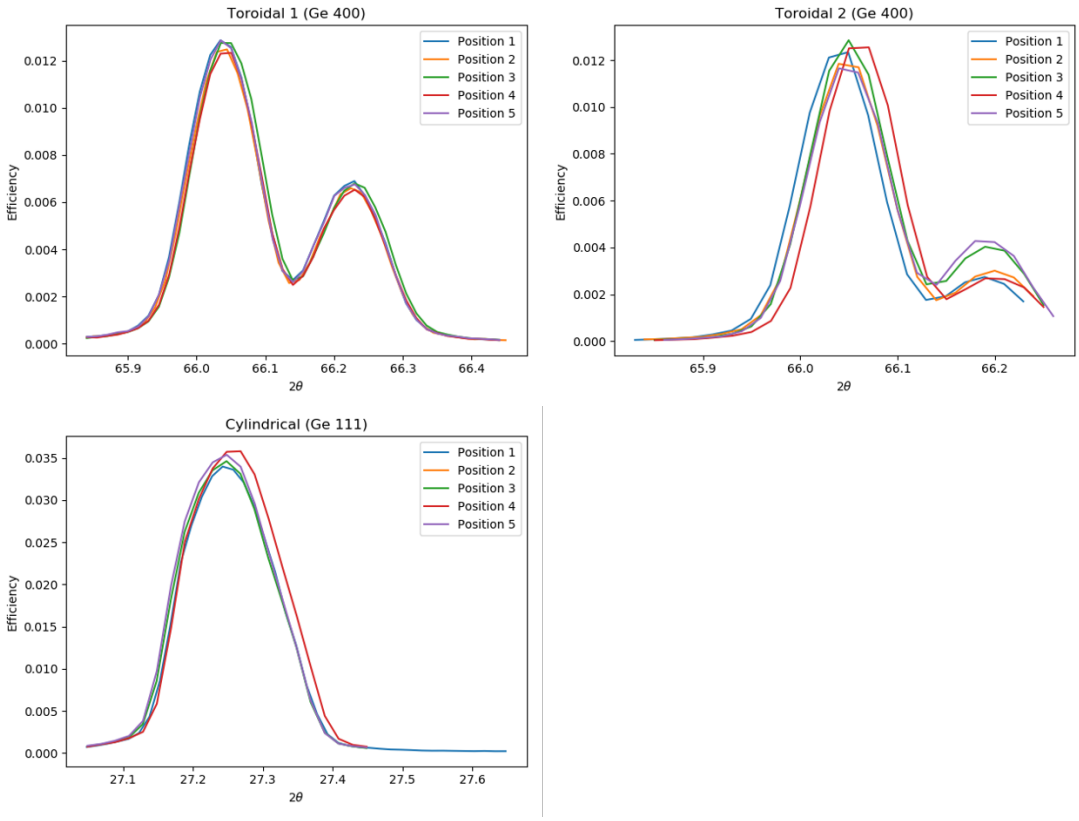

Figure 5.19: Plots of the $\theta - 2\theta$ scan measured at five different positions on each of the three crystals.

Since each crystal consists of only one lattice structure, there should be only one peak in their plots of the ω scan under the monochromatic source. In our measurement, the experimental source contains two wavelengths, 1.540 Å and 1.544 Å. The difference of wavelengths leads to a variation of 0.19° in $2\theta_B$ for the two toroidal crystals (Ge 400). Therefore, two peaks appear in the $\theta - 2\theta$ plots of the two toroidal crystals, and the deviation between the two peaks is consistent with the theoretical value. The lattice spacing $2d$ of the cylindrical crystal (Ge 111) is much larger than that of the toroidal crystals (Ge 400) (see the table 5.5). Consequently, the peak deviation caused by the different wavelengths is only 0.07° for the cylindrical crystal, which exceeds the resolution of the instrument. Hence, only one peak can be seen in the $\theta - 2\theta$ plots of the cylindrical crystal. The results of the $\theta - 2\theta$ scan show that there are no obvious defects of lattice plane in the detection zones of the three crystals.

In summary, through the three different XRD scans, we verified the meridional and sagittal radii of the three curved crystals, consistent with the designed geometries. The Bragg angle practically measured with the wavelength 1.540 Å of the toroidal 1, toroidal 2 and cylindrical crystals are 32.67°, 32.84° and 13.38°, respectively. The FWHM of the rocking curve of these three crystal are about 0.13°. The reflection efficiencies at θ_B of the toroidal crystals and the cylindrical crystal are 1.25% and 3.4%, respectively. And the lattice parameters of the three crystals are uniform in the detection zones around the centre.

5.10 Preliminary testing of toroidal crystal focal spot

The quality of focal spot of the optical element as the main lens is crucial to the imaging system. In this section, we will thus experimentally investigate the focal spot of the toroidal crystal (Toroidal 1 (Ge 400)).

We mounted the toroidal crystal in the imaging system shown in figure 5.20. The source energy is approximately 8 keV generated by a X-ray tube with a copper anode set at a voltage of 50 kV. The source size is about 150 μm. The detector section is a visible light CCD camera cooled to $-15°$, coupled with a luminescent Ce:YAG (YAG doped

with cerium) crystal of 2 mm thickness and an objective. The effective pixel size in the Ce:YAG crystal plane is 2.2 μm. The X-ray source, the toroidal crystal and the detector are all along the Rowland circle. The distances between the three satisfy the focus-to-focus configuration. The orientations and the positions of X-ray source and the detector are fixed. The incident angle θ of X-rays can be changed by rotating the toroidal crystal in the meridional plane. The spot of intense diffraction has been found around the experimentally measured Bragg angle 32.67°.

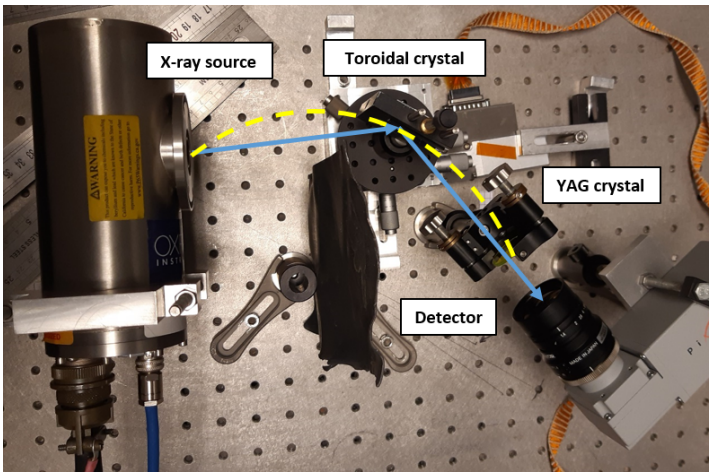

Figure 5.20: Experimental set-up with the toroidal crystal as imaging lens: The yellow dashed arc is the Rowland circle. The blue lines represent the path of X-rays. The source and the detector are both fixed and oriented to the direction forming the Bragg angle with the tangent line at the crystal center.

Figure 5.21 displays a fine focal spot scan with the incident angles around the Bragg angle 32.67° measured by the ω scan of XRD (see table 5.6). Each image was acquired with an exposure time of 1s. The difference of the incident angle between two sequential images is 0.005°.

Unlike the previous ω scan of XRD, which illuminated only a small zone of the crystal, the X-ray source used in this test is sufficiently divergent to illuminate the entire surface of the crystal. We first examine the diffraction response of the entire crystal with the incident angle θ of X-rays. The diffraction response of the entire crystal is estimated by the integrated intensity difference between the area of 50 $pixels \times 65$ $pixels$ covering the focal spot and the same size area of background, in order to remove the noise (see

figure 5.22 (a)). As shown in figure 5.22 (b), the integrated intensity of the focal spot remains constant in a range of 0.04° near the Bragg angle, and then decreases rapidly in the resulting plot. The resulting plot generally validates the Bragg angle previously measured on the entire crystal and reflects that the toroidal crystal has a high sensitivity to the incident angle.

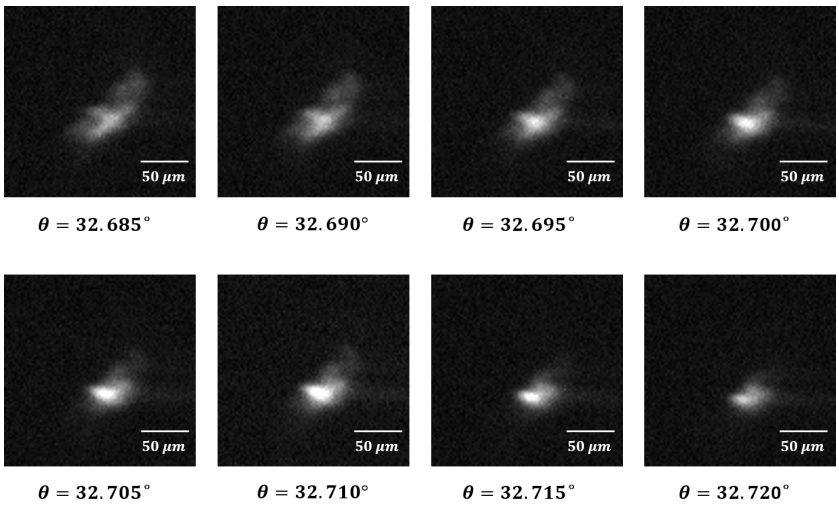

Figure 5.21: Scan of focal spot with varying incident angle θ: The exposure time of each image is $1s$. The difference of the incident angle between two sequential images is 0.005°.

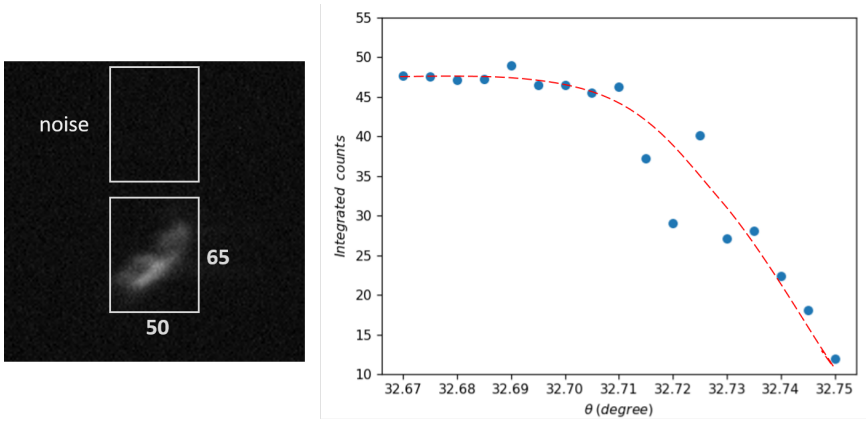

(a) **(b)**

Figure 5.22: Diffraction response of the entire crystal with the incident angle θ: (a) the diffraction response of the crystal is estimated by the integrated intensity of a 50 *pixels* × 65 *pixels* covering the focal spot with noise correction. (b) Plot of integrated intensity versus θ.

We further inspected the shape evolution of the focal spot along the incident angle θ. From figure 5.21, we can see that as the incident angle is adjusted, the initial elliptical large spot is gradually focused into a more circular bright spot. This shape evolution is more visible by comparing the relative change in the length and width of the focal spot. The length and width of the focal spot are estimated by the FWHMs of the intensity plots along its major and minor axes, as illustrated in figure 5.23 (a). Figure 5.23 (b) provides the scatter map of the length and width of the focal spot along θ.

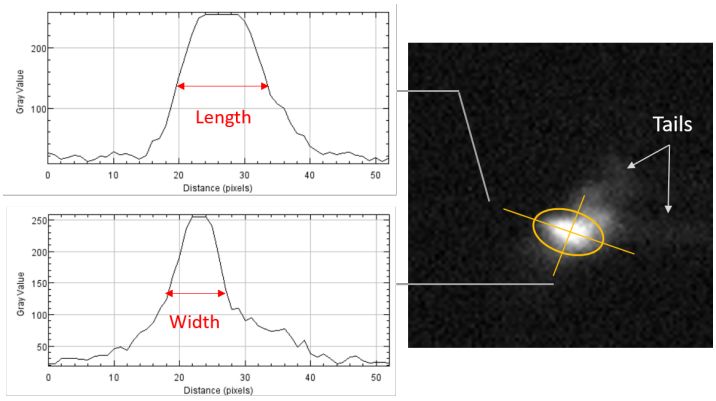

(a)

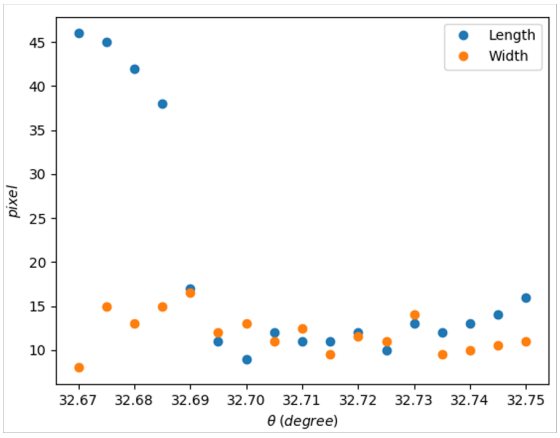

(b)

Figure 5.23: Shape evolution of the focal spot: (a) The length and width of the focal spot are measured from the FWHMs of the intensity plots along its major and minor axes drawn by the yellow lines. The tails of the main bright spot come from the coma aberration. (b) Scatter map of the length and width of the focal spot versus θ.

From the data in figure 5.23 (b), it is apparent that the length and width of the focal point converge with adjustment of the incident angle. Elliptical distortion of the focal spot is a characteristic of astigmatism. The reduction of the elliptical aberration verifies the geometry of the toroidal crystal, which is originally designed to eliminate astigmatism. On the other hand, the elliptical aberration varied with the incident angle indicates the misalignment between the source and crystal. The length and width of the focal spot at $\theta = 32.710^\circ$ are approximately 26.26 μm and 19.8 μm. As pointed out by the white arrows in figure 5.23 (a), another remark on the focal spot is the two tails that accompany the main bright spot. These two tails reflect the coma aberration of the focal spot, which is produced by the off-axis incident rays and always occurs in concave mirror imaging. The coma aberration can be significantly improved by reducing the crystal aperture.

In order to have a general idea of the impact of the vertical tilt of the toroidal crystal on the focal spot, we performed another scan by rotating the crystal in the sagittal plane. For the simplicity of manipulation, this focus scan was carried out with a green laser diode source. Although for X-rays and laser the reflection mechanism of the curved crystal is not exactly the same, they both obey the law of specular reflection. The laser was situated at the focus on the Rowland circle and magnified by a lens, shining a 2 cm long by 1 cm wide central zone of the toroidal crystal. The chief ray of the laser arrived at the center of crystal with the Bragg angle 32.67° to imitate the behavior of X-rays. The whiteboard screen, perpendicular to the reflection direction, was placed about 1 m away from the crystal far behind the focal spot. If the focal spot of the crystal is roughly a point, we should see a mirror image of the crystal surface shape on the screen, according to the linear propagation of light. Hence, the similarity between the image and the crystal surface shape can indirectly reflect the focal spot quality.

Three photos of the toroidal crystal images with slightly different vertical tilts are exhibited in figure 5.24.

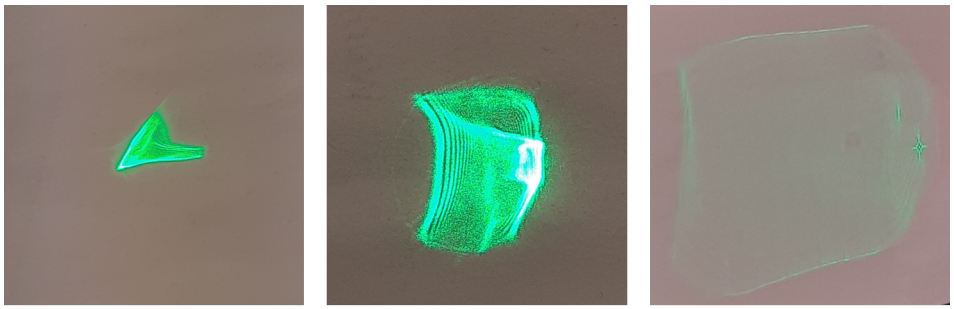

(a) **(b)** **(c)**

Figure 5.24: Three photos of the toroidal crystal images with slightly different vertical tilt: The three image were taken after the focus with a green laser source.

From figure 5.24(a) to (c), the image becomes increasingly similar to the crystal surface shape, suggesting the reduction in misalignment and the improvement in focal spot. Large differences in the shape between the images in figure 5.24 reflects that the small variation in the vertical tilt completely changes the focal spot shape formed by the toroidal crystal.

5.11 Conclusion

The work presented in this chapter was carried out under the overarching purpose of finding an X-ray optics with large aperture numerical to serve as the main lens in an X-ray plenoptic camera. The toroidally curved crystal has been proposed as the main lens for its large diffracting area and imaging property. The imaging performance of curved crystal is highly dependent on its internal and external structure. Therefore, a ray-tracing algorithm has been developed to deal with the geometry design of the curved crystal and estimate the focal spot. The simulation results of toroidal crystal carried out with the ray-tracing algorithm confirm its focusing ability. The toroidal crystals have been fabricated after the numerical verification. The measurements of these crystals performed on a 4-circle diffractometer indicate that their structures are consistent with the design. The recent testing on the focal spot of one of the toroidal crystals, reported in the last section of this chapter, shows the importance of the precise

alignment of the crystal used as imaging lens in the imaging system. More experimental tests are needed for the application of toroidal crystal in a light field imaging system.

Chapter 6

Experimental Work On X-ray Light Field Imaging Systems

In the previous chapters, we delved into the principle of light field and discussed the associated reconstruction algorithms. We theoretically and numerically studied two possible X-ray optics to prototype an X-ray plenoptic camera. Based on these studies, we experimentally set up and tested two FZP[1]-based light field imaging systems at two different X-ray energies. This chapter is divided into two parts to present these two experiments.

6.1 Experimental construction of X-ray light field microscope in "water window"

Starting from the first achievement of the light field microscope by Levoy, Marc and coworkers in 2006 [103], many articles have applied it to biomedical research, especially in the field of neuroscience [104] [105] [106]. However, previous published studies of light field microscope are sill limited to visible light. To construct a soft X-ray light field microscope (XLFM), we integrated a FZP array into the X-ray microscope reported in [107], forming the FZP-based plenoptic camera discussed in Chapter 4. The sketch of the proposed XLFM is displayed in figure 6.1.

[1]FZP is the abbreviation of Fresnel zone plate

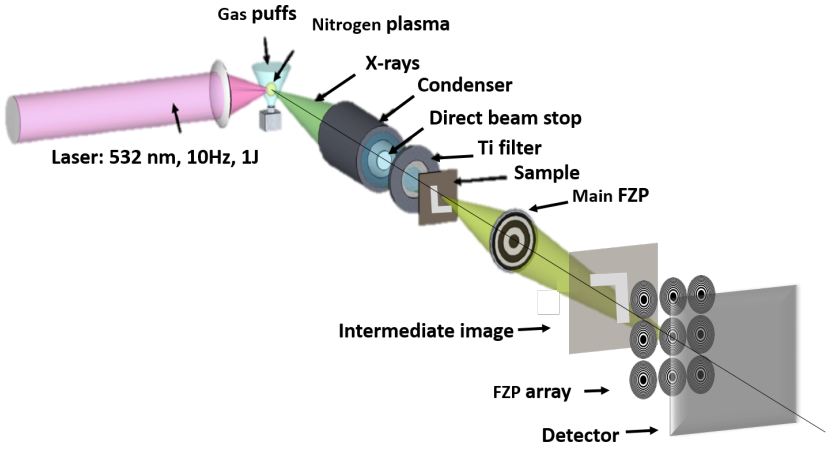

Figure 6.1: Sketch of XLFM: The XLFM is constructed by integrating an FZP array into a water window microscope using laser-plasma source.

For X-ray biological cellular imaging, the proposed XLFM is designed to operate in the so-called "water window" range (wavelength of 2.3 $-$ 4.4 nm). The "water window", extending from the K-absorption edge of carbon at 533 eV to the K-absorption edge of oxygen at 282 eV, results in the significant difference in absorption coefficients of biological specimen constituents: water (oxygen) and protein and lipids, etc. (carbon). Hence, for the X-rays in the "water window", water is relatively transparent, while carbon is absorbing, which provides high contrast.

We attempted to build an experimental XLFM at Laboratoire d'Optique Apliquée. The experimental set-up under construction will be described from the source to the detector along the propagation direction of X-ray beam. Figure 6.2 shows the experimental setup for imaging tests with the main FZP only.

We employs a desktop laser-plasma source to generate the "water window" X-rays. In detail, a pulsed Nd:YAG pumping laser (wavelength of 532 nm, pulses duration of 5 ns, repetition rate of 10 Hz and pulse energy of 1 J) is focused onto the nitrogen puff target. The nitrogen puff is released from the piezoelectric nozzle synchronized with the laser. The plasma is induced by the inverse bremsstrahlung absorption occurring in the interaction between the laser and the nitrogen gas. The nitrogen plasma has a broad spectrum radiation with emission peaks located in the "water window". The generated

radiation is further filtered by a 200 nm thick titanium (Ti) foil mainly transmitting the line at 2.88 nm (equivalent to the energy of 430 eV), allowing to obtain a quasi-monochromatic X-ray source [108].

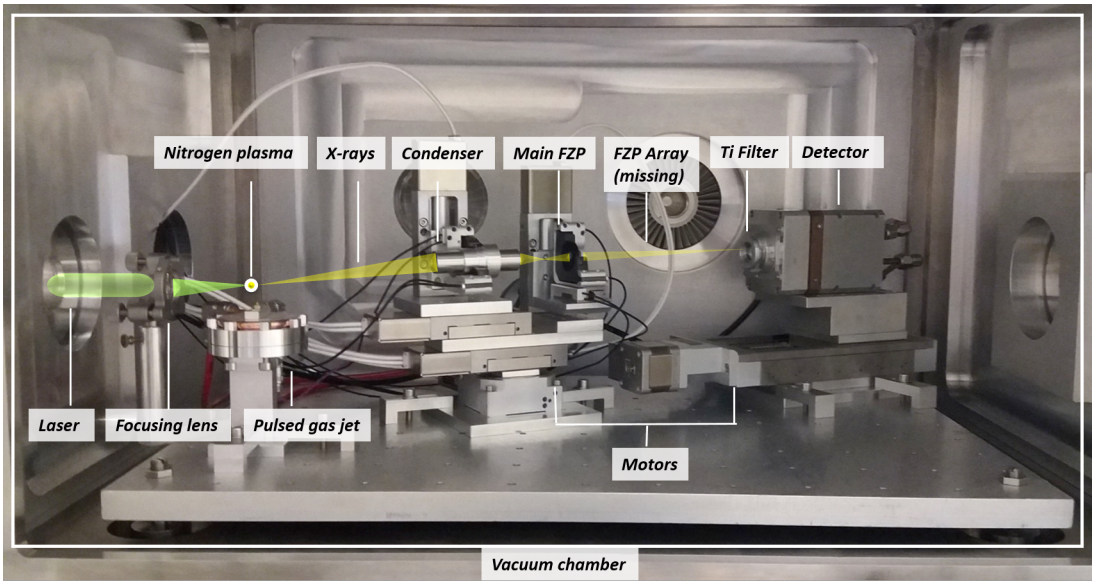

Figure 6.2: Photo of the experimental set-up in the "water window" range: The entire system including the laser-plasma source is installed in the vacuum chamber enveloped by the white rectangle. The FZP array has not been mounted in the photo. The optical axis of the imaging system is deviated from the propagation direction of the pump laser, to avoid laser damage.

Both the generation of the laser-plasma source and the propagation of the X-rays with a 2.88 nm wavelength require vacuum experimental condition. Therefore, the entire experimental set-up is installed in a vacuum chamber of background pressure about 10^{-5} $mbar$. The length of the vacuum chamber also limits the length of the main part of the system shown in figure 6.1 to less than 600 mm.

The generated radiation from the nitrogen plasma is then collected by the condenser, an ellipsoidal nickel-coated mirror coupled with a central stop blocking the direct beam. The sample is placed in the focal plane of the condenser. Different from the location shown in figure 6.1, the Ti filter is moved to the front of the detector. As the experimental set-up is mounted in a vacuum chamber with very reflective metal walls, placing

the Ti filter in the entrance of the detector can better remove the scattered laser.

Next, the illuminated sample is imaged by the FZP-based plenoptic camera consisting of main FZP, FZP array and detector. The main lens is a FZP containing 4473 zones, with a diameter of 320 μm and a focal length of 2.00 mm for the X-rays of 2.88 nm wavelength. The outermost zone width is 18 nm, namely the theoretically achievable resolution is up to 18 nm.

The FZP array composed of 20×20 sub-FZP is placed in the focal plane of the main FZP. The number of zones of each sub-FZP is 5, which may lead to low contrast referring to the simulation results discussed in Chapter 4. The diameter, the outermost zone width and the focal length of each sub-FZP are 32 μm and 1.69 μm, respectively. The focal length of the sub-FZP for the X-rays with a 2.88 nm wavelength is equal to 17.78 mm.

The detector, situated in the focal plane of the FZP array, is a back-thinned CCD camera with water cooling, capable of directly recording of soft X-rays in vacuum. The CCD camera consists of 2048×2048 pixels. The pixel size is 13.5 μm.

In order to facilitate the precise alignment in vacuum, the motors are installed for the condenser, the main FZP and detector. The assembly of the condenser and the main FZP is allowed to rotate in the horizontal plane and the translate along the X-rays propagation direction. The distances between the condenser and the main FZP is also adjustable by the extra translation motor below the condenser. In addition, both the condenser and the main FZP have the flexibility in the height and two directions tilts. The distance between the main FZP and the detector can be further changed by the translation of the detector.

The key parameters of the experimental imaging materials mentioned above are summarised in the table 6.1.

The construction of the experimental XLFM is challenging and requires the multidisciplinary knowledge. The experimental set-up is a combination of several systems, such as the vacuum pumping and detection, the water cooling for the nozzle of gas and the camera, the synchronization between the laser pulse and the gas puff, the laser-

plasma focusing, the motorisation and the light field imaging. At the current stage, we are still testing the laser-plasma source. The laser-plasma is hard to attain. The filtered emission spectrum of the experimental nitrogen plasma need to be validated in future work by comparing with the reported result in the literature [109].

Main FZP		20×20 **FZP array**		**CCD camera**	
Diameter	320 μm	Diameter	32 μm	Filter material	Titanium
1st order focal length	2.00 mm	1st order focal length	17.78 mm	Filter thickness	200 nm
Outermost zone width	18 nm	Outermost zone width	1.69 μm	Number of pixels	2048×2048
Number of Zones	4473	Number of Zones	5	Pixels size	13.5 μm
		FZP array spacing	37 μm		

Table 6.1: Overview of the key parameters of the experimental imaging materials. The given focal lengths of the main FZP and the FZP array in the table are calculated for the X-rays at 430 eV with a wavelength of 2.88 nm.

6.2 Experiment with synchrotron radiation at 11 keV

The second experiment was realized on the imaging beamline P05 of the third generation storage ring PETRA III at the Deutsches Elektronen-Synchrotron (DESY) in Germany. The purpose of the experiments was to test the feasibility of realizing the plenoptic camera in hard X-ray and to explore its performances. The following part of this chapter is dedicated to presenting all the details and findings of this experimental work. It begins with describing the experimental equipment and image acquisition method. It then continues with a discussion of light field image processing. Before image reconstruction, several basic performance parameters of the experimental set-up are examined. Next, experimental refocusing results at different distances are displayed and investigated. The resolution and the depth information extracted from the experimental light field data are analysed in the end.

6.2.1 Experiment materials and set-up

The implementation of X-ray plenoptic camera in this experiment is based on the use of Fresnel Zone Plate (FZP). The main components of the X-ray plenoptic camera are the main lens and the micro-lens array.

The sketch of the main structure of the experimental set-up is illustrated in figure 6.3. And the table 6.2 gives an overview of the principal parameters of the experimental devices. In the following, each of the main components of the experimental set-up will be introduced in detail along the propagation direction of X-ray (from left to right in figure 6.3). With the experimental geometry, the image of the sample from the main FZP is formed before the FZP array, marked as the intermediate image in the sketch. The intermediate image is further imaged by the FZP array and relayed to the detector located approximately in the image plane of the FZP array.

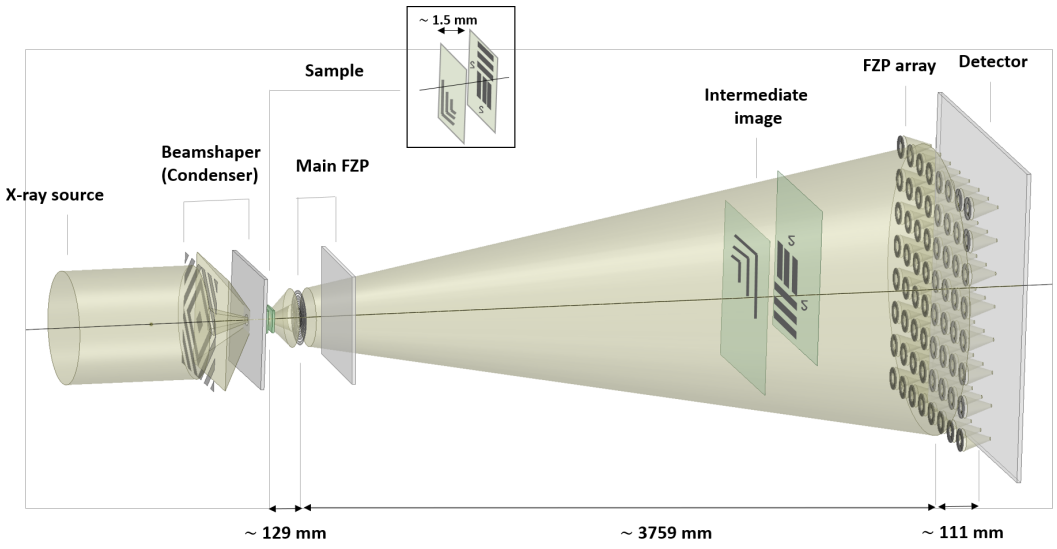

Figure 6.3: Sketch of the experimental X-ray plenoptic camera: along the direction of X-ray propagation, from left to right, there are the beamshaper, the sample, the main FZP, the FZP array and the detector.

Main FZP		9×9 **FZP array**		**Scintillator coupled PCO camera**	
Diameter	280 μm	Diameter	100 μm	Scintillator material	LuAG(Ce)
1st order focal length	124.21 mm	1st order focal length	88.72 mm	Scintillator thickness	50 μm
Outermost zone width	50 nm	Outermost zone width	100 nm	Number of pixels	2048×2048
Number of Zones	1400	Number of Zones	250	Pixels size	6.5 μm
		FZP array spacing	110 μm		

Table 6.2: Overview of the principal parameters of the experimental devices. The given focal lengths of the main FZP and the FZP array in the table are calculated for the X-rays at 11 keV.

6.2.1.1 X-ray source and beamshaper

The experimental operating energy of the X-ray beam is 11 keV, corresponding to a wavelength of 1.127 Å. The X-ray is radiated as the accelerated electron beam from the storage ring traverses the undulator. X-rays from such radiation are intense and concentrated in narrow energy band. The emitted X-ray beam, passing through slits and filters, is firstly directed to the optics hutch with monochromators. Then the optimised X-ray beam enters the experiment hutch approximately parallel. The incoming X-ray beam is further focused into a homogeneous and bright 50 $\mu m \times 50$ μm square spot by the beamshaper. The beamshaper is a Fresnel zone plate with specially designed square-like pattern and equipped with center stop and order sorting aperture. The beamshaper works as a condenser and generates the quasi Köhler illumination in the plane of the sample. More details about the source section of the beamline P05 are provided in [110].

6.2.1.2 Sample

The sample used in the experiment is composed of two classical resolution test targets for X-ray imaging, consisting of nested L-shaped pattern and USAF target pattern. The two targets can be regarded as two separate planes with a spacing of about $1 - 1.3$ mm, placed approximately 129 mm away from the main FZP. The target closer to the main FZP is denoted as T1 and the farther one is denoted as T2. The test pattern of each

target and their relative spatial position are shown in figure 6.4. Figure 6.4(a) shows the reference image of the targets test pattern. Figure 6.4 (b) and (c) are the images respectively focused on the T1 and T2, acquired by the main FZP and the detector only. The focus change between figure 6.4 (b) and (c) is achieved by changing the distance of the targets from the main FZP.

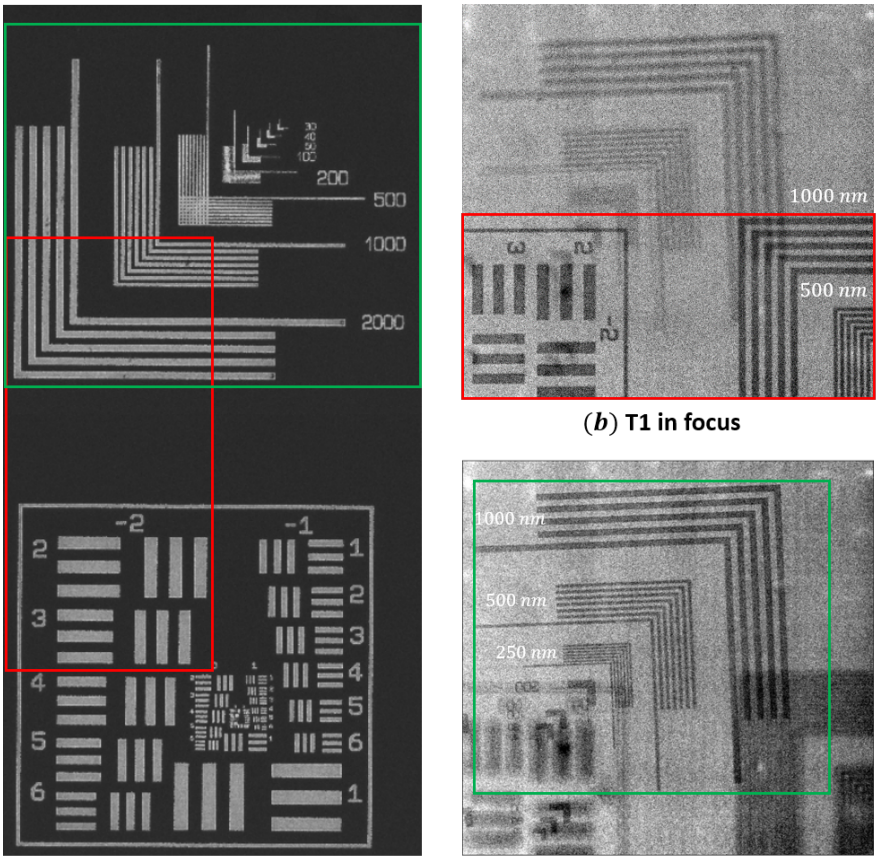

(*a*) **Test Pattern**

(*b*) **T1 in focus**

(*c*) **T2 in focus**

Figure 6.4: (a) Test pattern is consisted of nested Ls and USAF target. The numbers next to the nested Ls indicate the line pair width of each group in *nm*. The red and green rectangles correspond to the parts of T1 and T2, which can been seen via the detector. (b) and (c) Horizontally flipped images of the sample taken with the main FZP and the detector only, respectively focused at T1 and T2 plane. The line width (half of the line pair width) of the Ls patterns within the FoV of the camera are marked in white.

6.2.1.3 Main FZP and FZP array

The principle parameters of the main FZP and the FZP array used in the experiment are given in the table 6.2. Since the direct beam is blocked by the center stop of the beamshaper, the main FZP is equipped only with the order sorting aperture, i.e., the gray plate behind the main FZP in figure 6.3, to block the high order beams other than the first order.

The FZP array contains 9×9 sub-FZPs arranged in a square grid with the spacing of 110 μm. And the corresponding center stop array in gold is placed downstream of the FZP array, as close as possible to the FZP array. The diameter of each center stop is approximately $\frac{1}{3}$ of the sub-FZP diameter, which is about 33 μm. The visible light microscope images of the FZP array and its center stop array are shown in figure 6.5 (a) and (b), respectively.

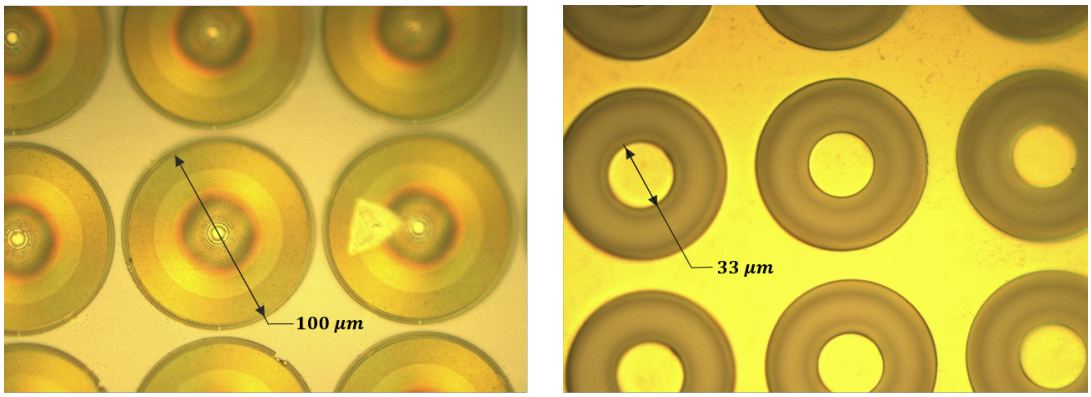

(a) **(b)**

Figure 6.5: Microscope images of the experimental FZP array and its center stop array: (a) FZP array and (b) center stop array. The sub-FZPs and the center stops are arranged into the same square grid with the spacing of 110 μm. The diameters of each micro-FZP and center stop are 100 μm and 33 μm, respectively. And the yellow color of the images comes from its own gold composition.

6.2.1.4 Detector

The detector is composed of a LuAG(Ce) scintillator crystal, an objective with adjustable 10× magnification and a PCO.edge 4.2 CMOS camera. The basic parameters

of the detector are given in the table 6.2. The scintillator, placed around the image plane of the FZP array, firstly converts the incoming X-ray into visible light (maximum emission at a wavelength of about $535nm$). Then the objective relays the visible image with a magnification onto the sensor of the PCO camera. Figure 6.6 shows the photo of the experimental detector section.

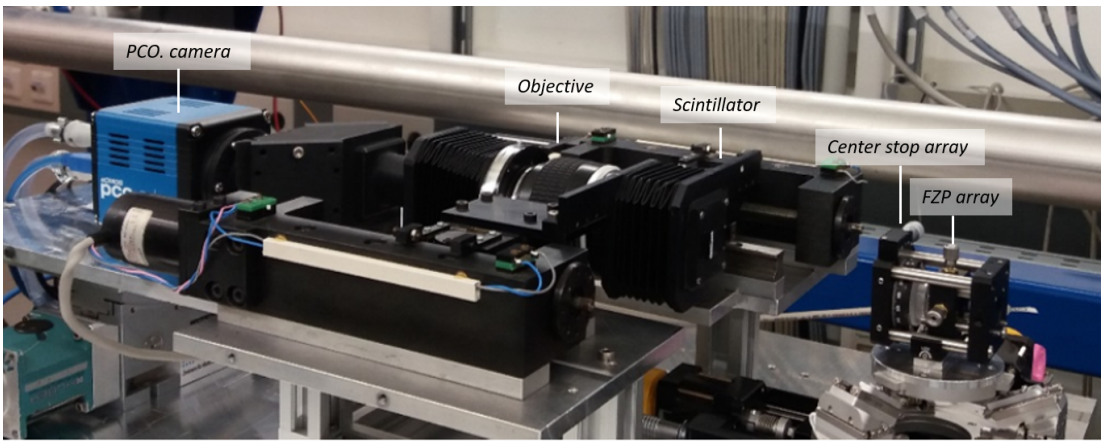

Figure 6.6: Photo of the experimental detector: the detector consists of a scintillator crystal, an objective with adjustable 10× magnification and a PCO.edge 4.2 CMOS camera. The X-ray image from the FZP array is firstly converted into visible light image via the scintillator. Then, the visible light image is relayed with a magnification by the objective and acquired by the sensor of the camera.

6.2.1.5 Set-up installation

We began with the alignment of the beamshaper, the main FZP and the detector. The sample was then mounted near the focus of the beamshaper. The main FZP was moved 128 mm away from the sample and the detector system was set to the designed position of the intermediate image. Next, slightly adjusting the sample distance by a motorized stage, a focus scan was performed to find the sharpest intermediate image on the detector. According to the position of the sharpest intermediate image of $T1$, the FZP array was inserted to the assigned position. And the detector was moved to about 111 mm away from the FZP array.

6.2.2 Data collection

6.2.2.1 Image stitching acquisition

There are three points to note about the experimental set-up: Firstly, the total size of the FZP array is about 990 μm, which is 20 times larger than the 50 μm wide illumination. The significant difference in size between the illumination and the FZP array makes it essential to place the FZP array far away from the main FZP, consequently resulting in very small numerical aperture ($NA = 3.7 \times 10^{-5}$) of each FZP in the experimental array. Secondly, each FZP in the experimental array is quite large relative to the main FZP, approximately $\frac{1}{3}$ the size of the main FZP. Finally, compared to the microlens array in visible light plenoptic camera typically consisting of more than 1000×1000 microlenses, the FZP array in the experimental X-ray set-up has a very limited number of microlens 9×9. In the object plane, these facts lead to the gaps that are not covered by the FZP array and the extremely low sampling rate.

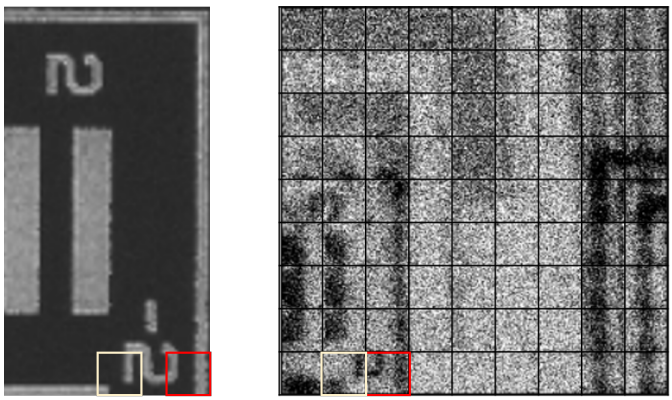

(***a***) (***b***)

Figure 6.7: Inadequate sampling problem of the experimental set-up: (a) Zoomed part of the test pattern imaged in the left lower corner of (b). (b) Light field image extracted from the experimental set-up with 9×9 FZP array. The black blocks divide the light field image according to the FZPs in the array. The white and red blocks indicate the zones of test pattern imaged by two adjacent FZPs in (a) and their micro-images in (b). The gap between the white and red blocks in (a) is an example of the gaps that are not covered by the FZP array in the object plane.

Figure 6.7 (a) displays the part of the test pattern corresponding to the left lower corner of the light field image in figure 6.7 (b), which is extracted from the raw image acquired by the experimental set-up with 9×9 FZP array. The numerical processing from the raw image to the light field image will be described in details in section 6.2.4.
The micro-images in each black block in figure 6.7 come from different single FZP of the array. For the ease of comparison, each micro-image has been flipped. The mentioned gaps in the object plane can be seen well from the micro-images of the numbers in the test pattern. The white and red blocks in figure 6.7 (a) and (b) indicate the zones of the test pattern (i.e. FoV) imaged by two adjacent FZPs of the array and the corresponding micro-images. We can notice that the image of the number -2 is partially missing. The discontinuity in the FoV of neighboring FZPs implies the inadequate sampling problem of the experimental set-up with only 9×9 FZP array.

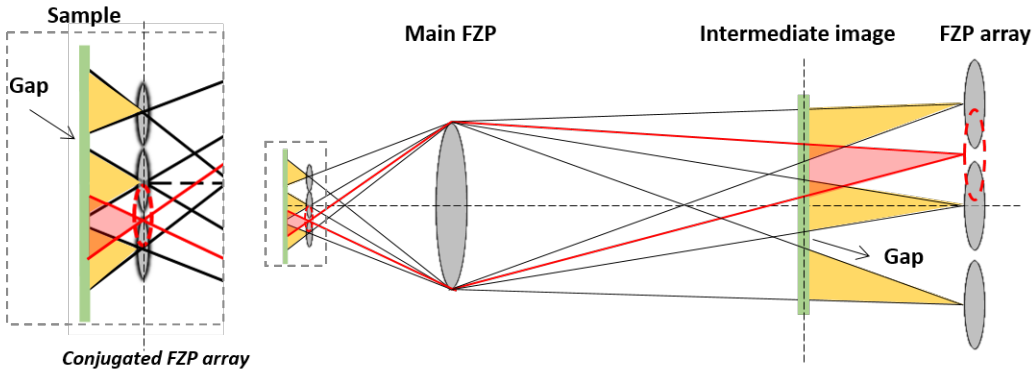

Figure 6.8: Schematic optical path diagram of the experimental set-up: For the clarity of the figure, the 9×9 FZP array is s not entirely drawn and the distance between the main FZP and the FZP array has been greatly reduced. Because the main FZP and the FZP array are far apart and their difference in dimensions is not large, each FZP in the array consequently has extremely small NA and non-adjacent FoV in the object plane. The FoV of each FZP of the array is colored in yellow. The arrow indicates the gap of the FoV between two adjacent FZPs. the red dashed circle represents a FZP at a stitching position that fills the gaps.

Figure 6.8 illustrates the formation of the gaps through the schematic optical path diagram of the experimental set-up. The conjugated FZP array in the object space is zoomed in the inset on the left. For the clarity of the figure, the 9×9 FZP array is not

entirely drawn and the distance between the main FZP and the FZP array has been greatly reduced. The imaging zones of the FZP array are colored in yellow.

In order to overcome the inadequate sampling problem under the limitation of the experimental set-up, we acquired the images with the FZP array translated to different positions in the assigned plane and then numerically merged them into one single light field image. The image taken with the FZP array moved less than one inter-lens spacing will cover the FoV gap of the FZP array at the initial position, as illustrated by the red dashed lens in figure 6.8. This acquisition method, so-called stitching, is widely used in X-ray imaging to extend the limited FoV of imaging system.

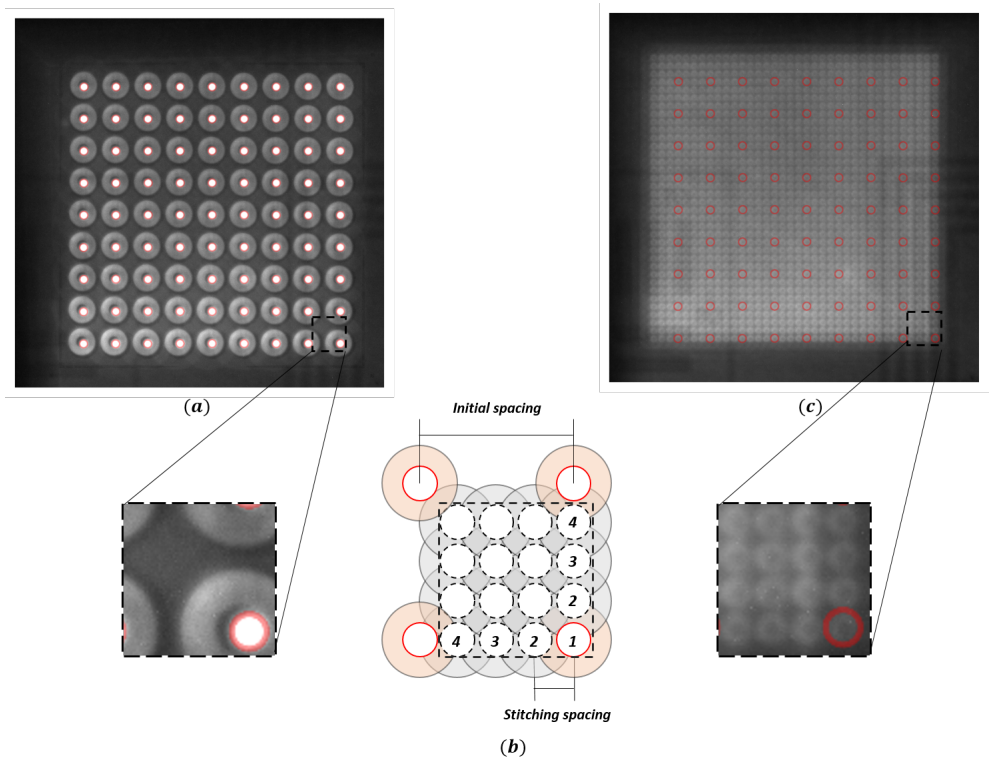

Figure 6.9: Image stitching: (a) is the the image taken with the 9×9 FZP array at one position. And (c) is the stitching image merging the images of the FZP array at 16 different positions. Their insets show the same enlarged unit cell of the FZP array delimited by the dashed square. (b) schematically illustrates the stitching method. The movement of the FZP array can be represented by the the change in position of the lower right vertex FZP within a unit cell. The red circles are the images of the initial FZP array, and the black dashed circles indicate the images added by stitching.

In the experiment, the initial unit cell of the FZP array has been divided into a 4×4 grid. Combining the first order images of the FZP array at these 16 positions, it allows to generate a more compact light field image with 36×36 adjacent and non-overlapping micro-images (see figure 6.9). With the image stitching method, the inter-lens spacing is equivalently reduced to 27.5 μm, equal to a quarter of the initial spacing of the FZP array. Figure 6.9 (a) and (c) display the image from the FZP array at one single position and the combined image of the stitching acquisition, respectively. The red circles indicate the FZPs of the initial array, which help to understand the formation of the stitching image. And the black dashed squares in figure 6.9 (a) and (c) delimit the same unit cell of the FZP array, enlarged in the insets. The stitching operation of the FZP array can be succinctly represented by the change in position of the lower right corner FZP in this unit cell, as schematically illustrated in figure 6.9 (b).

6.2.2.2 Images acquisition for flat-field correction

X-ray images generally suffer from systemic noise stemming from beam instability, scintillator imperfection, detector response variation, etc. A common method to manage the noise and improve the X-ray image quality is flat-field correction [111]. This correction is achieved by normalizing the captured raw image of sample with additional acquired reference images without sample, which is often referred to as flat-field image. For the application of the flat-field correction in the post image processing, 10 raw images and 4 flat-field images are acquired in each stitching position. The exposure time for each image is 5 seconds, thus the total acquisition time for a complete dataset consisting of 16 stitching positions is 1120 seconds in the experiment.

6.2.3 Raw image interpretation

As previously described in 4.3, FZP produces different orders images in the same time. FZP is employed for both major parts of the experimental set-up, thus generating composite raw images. An example of raw image is shown in figure 6.10. In more detail, it is the average image of 10 raw images with 5-second exposure time each, acquired at

one single stitching position of the FZP array.

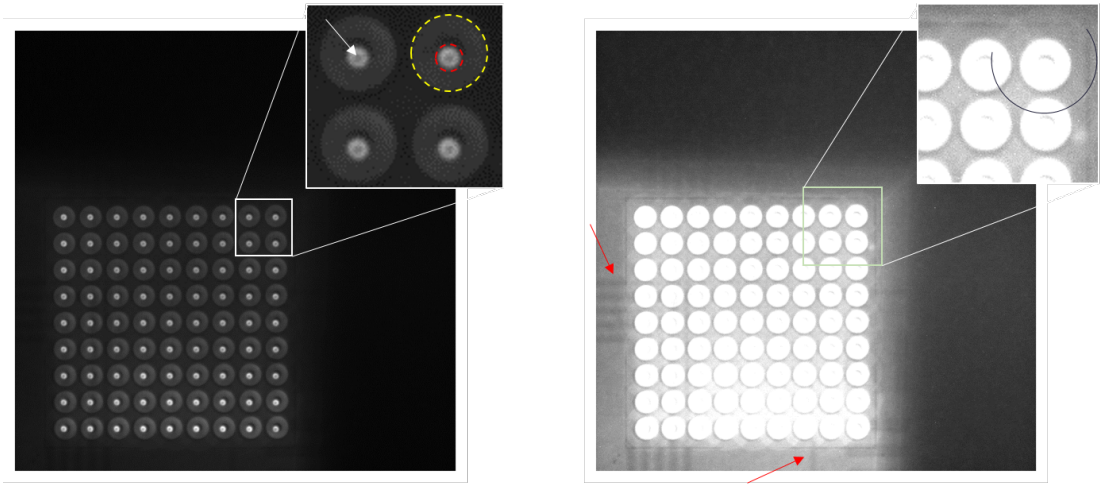

(***a***) (***b***)

Figure 6.10: Interpretation of raw images: (a) displayed the direct image from the experimental plenoptic camera. The yellow and red dashed circles mark the $0th$ and the $1st$ images from one FZP of the array. And the white arrow point to the shadow from the center stop of the FZP array; The adjusted contrast image of (a) is shown in (b). The low intensity parts then are present in (b), consisting of the $-1st$ images of the FZP array as the one delimited by the incomplete black circle and the $1st$ order image from the main FZP indicated by the red arrows.

Figure 6.10 (a) is the raw image directly from the experimental set-up. At first sight, we can see both the $0th$ order image and the first order image formed by each FZP in the array, delimited by the yellow and red dashed circles in the inset, respectively. In additional, as pointed out by the white arrow, there is a dark dot in the center of each $1st$ image, which is the shadow of its center stop. Adjusting the contrast of figure 6.10 (a), the low intensity components in the raw image become visible, as shown in figure 6.10 (b). The partially drawn black circle indicates a $-1st$ order image formed by one of the FZPs in the array, which can be barely seen in the raw image. And the red arrows point to the $1st$ image from the main FZP in the background. Due to the structure of the beamshaper and its center stop, no direct beam passes through the main FZP, hence the $0th$ image of the main FZP is not present in the raw image. Among the different

components of the raw image, only the $1st$ order images of the FZP array are assigned for use as the light field data.

Looking closely at the image of the FZP array, we can note that the $0th$ order and the $1st$ order images from the sub-FZPs of the array are not concentric. To make the difference of the image center between these two orders more obvious, we enlarge the image of the FZP array in figure 6.11 and mark the image center of the $0th$ order and the $1st$ order by red dot and black cross, respectively. The image centers are detected by numerical image processing, which is detailed in the section 6.2.4.2.

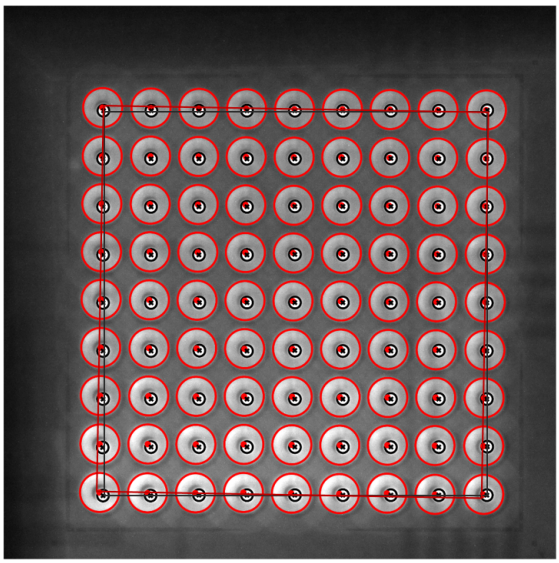

Figure 6.11: Rotation error between the FZP array and its center stop array in the experimental set-up: The centers of the $0th$ order and the $1st$ order images of each FZP are marked by the red dots and black cross. The red and black squares, which connect the centers of the $0th$ order and the $1st$ order outermost images, imply the positions of the center stop array and the FZP array, respectively.

The difference of the image center between the two orders is originated from the rotation error between the FZP array and its center stop array in the experimental set-up, as shown by the two squares in figure 6.11. The red and black squares are drawn by connecting the centers of the $0th$ order and the $1st$ order outermost images, respectively. Due to the imaging mechanism of the FZP, the center of the $1st$ order image is always

located on the optical axis of the FZP, while that of the $0th$ order is determined by its center stop (see figure 6.12). Accordingly, the red and the black squares imply the positions of the center stop array and the FZP array, respectively. The difference in position of these two squares visualizes the rotation error between the FZP array and its center stop array. Although the rotation error propagates to every stitching image, it has no significant effect on the light field data that employs only the $1st$ order image of the FZP array.

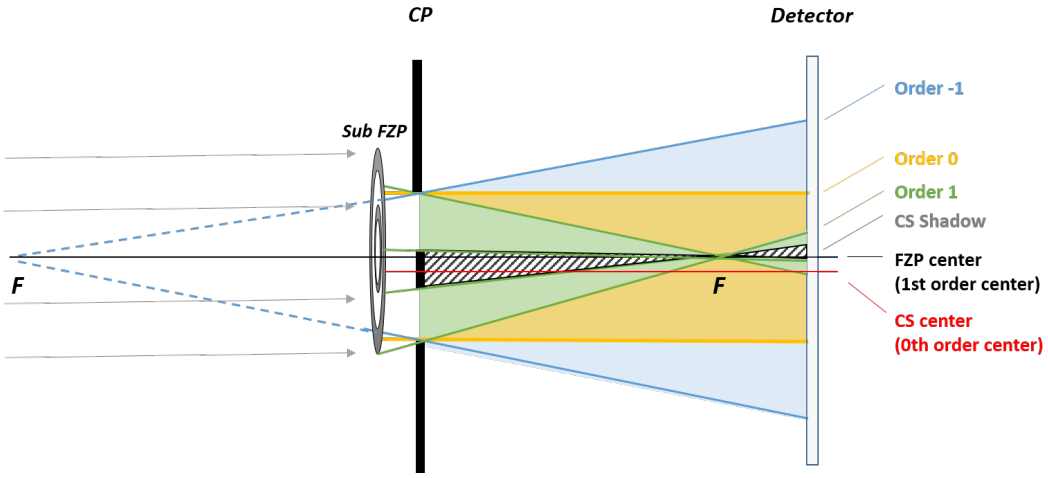

Figure 6.12: Optical path diagram of raw image: The incident beam on the sub-FZP is considered as parallel beam. The center axes of the sub-FZP and its center stop, shown by the black and the red solid lines, are not aligned due to the rotation error. Accordingly, the center of the $1st$ order image positioned on the sub-FZP optical axis is shifted from the center of the $0th$ order image determined by the center stop. The blue, yellow, green and slash shaded parts are the negative $1st$ order, the $0th$ order, the $1st$ order images and the shadow of the center stop.

Since the distance between the main FZP and the FZP array is vastly different from their size, the incident beam on the FZP array has extremely low angular divergence, thus it can be approximated as parallel beam. Under this approximation, the formation of each part of the micro-image from the experimental FZP array with slightly rotated center stop array is further illustrated in the optical path diagram of a single sub-FZP 6.12. The central axes of the sub-FZP and its center stop are shown by the black

and red solid lines, respectively. As the $0th$ order image on the detector is the direct beam that is not blocked by the center stop, its center is determined by the center stop and shifted accordingly.

6.2.4 Image pre-processing

From the previous analysis in the section 6.2.3, we can see that the micro-image from the experimental X-ray plenoptic camera has more complex structure than that from the visible light plenoptic camera. The goal of image pre-processing is to extract the light field image from the experimental data. In our experiment, only the $1st$ order image of each sub-FZP in the array is assigned to be used as the light field data. To adapt the stitching acquisition, the pre-processing is performed in each stitching position, which consists the selection, the localization and the enhancement of the $1st$ order sub-image. The output of each position is then synthesized into a single light field image. More details about the pre-processing will be discussed in the following.

6.2.4.1 Selection of the first order sub-image

In order to select the $1st$ order images from the raw images, we can take advantage of the significant difference in intensity between different orders. The straightforward way is setting an appropriate threshold value on the raw image that corresponds to the $1st$ order image. However, the illumination in the experiment is remarkably uneven, which will introduce errors in image selection. Figure 6.13(a) and (b) display an example flat-field image and the threshold result without illumination correction. The selection is performed on the flat-field images (the image without sample) to avoid the interference from the intensity variance caused by the sample. We can observe the fact that the size of the $1st$ order images of the FZP array are almost the same in the flat-field image. The red circles of the same size have been drawn for the convenience of comparison. With respect to this fact, the errors due to the non-uniform illumination can be seen by the change in size of the selected area from the brighter to the darker illumination part, i.e. from the bottom to the top in the figure 6.13(b). The change in

size can be quantified by the standard deviation (SD) of the selected area surface in pixel. The SD of the the result without non-uniform illumination correction is 90 pixels.

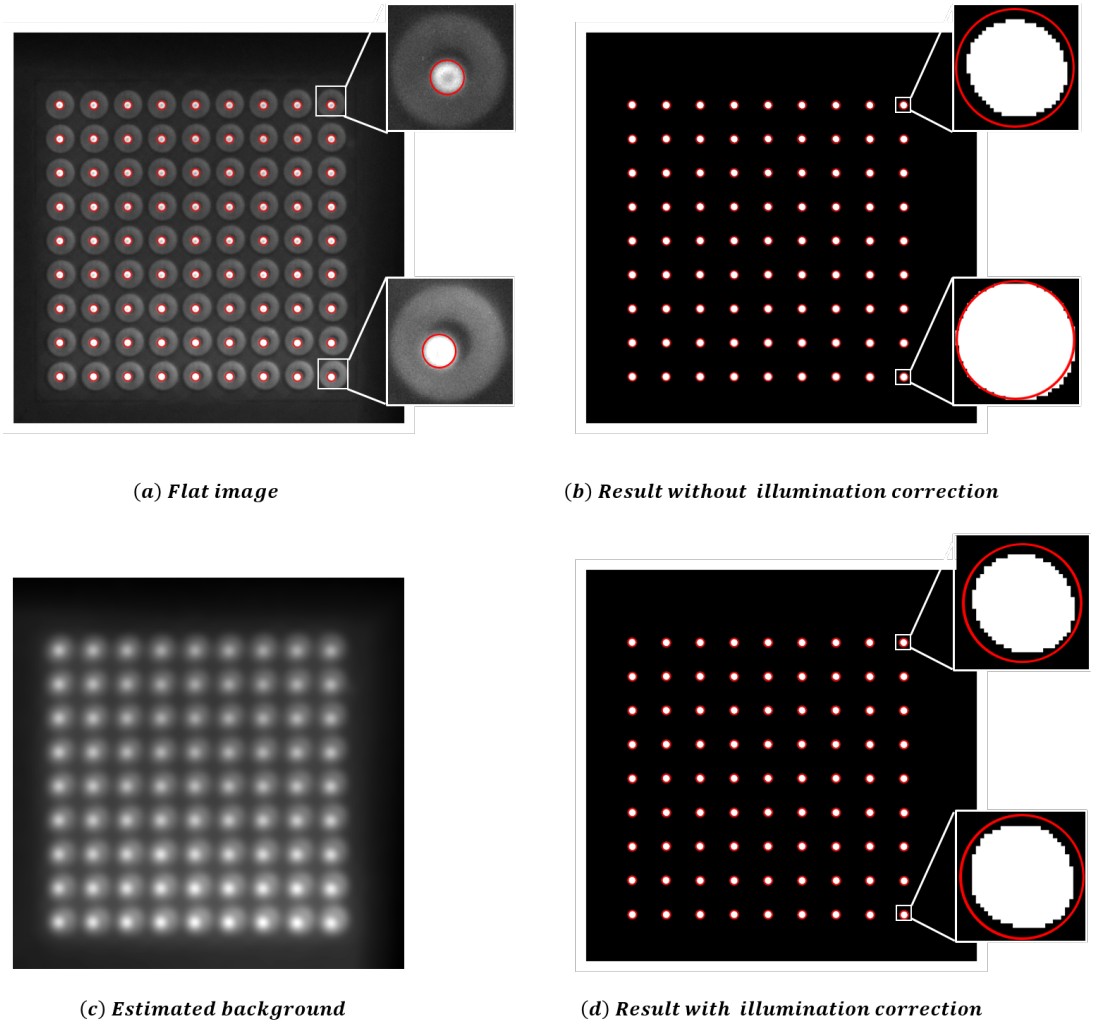

(a) *Flat image*

(b) *Result without illumination correction*

(c) *Estimated background*

(d) *Result with illumination correction*

Figure 6.13: Selection of the first order image with non-uniform illumination correction: (a) An example of flat image on which the selection is performed. (b) The result of threshold selection from the flat image without correction. The selected areas change from the brighter part to the darker part, implying the error introduced by the non-uniform illumination. (c) Background estimated by low frequency component of the flat image. The estimated background is generated by applying a Gaussian blur filter with a large kernel. (d) The result of threshold selection from the flat image with correction. The influence from the non-uniform illumination has been reduced, and the selected areas tend to be the same. All the red circles in the figure have the same size to facilitate size comparison.

The non-uniform illumination can be corrected in several ways based on the removal of background [112]. A common method to estimate the background is applying a low-pass filtering with a very large kernel on the image. We adopted a Gaussian blur filter as the low-pass filter to generate the estimated background in figure 6.13(c). Dividing the flat-field image by the estimated background, we obtained the corrected image. Figure 6.13(d) displays the threshold result from the corrected image, in which selected areas from the bottom to the top tend to be the same. The SD in surface of the result with non-uniform illumination correction is significantly reduced to 20 pixels.

6.2.4.2 Localization of the first order sub-image

The post image processing of the light field image greatly relies on the positions of sub-images. Thus the localization of each $1st$ order image is a crucial step. In order to reduce the disturbance of other structures in the composite image, the localization of the $1st$ order images is performed on the thresholded binary result from the flat image. As the circular $1st$ order images approximately have the same size that can be easily measured, the localization is actually detecting the center of the circle with known radius. It is a classical issue in image processing and many algorithms have been developed as reviewed in the section 3.1. We test four of these different algorithms on the experimental image and discuss about their performance in the following.
The four different algorithms of center detection that will be discussed are Hough transform, intensity transform, distance transform and image moment [113] [114] [115] [116]. Brief descriptions of the basic principles of each algorithm are given below:

- **Hough Transform**

The use of the Hough transform to detect the center of a circle with known radius r can be summarized as a voting procedure. As illustrated in figure 6.14, the operation is to transform each point on the edge of the input circle into a circle of radius r centered at that point. Theoretically, all such circles will have a common intersection corresponding to the center of a perfect circle. In practice, the most voted point, at which the most

of circles cross, is considered as the center of the input circle that may not be a perfect circle.

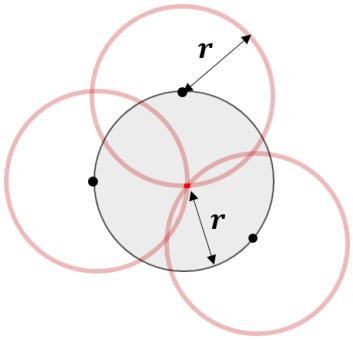

Figure 6.14: Basic principle of Hough transform. The red circles centered at different black edge spots with the radius of the detected circle intersect at a common point, which is the center of the detected circle.

- **Distance Transform**

Distance transform is usually operated on binary image. The general idea of the distance transform is to generate a distance map that labels each pixel of the image with the distance to the nearest zero-value pixel. As shown in figure 6.15, the center of a circle will have the longest distance to the boundary zero-value pixel, namely the highest value in the distance map. The center of an input circle thus can be derived from the maximum value pixel after the distance transform.

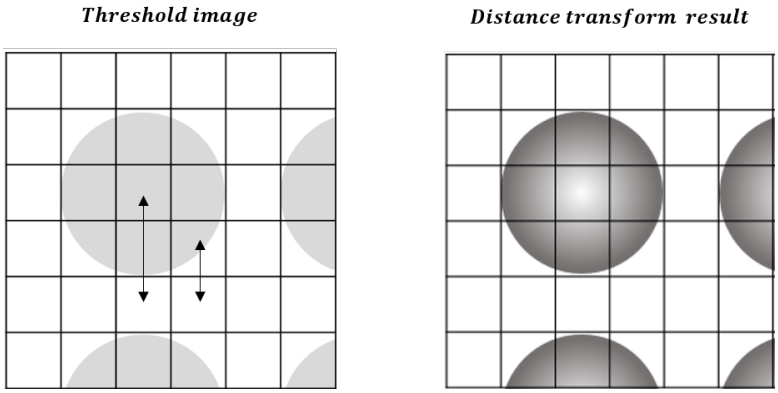

Figure 6.15: Basic principle of distance transform. The value of each pixel is replaced by the distance to the nearest zero-value pixel. The center of circle corresponds to the pixel with the longest distance.

- **Intensity Transform**

Similar to the distance transform, the concept of the intensity transform is replacing each pixel of the image by the intensity of its neighbour pixels. The intensity transform can be considered as convolving a predefined spatial filter on the image. In our case that the data from the plenoptic camera is an array of adjacent sub-images, we define a binary convolution kernel of the sub-image size (the diameter for the circular sub-image), and only its borders have the value of 1 (see figure 6.16). Mapping this convolution kernel on the input image, each pixel is converted to the intensity sum of all pixels at a distance r from it. Only the borders of the center (the red square in figure 6.16) will cover all the gap pixels with low intensity and thus turns into a local minimum, by which we can find the center of the circle.

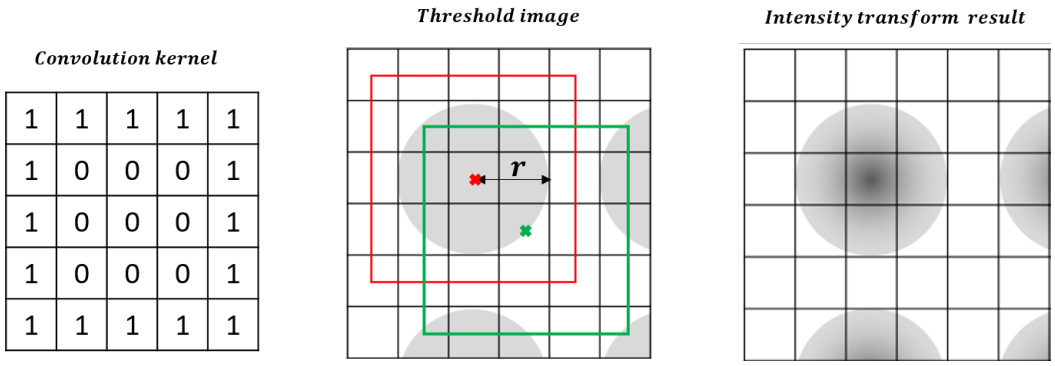

Figure 6.16: Basic principle of intensity transform. Due to the adjacency of plenoptic image, only the edge pixels of the center will pass through all the the gap pixels with low intensity , as the red square. Therefore, the local minimum after intensity transform corresponds to the center.

- **Image Moment**

Image moment is a technique widely used in imaging processing to determining the centroid of an arbitrarily shaped object, mathematically defined as

$$M_{ij} = \sum_i \sum_j x^i y^j I(x, y) \tag{6.1}$$

where M_{ij} is the $(i+j)th$ order image moment, (x, y) is the pixel coordinates and $I(x, y)$ is the intensity of pixel (x, y).

From a statistical perspective, the centroid of an object is the arithmetic mean position $(\bar{x}, \bar{y})$ of all its constituent points. It can be calculated from the weighted average of the image pixels' intensities, expressed in the integral form in equation 6.2.

$$\int x \, dI = \bar{x} \int dI, \ \int y \, dI = \bar{y} \int dI \tag{6.2}$$

The discrete form of the left side of the above equation corresponds exactly to the $1st$ order image moment (M_{10} for x direction and M_{01} for y direction), and the right side $\int dI$ is the $0th$ order image moment M_{00}. Thereby, the centroid of object can be given by the image moment as

$$(\bar{x}, \bar{y}) = (\frac{M_{10}}{M_{00}}, \frac{M_{01}}{M_{00}}) \tag{6.3}$$

Considering that our experimental data is in the form of image array, it is necessary to split the experimental image into fragments containing only one sub-image each before applying the image moment to detect the center grid.

We applied these four methods on the threshold binary results from the experimental images. To compare their performance in a general way, we recreated the binary images of circles array according to the center grid detected from these four methods. The subtraction between these output images and the initial threshold image are displayed in figure 6.17. The red and blue areas represent the uncovered and exceeded parts with regard to the initial threshold image, respectively. The standard deviation of difference per sub-image in pixel is given in table 6.3.

Hough transform	**Intensity transform**	**Image moment**	**Distance transform**
149	97	79	68

Table 6.3: Standard deviation of the results of different methods per sub-image in pixel.

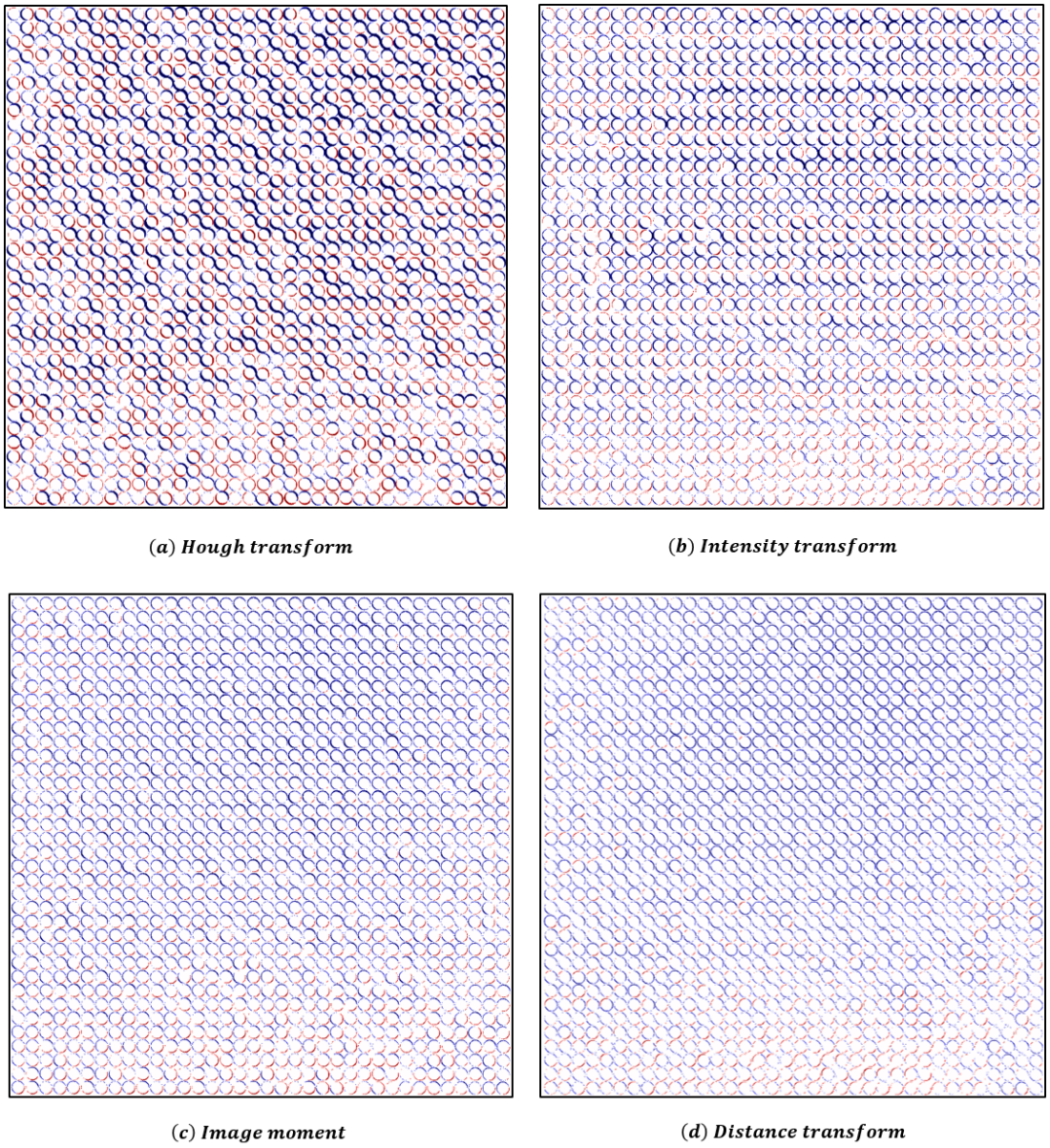

(*a*) ***Hough transform*** (*b*) ***Intensity transform***

(*c*) ***Image moment*** (*d*) ***Distance transform***

Figure 6.17: Subtraction between the detected threshold result image and the estimated binary image according to the detection results of different methods. The white area represents that the detection result is consistent with the input image. And the red and blue areas are the uncovered and exceeded parts with regard to the initial threshold image, respectively.

Apparently, the result of Hough transform has relatively large bias, due to the fact that the sub-images are not perfect circles. The result of intensity transform has a clear improvement but not as good as the results of image moment and distance transform. Because the intensity transform detects the image with a fixed size kernel, while the position distribution of the sub-images is not uniform. The results of image moment and distance transform are similar. However, to detect an array-like image, the image moment method requires pre-splitting of the image, as mentioned above. Image moment method is relatively inconvenient to plenoptic camera data, especially for the plenoptic image with the sub-images of non-uniform position distribution. In summary, distance transform is a more compatible method to the plenoptic image for center detection. It is more tolerant to the irregularity in shape and in position of sub-images, leading to less bias. Furthermore, the application of distance transform is more handy without additional pre-processing.

6.2.4.3 Sub-image enhancement and light field image extraction

The imaging processing steps described above preformed on the flat-field images allow to generate the selection mask for the $1st$ order image. The reader may notice that the $1st$ order images of the FZP array cannot be directly seen from the raw images displayed before. This is because the contrast of the experimental $1st$ order image is extremely low in raw images and submerged by the intense background, poorer than what would be expected by referring to the simulation results at the experimental energy in Chapter 4. Besides the interference between different orders images, the extremely low contrast is probably due to the fact that the test patterns are not sufficiently opaque to the X-rays at the experimental energy.

In order to enhance the visibility of the image and increase the signal-to-noise ratio (SNR), before applying the selection mask in each stitching position, we average the raw image and correct it by the division with the averaged flat-field image. The output image of one single stitching position is shown in figure 6.18. The pipeline of image processing for each stitching position is summarized in figure 6.19.

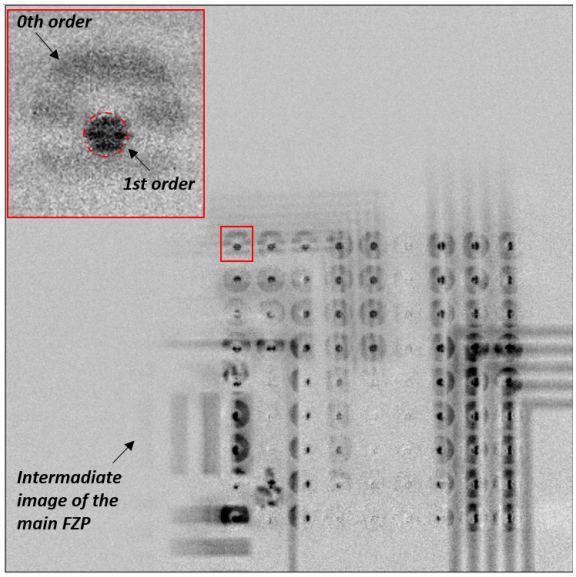

Figure 6.18: Enhancement of the 1*st* order sub-image. The enhanced image is the result of division between the averaged raw image and the averaged flat-field image. The fine structure of a single sub-image is zoomed in the left-upper inset.

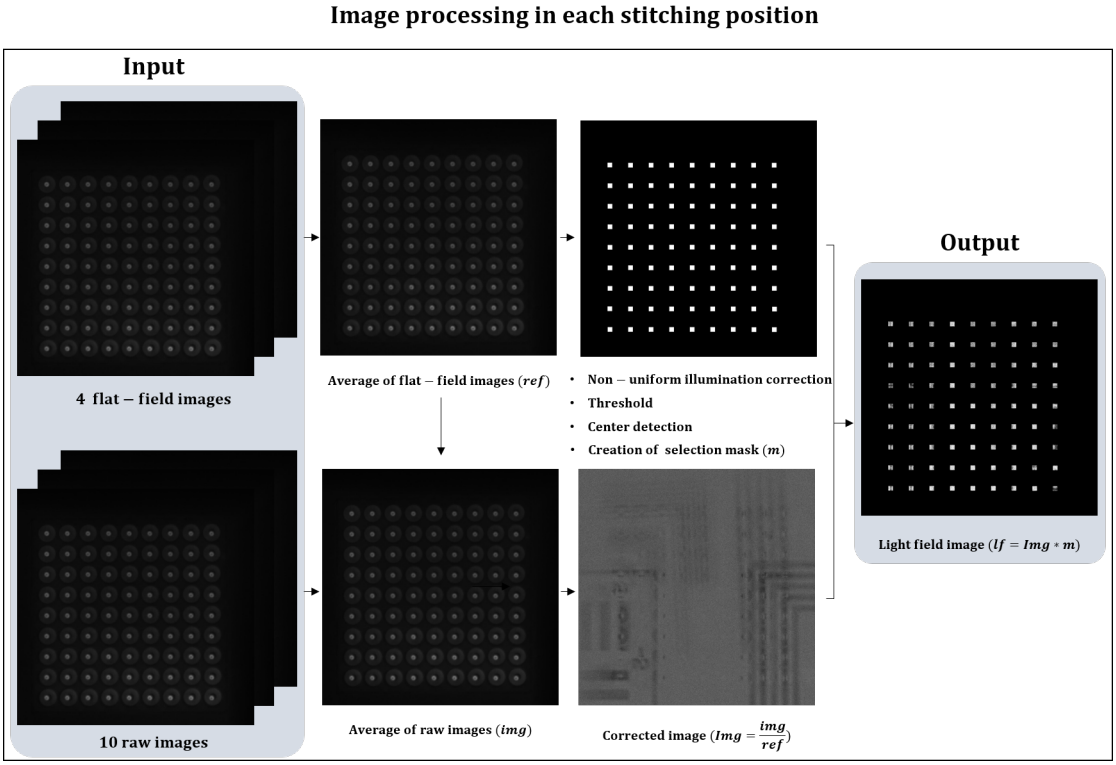

Figure 6.19: Pipeline of image processing in each stitching position

Combining the outputs of 16 stitching positions and removing blank pixels, the extracted light field image consisting of 36×36 sub-images is displayed in figure 6.20. Compared to the under-sampling light field image taken with 9×9 FZP array in figure 6.7(b), each part of the targets has been imaged by at least one sub-FZP in the synthesized light field image extracted from the stitching data.

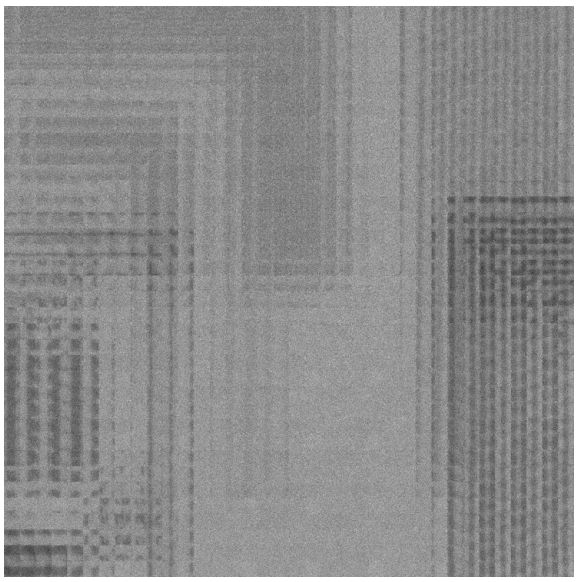

Figure 6.20: Light field image extracted from a complete experimental dataset of 16 stitching positions, consisting of 36×36 sub-images. Each sub-image contains 27×27 pixels. The used dataset was acquired with T1 approximately in focus.

6.2.5 Results and analysis

6.2.5.1 Parameters estimation of experimental plenoptic camera

According to the measured distances and the acquired images in the experiment, we theoretically extrapolated the basic parameters of the experimental X-ray plenoptic camera before reconstruction. A note of caution is due here since there exists errors in the measured experimental distances. The size of the optics used is in micrometers, while the distances between them can go to the order of meters. Moreover, with the obstruction of the mounts of each optics, the accuracy of the measurement was quite limited under the current experimental conditions. To reduce the effect of measurement

errors, we first estimated more finely the geometry of the experimental set-up from the magnification of the acquired images.

From the center spacing in pixels of the $1st$ order images extracted from the raw images (distance between two red circles in figure 6.11) and the known spacing of the FZP array, the estimated effective pixel size of the experimental detector system d_p is 0.89 μm. A bar of the nested L-shaped pattern with original width 1 μm on the right of $T1$ occupies 9 pixels on average in the sub-image. Multiplied by the effective pixel size, the width of the bar in the sub-image is 8 μm, implying a magnification M of about 8 through the assembly of the main FZP and the FZP array. On the other hand, the distance from the FZP array to the detector b, which can be derived from the size ratio between the $1st$ order image and the sub-FZP, is approximately 111.8 mm. Furthermore, the magnification of the main FZP M_1 is about 29, measured from the conventional image with $T1$ in focus in figure 6.4(b). Combining the above calculation results, the intermediate image of $T1$ formed by the main FZP is located at about 410 mm upstream of the FZP array. Thus, the magnification of the sub-FZP M_2 is 0.275. Taking the distance between the main FZP and the FZP array z_0 measured in the experiment and the above estimated position of the intermediate image, we can derive the sample position Z is 129 mm, which basically agrees to the measured value with a ± 0.5 mm error. The following analyses are based on this experiment geometry set out in the table 6.4, but the error still exists.

Z	z_0	b	M_1	M_2	M	d_p
129 mm	3759 mm	111.8 mm	29	0.275	8	0.89 μm

Table 6.4: Experimental geometry parameters optimized based on practical measurements and acquired images.

Further calculations are performed under the assumption that the image plane of $T1$ after the FZP array lies exactly in the plane of the detector. However, the extremely small numerical aperture of the sub-FZP results in a very long depth of field, and the exact position of the image plane is difficult to determine accurately in practice.

Based on the geometry and the optical components of the experimental set-up, we calculate the basic parameters describing its imaging performance without post numerical processing. The definitions and equations applied in this calculation are explained in detail in Appendix 7.A.

The numerical aperture and the corresponding lateral resolution in the intermediate image plane of the main FZP and the sub-FZP, respectively noted as NA'_M, NA_m, Res'_M and Res_m, are provided in the table 6.5. And the resolution of the detector Res'_d the intermediate image plane is given by dividing the effective pixel size by the magnification of the sub-FZP, i.e. $\frac{d_p}{M_2}$. Different from most cases of visible light plenoptic camera, the lateral resolution of the experimental set-up is more limited by the main FZP than the FZP array and is ultimately determined by the resolution of the detector.

NA'_1	NA_2	Res'_M	Res_m	Res'_d
4.2×10^{-5}	1.2×10^{-4}	1.64 μm	0.57 μm	3.32 μm

Table 6.5: Numerical aperture and lateral resolution of the optical elements of the experimental plenoptic camera in the intermediate image plane.

With the above analysis, the basic parameters describing the performance of the experimental plenoptic camera in the object plane , such as numerical aperture NA, resolution Res, field of view FoV and depth of field DoF, are summarized in the table 6.6.

NA	Res	FoV	DoF
1.1×10^{-3}	0.11 μm	35 μm	0.1 mm

Table 6.6: Basic parameters of the experimental plenoptic camera in the object space.

6.2.5.2 Refocusing results

We reconstruct the extracted light field image in figure 6.20 with the back propagation algorithm based on ray tracing discussed in the section 3.2. Images reconstructed at different distances have been examined, while sharp images can be only obtained with

$Z_r = 129 \pm 0.5\ mm$ around the object plane of $T1$, consistent with the experimental object distance. The refocusing results are partially displayed in figure 6.21 with the equivalent distance to the main FZP in object space Z_r. The reconstruction distance Z_r is calculated from the estimated geometry and thus also contains errors. For comparison purpose, each reconstructed image is resized to the same dimension, i.e. 324×324 pixels.

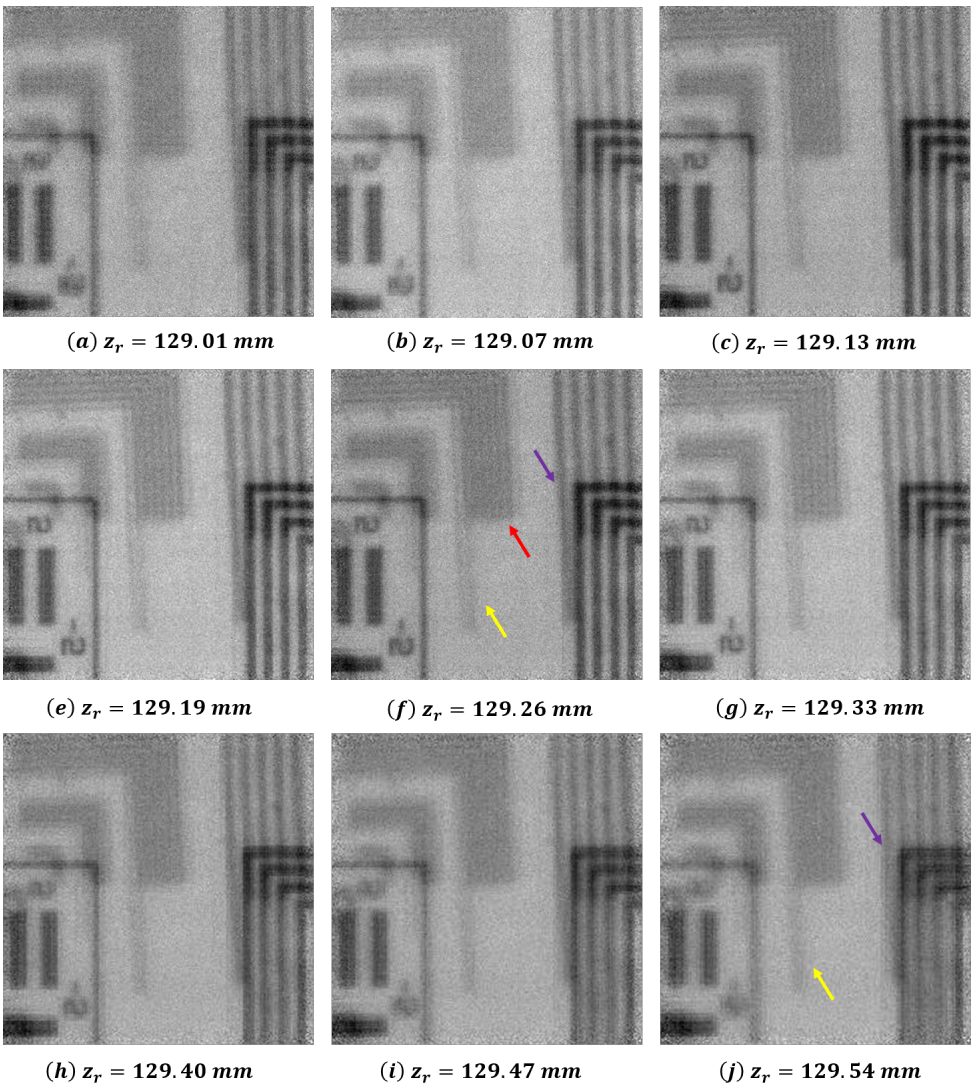

Figure 6.21: Partial refocusing results: this set of images are reconstructed from the raw images acquired near the image plane of $T1$. The Z_r labelled below each image indicates the equivalent object plane after reconstruction. For $T2$, the sharpest images of the lines indicated by the purple and the yellow arrows are obtain with different Z_r. The set of thin lines of $T2$ pointed out by the red arrow is more the result of aliasing than refocusing.

The change of focus can be seen from the sharpness evolution of the test patterns in the set of reconstructed images. A qualitative examination of figure 6.21 from (c) to (g) shows that the quality of reconstructed images remains approximately consistent over a distance range of about 0.2 mm. Comparing this distance range with the DoF of the experimental set-up (about 0.1 mm, see table 6.6), we can notice the depth of field of the system has been extended by the post numerical processing, which is a characteristic of plenoptic camera. The quantitative analysis of the reconstruction results from the light field image shown in figure 6.20 are provided in the following sections 6.2.5.3 and section 6.2.5.4.

Closer inspection of the refocusing results of $T2$ shows that the group of the 1 μm wide pattern indicated by the purple arrow in the reconstructed images are sharp in the range $Z_r = 129.13\ mm$ to $Z_r = 129.33\ mm$, whereas the single vertical line of the 0.5 μm wide group indicated by the yellow arrow is doubled like in its out-of-focus image (see figure 6.4(b)). Special attention needs to be paid to interpret the sharpness evolution of the 0.5 μm wide pattern group of $T2$. Although the set of fine lines indicated by the red arrow appear from the image reconstructed at $Z_r = 129.13\ mm$, it is actually more a result of aliasing than refocusing. On $T2$ in figure 6.4, the 0.5 μm wide pattern group originally consists of 7 lines, but only 6 lines can be seen in reconstructed image. Therefore, the single vertical line of the 0.5 μm wide reflects better refocus level of $T2$. The middle vertical line starts to focus when the reconstruction distance Z_r increases to 129.54 mm. However, no clear images refocused separately on $T1$ and $T2$ have been found via the post numerical processing. The explanation for this is that $T2$ was out of the depth of field (DoF) of the experimental set-up. Blocked by the mounts, the minimum achievable distance between the two targets is approximately 1.3 mm, which far exceeds the DoF of the experimental set-up about 0.1 mm in object space, greatly limiting the image quality of $T2$ in the reconstruction results.

The above interpretations about the refocusing of $T2$ are confirmed by comparing the sharpest refocused images reconstructed from three light field images acquired with the targets at different object distances (see figure 6.22). The targets positions of these

three light field images are illustrated by the schematic at the bottom of figure 6.22. The targets position of the light field image used in figure 6.21 is represented by the green rectangle in the schematic, where $T1$ is in the focal plane of the experimental set-up and about 129 mm away from the main FZP. Keeping the distance between $T1$ and $T2$ constant, the targets of the other two light field images, represented by the blue and yellow rectangles, were moved closer to the main FZP 0.5 mm and 1 mm, respectively. In other words, $T1$ is moved away from the focal plane, while $T2$ is moved closer to the focal plane. The refocused images corresponding to the three targets positions are enclosed by the same color. No matter which target, a significant improvement in its refocused image can be seen when the target gets closer to the focal plane in the acquired light field image.

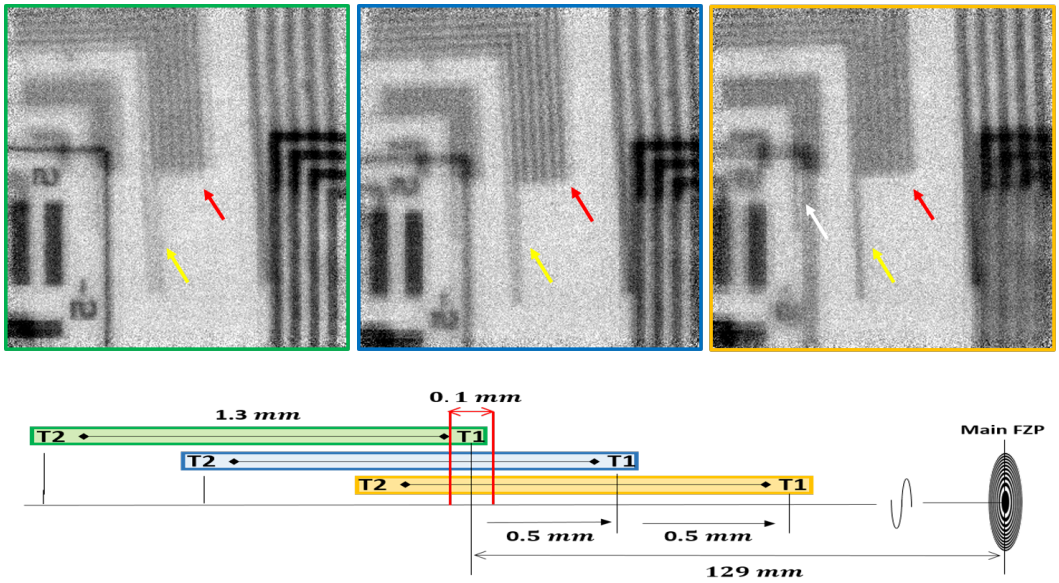

Figure 6.22: Refocusing results reconstructed from the light field images acquired with the targets at different positions: The position change of the targets are shown in the schematic at the bottom of the figure. The corresponding refocused images to different targets position are enclosed in the same color. From left to right, $T1$ is moving away from the focal plane, while $T2$ is getting closer to the focal plane. The region enclosed by the red lines is the depth of field of the experimental set-up without the post numerical processing.

Examining $T2$ in three refocused image from left to right, we can remark that the vertical single line indicated by the yellow arrow becomes progressively refocused as $T2$

approaches the focal plane. Even a thin line of 250 μm width on $T2$ indicated by the white arrow becomes well visible in the right refocused image, where $T2$ is closest to the focal plane. However, the finer lines indicated by the red arrow are more visible in the middle refocused image than in the right one, contrary to the change in the relative position of $T2$ to the focal plane. This is consistent with our previous observation that the vertical single line reflects the real focus level of $T2$ rather than the finer lines indicated by the red arrow.

6.2.5.3 Resolution analysis of reconstructed images

The reconstructed images contain significant noise from its origin light field image. The noise has an important negative impact on the contrast and sharpness of the image and poses difficulties for accurate measurement of standard parameters of image quality. Here, we measure the width of point spread function (PSF) to reflect the resolution of the reconstructed image. This resolution measurement is established based on the theory that an image is the convolution result between the PSF of the imaging system and the perfect object image predicted by geometrical optic, as discussed in the section 4.4. A major advantage of this method is that it exploits not only the intensity information of the image but also the overall shape of intensity profile plot, providing a better accuracy. Since the size of test pattern is known, the most straightforward method to measure the PSF from the image would be the inverse process of convolution, namely, deconvolving the image by the magnified test pattern. However, deconvolution is highly sensible to noise, and even tiny noise can significantly degrade the result. Thus deconvolution is not applicable to our case. Therefore, instead of direct deconvolution, we convolve the test pattern with hypothetical PSF of different widths and compare the results to the profile plot of the image, and finally determine the actual PSF by least-squares method. This PSF measurement method is actually curve fitting, as illustrated in figure 6.23 (b). In practice, we construct the fitting function F by convolving a window function T of the target bar width with a Gaussian function $G(\sigma)$ approximating PSF. Due to

the significant impact of noise, we additionally introduce a scale factor α and a noise term β to correct the fitting function, yielding

$$F(\sigma, \alpha, \beta) = \alpha * (T \otimes G(\sigma)) + \beta \tag{6.4}$$

The best fitted parameters are that minimize the least-squares between the fitting function F and the image profile plot I, mathematically written as

$$\{\sigma^*, \alpha^*, \beta^*\} = argmin \, \|I - F\|^2 \tag{6.5}$$

We use the full width at half maximum (FWHM) of the best-fitted Gaussian function as the reconstructed image resolution, which is approximately 2.355 times σ^*. Caution must be applied when comparing different resolution values, because they are defined inconsistently. With this resolution measurement method, we investigated the resolution across the refocused image and along the reconstruction distance in the experimental reconstructed images.

We first measured different sections of $T1$ in its refocused image. As examples, figure 6.23(c) and (d) display the measurements of the two groups with known widths of 1 μm and 1.8 μm, respectively indicated by the yellow and red squares in (a). For each bar of interest, the measurement was performed on the average normalized profile of multiple rows extracted from the inverted refocused image of $T1$. Inverting image is for the convenience of the subsequent fitting. The results vary from 0.38 μm to 0.66 μm, showing that the resolution is not consistent across the same reconstructed image. This fact can also be observed directly from the change in the shape of each bar profile, as shown in figure 6.23(d). The higher the resolution is, the more the profile of a bar tends to be rectangular.

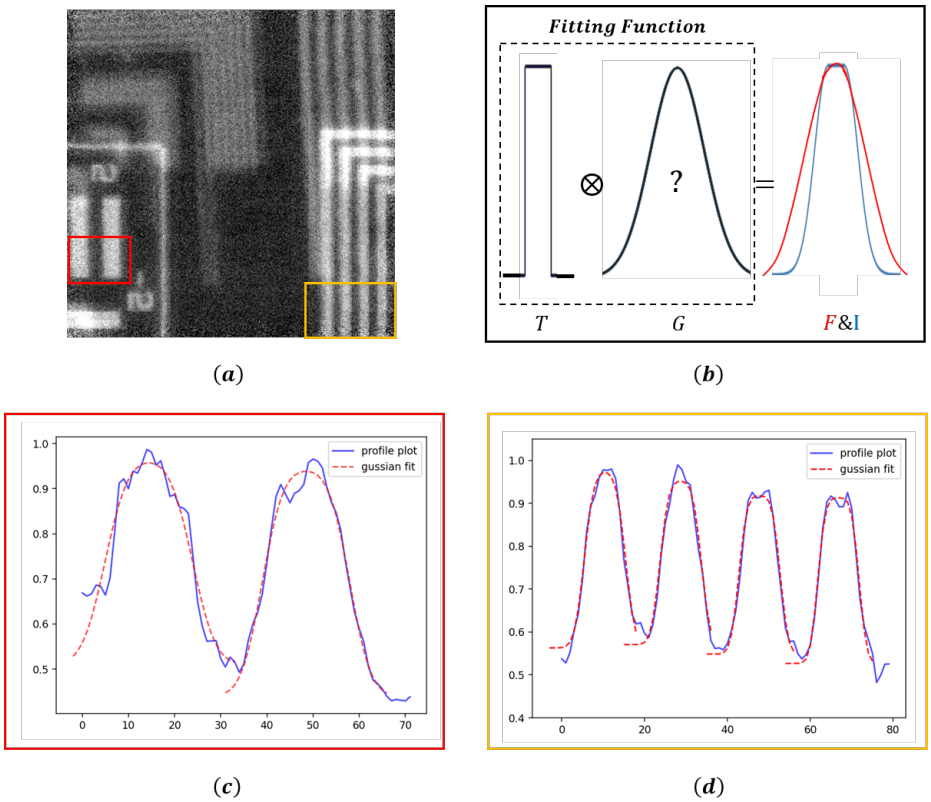

(*a*) (*b*) (*c*) (*d*)

Figure 6.23: Resolution measurement in reconstructed images: (a) indicates the measured sections of two groups bar with widths of 1 μm and 1.8 μm, respectively indicated by the yellow and red squares. The corresponding profiles and fitting plots are displayed in (c) and (d). (b) illustrates the main idea of resolution measurement method used. The image of a bar is considered as the convolution result between a window function T and a Gaussian function G. The resolution is defined as the FWHM of G that minimizes the least-squares between the fitting function F and the image profile I.

The resolution along reconstruction distance Z_r has been studied from two aspects: On one hand, the resolution measurements were performed in the experimental images reconstructed more precisely by a weighted ray-tracing algorithm [117]. On the other hand, the resolution was measured in the numerical images reconstructed from the light field image, which was simulated with the same geometry as the experiment by the algorithm described in [118]. The simulation work was performed by Dr. Charlotte Herzog.

A few of reconstructed images and simulation images used in this study are displayed

in figure 6.24. In this section of investigation, the resolution of the 1 μm wide bar on $T1$, indicated by the red arrow in figure 6.24, is used to represent the resolution of the reconstructed image.

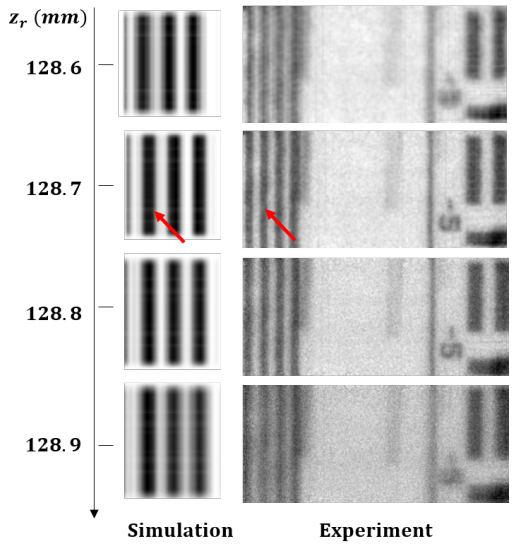

Figure 6.24: Simulation and experimental images: The left and right columns display the images at different Z_r reconstructed from experimental and simulation data, which are used in the study of resolution along distance.

The blue and red plots in the figure 6.25 show the resolution along the reconstructed distance Z_r measured from experiment and simulation, respectively. Compared to the experimental results, the resolution of the simulation is better (lower value), since it does not contain noise. The evolution of resolution along Z_r in the simulation and the experiment agrees well. The best resolution is achieved at the reconstruction distance around 128.7 mm in both the simulation and the experiment. The difference in the reconstruction distance Z_r with the previous sections arises from the uncertainty in the estimation of the experimental set-up geometry. More importantly, the resolution plot along the reconstruction distance reveals the focusing changing ability of the experimental X-ray plenoptic camera.

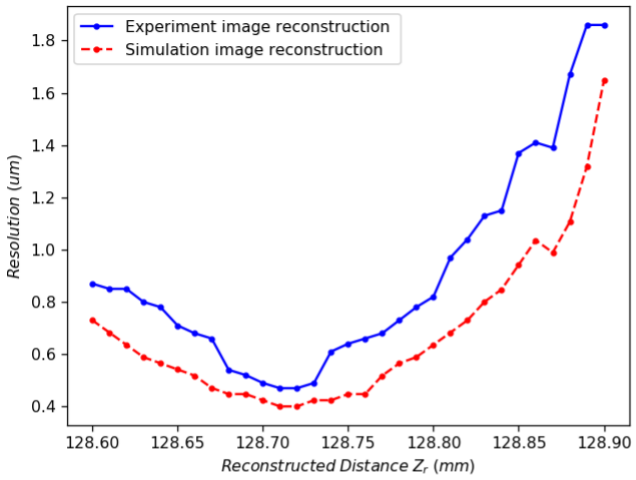

Figure 6.25: Resolution along reconstruction distance: The resolution of the 1 μm wide bars of T1 measured from the simulation and the experimental reconstructed images are plotted respectively in red and in blue along reconstruction distance. The difference in the reconstruction distance Z_r with the previous sections arises from the uncertainty in the distance estimation of the experimental set-up.

Furthermore, the highest resolution around the target plane in images reconstructed from either experimental or simulated data is 4 or 5 larger than the estimated resolution in the sub-image plane given in the table 6.2.5.2. This may be explained by the relationship between the pixel and the aperture of the ML discussed in the section 3.2.3. From the experimental data, the targets can be well reconstructed with the 8 pixel patches of the 31 pixel sub-images, which corresponds to the $\frac{8}{31}$ numerical aperture of the main FZP. As the lateral resolution is inversely proportional to the numerical aperture, it results in a 3.8 times enlargement of the sub-image resolution in the reconstructed images. In addition, for the convenience of the numerical processing, the 31 pixel is actually the width of the inner tangent square of the circular sub-image. The reconstruction numerical aperture of the targets is thus slightly smaller than $\frac{8}{31}$. Consequently, the reconstruction resolution is slightly larger than 3.8 times the sub-image resolution, which is close to the resolution ratio 4 measured from the images reconstructed from the simulation data. The significant noise in the experimental data might further enlarge this factor to 5.

6.2.5.4 Depth estimation in reconstructed images

In order to extract the depth, we applied the two approaches introduced in the previous section 3.3 on the experimental light field data, namely the focal stack-based approach and the EPI-based approach.

Reviewing our studies about the resolution, the analyses are performed on the focal stack reconstructed from the experimental data. The focal stack-based approach, of which the main idea is using the best refocused image to find the object position, is equivalent to the study of the resolution along reconstruction distance effectuated above. The extracted depth for $T1$ is about $128.7mm$. For $T2$, the single vertical line in the middle of the reconstructed image suffers from the significant noise, therefore we can barely extract a minimum value from its resolution plot along the reconstruction distance to find its corresponding depth.

For the application of the EPI-based approach, we regrouped the experimental light field image to multi-perspective image, shown in figure 6.26 (a). However, due to the limited number of sub-FZP in the experimental set-up and the significant noise, the image of each sub-view can be barely seen, as zoomed in the red inset of figure 6.26 (a). Recall that the EPI-based approach estimates the depth based on the disparity between the image of different sub-views, which also exits between different sub-images in light field image, as illustrated in the section 3.2. In contrast to the light field data acquired by visible light plenoptic camera, the experimental data contains much fewer sub-images, but the size of the sub-image is large. Hence, in our case, the disparity is easier to be measured directly from the light field image than from the multi-perspective image.

An example of the disparity measurement is shown in the inset of figure 6.26 (b), where the blue square delineates each sub-image, the red spot represents its center and the dashed black lines indicate the same section of a 1.8 μm wide bar edge in $T1$. The average disparity of $T1$ measured from the experimental light field image is 7 ± 1 pixels. Because of the stitching acquisition, the baseline of the experimental set-up is reduced to 27.5 μm. According to the equation 3.4 and the lens imaging

equation, the corresponding depth in object space is $129.1 \pm 0.1\ mm$, consistent well with the distance measured in the experiment. The depths estimated by the focal stack-based approach and the EPI-based approach, respectively 128.7 mm and 129.1 mm, are slightly different, owing to the incertitude in the geometry of the experimental set-up. Their difference 0.4 mm is lower than the experimental precision of the distance measurement. However, $T2$ is out of focus in the detector plane, making it nearly impossible to find a sharp edge in the sub-images to measure the disparity.

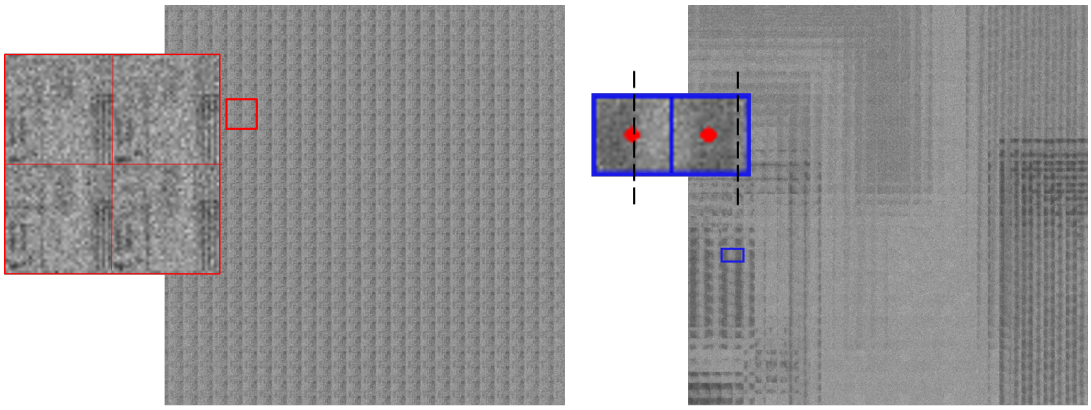

(***a***) (***b***)

Figure 6.26: Application of the EPI-based approach in the experimental light field data: (a) The multi-perspective image regrouped from the experimental data for the application of the EPI-based approach. Due to the small number of sub-FZPs and the significant noise, the quality of each sub-view image is greatly limited and the disparity can barely extracted. (b) An example of disparity measurement alternatively performed in the experimental light field image. The dashed black lines indicate the same section of a bar edge of $T1$. The disparity can be measured from its relative displacement with respect to the center of sub-image marked by the red spot. The blue square delineates the edge of a single sub-image.

6.3 Conclusion

In this chapter, we reported in detail experimental work on the light field imaging system, consisting two parts.

The prototype of an X-ray light field microscope in the "water window" range under construction are introduced in the first part. There is still a considerable amount of preparatory work to be done before the entire light field system can be investigated.

Currently, the major limitation of this experiment is the stable generation of the laser-plasma X-ray source. In further work, the effect of the pumping laser energy, the density distribution of the gas puff and the vacuum condition could be further explored to address this issue.

The second part presented the first experiment of X-ray plenoptic camera with synchrotron radiation. Image stitching acquisition is proved in this experiment to be useful to compensate the limitation of the available optics, but at the cost of acquisition time. The corresponding image processing for light field image extraction is discussed and addressed. Reconstructing experimental data by the algorithm originally developed for visible light system allows to change the focus along distance after the acquisition. The $3D$ spatial information of one test target can be recovered from the analysis of the experimental data.

Although this experiment is not entirely successful in extracting two separate images refocused on different test targets by post numerical processing, it does substantiate the feasibility of plenoptic camera in X-ray and the applicability of visible light field theory in X-ray. Moreover, this experiment confirms the current main limitation to implement light field imaging system in X-ray, that is, the lack of adapted X-ray optics.

Further research on the design and fabrication of compatible X-ray optics are strongly required to realize X-ray light field imaging system. Also, a better understanding of the combined implication of system structural parameters and reconstruction algorithm will be of great help.

Chapter 7

Conclusion And Perspectives

7.1 Outcomes

In the past three decades, visible light field imaging technology and the associated acquisition devise, the plenoptic camera, have experienced rapid development. However, few studies have investigated the light field imaging in the X-ray range. Therefore, the aim of this thesis was to implement the light field imaging in the X-ray range and prototype an X-ray plenoptic camera for biomedical applications. We adopted the major configuration of the sensor-side structured plenoptic camera in visible light consisting of main lens, microlens array and detector. Based on this configuration, the main issue we addressed was the search of alternative X-ray optics for the refractive lenses used in the visible light imaging system.

The research of prototyping an X-ray plenoptic camera started from the theoretical studies of light field imaging developed in visible light. We reviewed the development of light field imaging system and the relevant refocusing and depth extraction algorithms. We compared three basic refocusing algorithms and mathematically interpreted the interconnection between them. This work contributes to a deeper understanding of the principles of light field imaging.

To move towards X-ray light field microscope, we proposed a Fresnel zone plate (FZP) based plenoptic camera, namely replacing the refractive main lens and microlens array by the diffractive FZP and FZP array. The imaging performance of the FZP is highly

interrelated to its size, while the size of each FZP is greatly limited to make a dense lens array. Thereby, we developed a simulation algorithm on the base of scalar diffraction theory, which allows to simulate the images formed by the FZP with different geometries and under different coherence conditions, to determine the number of zones of each FZP related to its size in the array. The simulation results surprisingly showed that the image can be formed by the FZP with a number of zones as small as 5. And the contrast of FZP images improves rapidly with increasing number of zones. However, the contrast of the FZP images is relatively low compared to the refractive lens images, due to the overlap of different diffraction orders.

In parallel, we conceived an X-ray plenoptic camera toward X-ray light field scanning system, composed of a toroidal crystal as main lens, a FZP array and a detector, for larger samples such as mice or their organs working under higher source energy. The toroidal crystal was proposed as the main "lens" for its two imaging properties: the large effective diffracting area, leading to high numerical aperture and good beam flux collection, beneficial for image quality. The two imaging properties of the toroidal crystal have been first numerically verified using our ray-tracing algorithm. Two toroidal crystals of our customized design with high numerical aperture have been fabricated, and their curvatures and lattice structure have been globally examined by the X-ray diffraction measurements. The preliminary results of experimental focusing tests on one of the toroidal crystals further reveal the feasibility of toroidal crystal to serve as the main lens.

In addition to the investigation of the individual optical components mentioned above, we also worked on two experiments on the entire light field imaging systems at different X-ray energies. On the one hand, we constructed an experimental X-ray light field microscope in the "water window", for future X-ray volumetric imaging of biological specimens. On the other hand, we conducted the experiment of a FZP-based plenoptic camera with synchrotron radiation at 11 keV, the first real X-ray plenoptic camera. The relevant image pre-processing has been discussed and adapted to the image feature of FZP array. A light field image with the same structure of the one captured in visible

light has been extracted from the data captured by the X-ray experimental set-up. The focus change after the acquisition and the depth estimation, two main characteristics of light field imaging, have been reproduced with the X-ray experimental data. Taken together, these experimental results demonstrated the feasibility of the X-ray plenoptic camera and extended the application of light field imaging to the X-ray range.
Overall, the work carried out during this thesis contributed in several ways to our understanding of X-ray light field imaging and provided a foundation for the achievement of plenoptic camera in X-ray range.

7.2 Future Work

The work performed in this thesis provides the following insights for future research:
A speciality of the light field imaging is that the performance of a plenoptic camera is largely related to the post processing algorithm. More information on how the post processing quantitative affects the reconstruction of light field data would help to build a plenoptic camera with higher depth accuracy. More detail problems in reconstruction, such like occlusion and non-Lambertian case, still needed to be addressed. Incorporating the artificial intelligence, a major recent trend, is conducive to improving the performance and expanding the applications of light field imaging.
For the search of X-ray optics compatible with the light field imaging system, the current work mainly focuses on the FZP and curved crystal. A more extensive study of X-ray optics may lead to other possible options. Experiments on X-ray light field imaging systems with different geometries would be also worthwhile for dealing with the limitation from X-ray optics.
At current stage, the samples used in the experiments of X-ray light field imaging are composed of only two separate targets. A natural progression of this work is to test with continuous volumetric samples until real biological samples.
The application of laboratory X-ray source, such as desktop laser-plasma source and X-ray tube, will also greatly facilitate experimental investigation on X-ray light field imaging and accelerate the development. Moreover, as diffractive X-ray optic are sen-

sible to the source spectrum, the monochromatization of laboratory X-rays sources are also an important aspect for future experimental work.

Integrating each mentioned possible improvements, future experimental investigations on the entire system will be crucial to explore the achievable performance of light field imaging in the X-ray range. More broadly, comparisons with other X-ray 3D imaging technologies using controlled trials could provide a more explicit understanding of the advantages and shortcomings of light field imaging.

Appendix

7.A Definitions and equations of key parameters for the experimental plenoptic camera

The imaging performance of an imaging system can be quantitatively evaluated from several parameters such as field of view, numerical aperture, lateral resolution and depth of field. The definitions and equations of these parameters may vary in different literature, depending on the theoretical background applied, the specificity of the studied system or the focus of the study [119] [120] [121].

Here, the definitions and equations are confined to the plenoptic camera model experimentally investigated in section 6.2 of Chapter 6. The four performance parameters of the experimental plenoptic camera that we discussed are purely derived from the optical components and the system geometry, without considering the influence of the post numerical processing. More discussions on the imaging performance of the plenoptic camera can be found in the literature [15] [122], etc.

The geometry of the experimental plenoptic camera and the corresponding variables are given in figure 7.A.1, where

Z is the object distant,

z_0 is the distance between the main FZP and the FZP array,

z_1 is the image distance of the main FZP,

z_2 is the distance from the intermediate image formed by the main FZP to the FZP array,

and b is the distance between the FZP array to the detector.

Turning to the variables representing the size of optics,

d_A is the total size of the FZP array,

d_M, d_m are the diameters of the the main FZP and a sub-FZP of the array,

d_p is the pixel size of the detector.

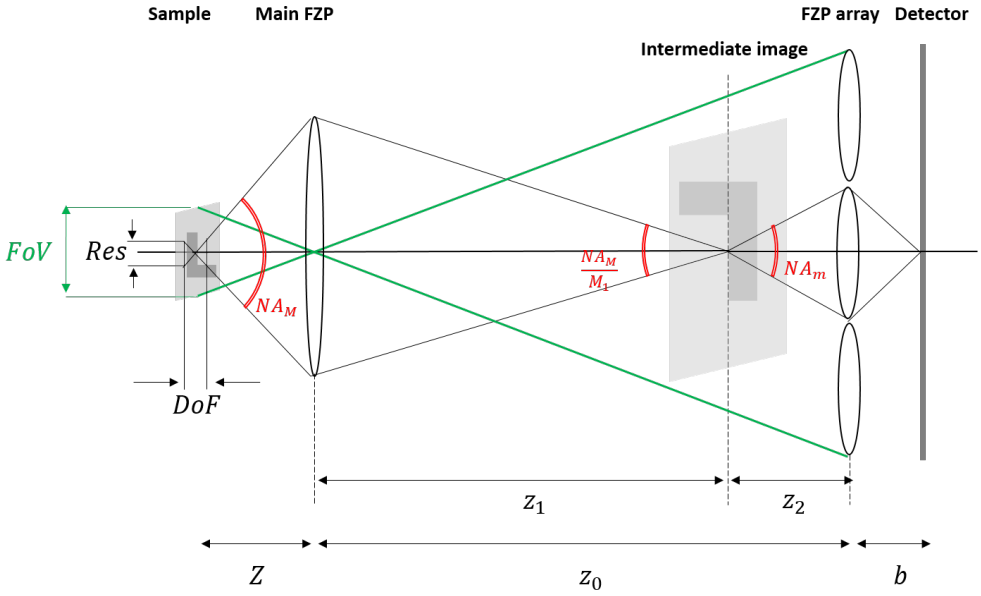

Figure 7.A.1: Sketch of the plenoptic camera experimentally investigated with synchrotron radiation. The values of the variables marked in the figure are given in section 6.2.5.1.

The four imaging performance parameters (field of view, numerical aperture, lateral resolution and depth of field) of the experimental plenoptic camera in the object plane are derived below with the mentioned variables:

- **Field of View (FoV)**

The field of view of the experimental plenoptic camera is defined as the area in the object plane that can be sampled by the FZP array through the main FZP. Considering

only the chief rays (green lines in figure 7.A.1) of the main FZP for simplification, the FoV can be given in the term of horizontal width as

$$FoV = \frac{d_A}{z_0} Z \tag{7.1}$$

- **Numerical Aperture (NA)**

The numerical aperture of an optics is a dimensionless number that indicates the range of angle over which it can collect light. The numerical aperture in the object side of the main FZP and a sub-FZP, denoted as NA_M and NA_m, respectively, are defined as

$$NA_M = \frac{d_M}{2Z} \tag{7.2}$$

$$NA_m = \frac{d_m}{2z_2} \tag{7.3}$$

The numerical aperture of the experimental plenoptic camera NA is limited by the minimum between NA_M and NA_m. Attention needs to be paid to the effect of lens magnification on the NA in different planes. We compare the numerical apertures in the intermediate planes, namely

$$NA' = min(\frac{NA_M}{M_1}, NA_m) \tag{7.4}$$

where M_1 is the magnification of the main FZP, $M_1 = z_1/Z$. NA' is the numerical aperture of the plenoptic camera in the intermediate planes. The NA in the object plane of the plenoptic camera is thus the corresponding magnified value of NA', i.e. $NA = M_1 \times NA'$.

- **Lateral Resolution (Res)**

We define the lateral resolution *Res* of plenoptic camera as the minimum distance to distinguish two points in the object plane, which is a common definition for the resolution of imaging systems such as microscope and telescope. The lateral resolution of the plenoptic camera *Res* is affected by the resolution of each component and is equal

to the largest necessary distinguishable distance. We analyze first the resolution of each component.

The resolution of the detector Res_D is determined by the pixel size d_p.

$$Res_D = d_p \tag{7.5}$$

The resolution of the lenses (main FZP and sub-FZP) in the object side derived from wave optics are related to their numerical apertures. According to the Rayleigh criterion [123], Res_M and Res_m can be written in terms of NA_M and NA_m as

$$Res_M = 0.61\frac{\lambda}{NA_M} \tag{7.6}$$

$$Res_m = 0.61\frac{\lambda}{NA_m} \tag{7.7}$$

Due to the different magnifications of each plane, we further convert Res_M and Res_D to the effective values in the intermediate imaging plane to determine maximum (the largest necessary distinguishable distance), yielding

$$Res' = max(M_1 Res_M,\ Res_m,\ \frac{d_p}{M_2}) \tag{7.8}$$

where $M_1 = \frac{z_1}{Z}$ and $M_2 = \frac{z_2}{b}$, and the Res' is the resolution of the plenoptic camera in the intermediate image plane.

Substituting the resolution of each component, the resolution of the plenoptic camera in the intermediate image plane becomes

$$Res' = max(M_1(0.61\frac{\lambda}{NA_M}),\ 0.61\frac{\lambda}{NA_m},\ \frac{d_p}{M_2}) \tag{7.9}$$

Converting back to the object plane, the resolution of the plenoptic camera is

$$Res = \frac{Res'}{M_1} \tag{7.10}$$

- **Depth of Field (DoF)**

In the regime of geometrical optics, depth of field is the axial range around the object plane within which the image of the object at any position is all acceptably resolved on the sensor. In the regime of wave optics, the depth of field refers to the tolerant focus range on the axis, depending on the axial intensity distribution of focus. Taking into account the influence of the two aspects, the equation of total DoF_{tot} is given in the literature [121] as

$$DoF_{tot} = DoF_{geo} + DoF_{wave} = \frac{\lambda}{NA^2} + \frac{Res}{NA} \tag{7.11}$$

In the section 6.2.5.1, we calculate the DoF in the object side of the plenoptic camera, within which the object is considered as resolved in a single sub-image without the post numerical processing. The extension of DoF with the post numerical processing, resulting from the cross-effect of different sub-images, is discussed in the section 6.2.5.2. In our experimental set-up, the resolution of detector is close to the diffraction limit of the FZPs. The DoF_{wave} thus dominates in the equation, and the DoF is given by

$$DoF = \frac{\lambda}{NA^2} \tag{7.12}$$

where NA is the numerical aperture of the plenoptic camera in the object plane previously discussed.

The equations of the four parameters derived for the experimental plenoptic camera are summarised in the table 7.A.1.

Field of View (FoV)	$\frac{d_A}{z_0} Z$
Numerical aperture (NA)	$M_1 \times min(\frac{NA_M}{M_1}, NA_m)$
Lateral Resolution (Res)	$\frac{1}{M_1} \times max(M_1(0.61\frac{\lambda}{NA_M}),\ 0.61\frac{\lambda}{NA_m},\ \frac{d_p}{M_2})$
Depth of Field (DoF)	$\frac{\lambda}{NA^2}$

Table 7.A.1: Equations summary of four imaging performance parameters derived from the experimental plenoptic camera.

Bibliography

[1] Michael Faraday. “LIV. Thoughts on ray-vibrations.” In: *The London, Edinburgh, and Dublin Philosophical Magazine and Journal of Science* 28.188 (1846), pp. 345–350 (cit. on p. 5).

[2] Andreı Gershun. “The light field.” In: *Journal of Mathematics and Physics* 18.1-4 (1939), pp. 51–151 (cit. on p. 5).

[3] EH ADELSON. “" The Plenoptic Function and the Elements of Early Vision", Computational Models of Visual.” In: *Processing, Chap. 1, Edited by M. Landy and JA Movshon* (1991) (cit. on p. 5).

[4] Marc Levoy and Pat Hanrahan. “Light field rendering.” In: *Proceedings of the 23rd annual conference on Computer graphics and interactive techniques*. 1996, pp. 31–42 (cit. on pp. 5, 6).

[5] Steven J Gortler et al. “The lumigraph.” In: *Proceedings of the 23rd annual conference on Computer graphics and interactive techniques*. 1996, pp. 43–54 (cit. on pp. 5, 6).

[6] Gabriel Lippmann. “Epreuves reversibles donnant la sensation du relief.” In: *J. Phys. Theor. Appl.* 7.1 (1908), pp. 821–825 (cit. on p. 7).

[7] Edward H Adelson and John YA Wang. “Single lens stereo with a plenoptic camera.” In: *IEEE transactions on pattern analysis and machine intelligence* 14.2 (1992), pp. 99–106 (cit. on p. 7).

[8] Ren Ng et al. *Light Field Photography with a Hand-held Plenoptic Camera*. Research Report CSTR 2005-02. Stanford university, Apr. 2005, Stanford University Computer Science Tech Report. URL: https://hal.archives-ouvertes.fr/hal-02551481 (cit. on pp. 8, 21, 22).

[9] Andrew Lumsdaine and Todor Georgiev. “The focused plenoptic camera.” In: *2009 IEEE International Conference on Computational Photography (ICCP)*. IEEE. 2009, pp. 1–8 (cit. on p. 8).

[10] Bennett Wilburn et al. “High performance imaging using large camera arrays.” In: *ACM SIGGRAPH 2005 Papers*. 2005, pp. 765–776 (cit. on p. 8).

[11] Todor Georgiev and Chintan Intwala. "Light field camera design for integral view photography." In: *Adobe Technical Report* 1 (2006), p. 13 (cit. on p. 8).

[12] Anat Levin et al. "Image and depth from a conventional camera with a coded aperture." In: *ACM transactions on graphics (TOG)* 26.3 (2007), 70–es (cit. on pp. 8, 9).

[13] Wikipedia. *Lytro*. https://en.wikipedia.org/wiki/Lytro. Accessed: 2022-05-11 (cit. on p. 8).

[14] raytrix. *3D Light-Field Cameras with 4D Plenoptic Depth Sensors*. https://raytrix.de/products/. Accessed: 2022-05-11 (cit. on p. 8).

[15] Charlotte Herzog. "plenoptic imaging : from visible light to X-rays." Theses. Université de Bordeaux, Sept. 2020. URL: https://tel.archives-ouvertes.fr/tel-03129863 (cit. on pp. 9, 10, 144).

[16] Edmund Y Lam. "Computational photography with plenoptic camera and light field capture: tutorial." In: *JOSA A* 32.11 (2015), pp. 2021–2032 (cit. on p. 18).

[17] Berthold Horn, Berthold Klaus, and Paul Horn. *Robot vision*. MIT press, 1986 (cit. on p. 20).

[18] Ren Ng. *Digital light field photography*. stanford university, 2006 (cit. on p. 20).

[19] Pierre Matysiak et al. "A pipeline for lenslet light field quality enhancement." In: *2018 25th IEEE International Conference on Image Processing (ICIP)*. IEEE. 2018, pp. 639–643 (cit. on p. 20).

[20] Pierre Matysiak et al. "High quality light field extraction and post-processing for raw plenoptic data." In: *IEEE Transactions on Image Processing* 29 (2020), pp. 4188–4203 (cit. on pp. 20, 21).

[21] Mark Brady and Gordon E Legge. "Camera calibration for natural image studies and vision research." In: *JOSA A* 26.1 (2009), pp. 30–42 (cit. on p. 20).

[22] Alexander A Sawchuk. "Real-time correction of intensity nonlinearities in imaging systems." In: *IEEE Transactions on Computers* 100.1 (1977), pp. 34–39 (cit. on p. 20).

[23] FJ WM Leong, M Brady, and J O'D McGee. "Correction of uneven illumination (vignetting) in digital microscopy images." In: *Journal of clinical pathology* 56.8 (2003), pp. 619–621 (cit. on p. 20).

[24] Lois Mignard-Debise and Ivo Ihrke. "A vignetting model for light field cameras with an application to light field microscopy." In: *IEEE Transactions on Computational Imaging* 5.4 (2019), pp. 585–595 (cit. on p. 20).

[25] Suning Li et al. "High-Accuracy Correction of a Microlens Array for Plenoptic Imaging Sensors." In: *Sensors* 19.18 (2019), p. 3922 (cit. on p. 20).

[26] Changkun Yang et al. "Improved Camera Distortion Correction and Depth Estimation for Lenslet Light Field Camera." In: *Photogrammetric Engineering & Remote Sensing* 85.3 (2019), pp. 197–208 (cit. on p. 20).

[27] Chelsea M Thomason, Brian S Thurow, and Timothy W Fahringer. "Calibration of a microlens array for a plenoptic camera." In: *52nd aerospace sciences meeting*. 2014, p. 0396 (cit. on p. 20).

[28] S Xu, ZL Zhou, and N Devaney. *Multi-view Image Restoration from Plenoptic Raw Images, chapter ACCV*. 2015 (cit. on p. 20).

[29] Xin Jin, Xufu Sun, and Chuanpu Li. "Geometry parameter calibration for focused plenoptic cameras." In: *Optics express* 28.3 (2020), pp. 3428–3441 (cit. on p. 20).

[30] Donald G Dansereau, Oscar Pizarro, and Stefan B Williams. "Decoding, calibration and rectification for lenselet-based plenoptic cameras." In: *Proceedings of the IEEE conference on computer vision and pattern recognition*. 2013, pp. 1027–1034 (cit. on p. 21).

[31] Ole Johannsen et al. "On the calibration of focused plenoptic cameras." In: *Time-of-Flight and Depth Imaging. Sensors, Algorithms, and Applications*. Springer, 2013, pp. 302–317 (cit. on p. 21).

[32] Niclas Zeller et al. "Metric calibration of a focused plenoptic camera based on a 3D calibration target." In: *ISPRS Annals of Photogrammetry, Remote Sensing and Spatial Information Sciences* 3 (2016), pp. 449–456 (cit. on p. 21).

[33] Yunsu Bok, Hae-Gon Jeon, and In So Kweon. "Geometric calibration of micro-lens-based light field cameras using line features." In: *IEEE transactions on pattern analysis and machine intelligence* 39.2 (2016), pp. 287–300 (cit. on p. 21).

[34] Pierre David, Mikaël Le Pendu, and Christine Guillemot. "White lenslet image guided demosaicing for plenoptic cameras." In: *2017 IEEE 19th International Workshop on Multimedia Signal Processing (MMSP)*. IEEE. 2017, pp. 1–6 (cit. on p. 21).

[35] Martin Alain and Aljosa Smolic. "Light field denoising by sparse 5D transform domain collaborative filtering." In: *2017 IEEE 19th International Workshop on Multimedia Signal Processing (MMSP)*. IEEE. 2017, pp. 1–6 (cit. on p. 21).

[36] Andrew Lumsdaine, Todor Georgiev, et al. "Full resolution lightfield rendering." In: *Indiana University and Adobe Systems, Tech. Rep* 91 (2008), p. 92 (cit. on p. 30).

[37] Todor G Georgiev and Andrew Lumsdaine. "Focused plenoptic camera and rendering." In: *Journal of Electronic Imaging* 19.2 (2010), p. 021106 (cit. on p. 31).

[38] Christopher Hahne et al. "Raw image data taken by a standard plenoptic camera." In: (Sept. 2016). DOI: 10.6084/m9.figshare.3362152.v1. URL: https://opticapublishing.figshare.com/articles/dataset/Raw_image_data_taken_by_a_standard_plenoptic_camera/3362152 (cit. on pp. 34, 35).

[39] Christopher Hahne et al. "Refocusing distance of a standard plenoptic camera." In: *Optics Express* 24.19 (2016), pp. 21521–21540 (cit. on p. 35).

[40] José Luis Pech-Pacheco et al. "Diatom autofocusing in brightfield microscopy: a comparative study." In: *Proceedings 15th International Conference on Pattern Recognition. ICPR-2000*. Vol. 3. IEEE. 2000, pp. 314–317 (cit. on p. 36).

[41] Harsh Nanda and Ross Cutler. "Practical calibrations for a real-time digital omnidirectional camera." In: *CVPR Technical Sketch* 20.2 (2001) (cit. on p. 36).

[42] Murali Subbarao, Tae Choi, and Arman Nikzad. "Focusing Techniques." In: *Journal of Optical Engineering* 32 (1993), pp. 2824–2836 (cit. on p. 36).

[43] Megan J Russell and Tania S Douglas. "Evaluation of autofocus algorithms for tuberculosis microscopy." In: *2007 29th Annual International Conference of the IEEE Engineering in Medicine and Biology Society*. IEEE. 2007, pp. 3489–3492 (cit. on p. 36).

[44] Ge Yang and Bradley J Nelson. "Wavelet-based autofocusing and unsupervised segmentation of microscopic images." In: *Proceedings 2003 IEEE/RSJ International Conference on Intelligent Robots and Systems (IROS 2003)(Cat. No. 03CH37453)*. Vol. 3. IEEE. 2003, pp. 2143–2148 (cit. on p. 36).

[45] Hui Xie, Weibin Rong, and Lining Sun. "Wavelet-based focus measure and 3-d surface reconstruction method for microscopy images." In: *2006 IEEE/RSJ International Conference on Intelligent Robots and Systems*. IEEE. 2006, pp. 229–234 (cit. on p. 36).

[46] Filip Rooms et al. "PSF estimation with applications in autofocus and image restoration." In: *Ieee signal processing symposium, leuven, belgium*. 2002 (cit. on p. 36).

[47] Said Pertuz, Domenec Puig, and Miguel Angel Garcia. "Analysis of focus measure operators for shape-from-focus." In: *Pattern Recognition* 46.5 (2013), pp. 1415–1432 (cit. on p. 36).

[48] Sven Wanner and Bastian Goldluecke. "Globally consistent depth labeling of 4D light fields." In: *2012 IEEE Conference on Computer Vision and Pattern Recognition*. IEEE. 2012, pp. 41–48 (cit. on p. 36).

[49] Alessandro Vianello et al. "Robust hough transform based 3D reconstruction from circular light fields." In: *Proceedings of the IEEE Conference on Computer Vision and Pattern Recognition*. 2018, pp. 7327–7335 (cit. on p. 36).

[50] Alessandro Vianello et al. "3D reconstruction by a combined structure tensor and Hough transform light field approach." In: *tm-Technisches Messen* 84.7-8 (2017), pp. 460–478 (cit. on p. 36).

[51] Yongbing Zhang et al. "Light-field depth estimation via epipolar plane image analysis and locally linear embedding." In: *IEEE Transactions on Circuits and Systems for Video Technology* 27.4 (2016), pp. 739–747 (cit. on p. 37).

[52] Changil Kim et al. "Scene reconstruction from high spatio-angular resolution light fields." In: *ACM Trans. Graph.* 32.4 (2013), pp. 73–1 (cit. on p. 37).

[53] Michael W Tao et al. "Depth from combining defocus and correspondence using light-field cameras." In: *Proceedings of the IEEE International Conference on Computer Vision*. 2013, pp. 673–680 (cit. on p. 37).

[54] Hao Sheng et al. "Occlusion-aware depth estimation for light field using multi-orientation EPIs." In: *Pattern Recognition* 74 (2018), pp. 587–599 (cit. on p. 37).

[55] Ting-Chun Wang, Alexei A Efros, and Ravi Ramamoorthi. "Occlusion-aware depth estimation using light-field cameras." In: *Proceedings of the IEEE International Conference on Computer Vision*. 2015, pp. 3487–3495 (cit. on p. 37).

[56] Haiting Lin et al. "Depth recovery from light field using focal stack symmetry." In: *Proceedings of the IEEE International Conference on Computer Vision*. 2015, pp. 3451–3459 (cit. on p. 37).

[57] Neus Sabater et al. "Accurate disparity estimation for plenoptic images." In: *European Conference on Computer Vision*. Springer. 2014, pp. 548–560 (cit. on p. 37).

[58] Hae-Gon Jeon et al. "Accurate depth map estimation from a lenslet light field camera." In: *Proceedings of the IEEE conference on computer vision and pattern recognition*. 2015, pp. 1547–1555 (cit. on p. 37).

[59] Stefan Heber and Thomas Pock. "Convolutional networks for shape from light field." In: *Proceedings of the IEEE Conference on Computer Vision and Pattern Recognition*. 2016, pp. 3746–3754 (cit. on p. 37).

[60] Youngjin Yoon et al. "Learning a deep convolutional network for light-field image super-resolution." In: *Proceedings of the IEEE international conference on computer vision workshops*. 2015, pp. 24–32 (cit. on p. 37).

[61] Felix Heide, Wolfgang Heidrich, and Gordon Wetzstein. "Fast and flexible convolutional sparse coding." In: *Proceedings of the IEEE Conference on Computer Vision and Pattern Recognition*. 2015, pp. 5135–5143 (cit. on p. 37).

[62] Bertram Eugene Warren. *X-ray Diffraction*. Courier Corporation, 1990 (cit. on p. 39).

[63] Janos Kirz, Chris Jacobsen, and Malcolm Howells. "Soft X-ray microscopes and their biological applications." In: *Quarterly reviews of biophysics* 28.1 (1995), pp. 33–130 (cit. on p. 39).

[64] Weilun Chao et al. "Soft X-ray microscopy at a spatial resolution better than 15 nm." In: *Nature* 435.7046 (2005), pp. 1210–1213 (cit. on p. 39).

[65] PAC Takman et al. "High-resolution compact X-ray microscopy." In: *Journal of microscopy* 226.2 (2007), pp. 175–181 (cit. on p. 39).

[66] Ryan C Moffet, Alexei V Tivanski, and Mary K Gilles. *Scanning transmission X-ray microscopy: Applications in atmospheric aerosol research*. Tech. rep. Lawrence Berkeley National Lab.(LBNL), Berkeley, CA (United States), 2011 (cit. on p. 39).

[67] Martin D De Jonge and Stefan Vogt. "Hard X-ray fluorescence tomography—an emerging tool for structural visualization." In: *Current opinion in structural biology* 20.5 (2010), pp. 606–614 (cit. on p. 39).

[68] Alexei Erko et al. *Modern developments in X-ray and neutron optics*. Vol. 137. Springer, 2008 (cit. on p. 40).

[69] Enzo Di Fabrizio et al. "High-efficiency multilevel zone plates for keV X-rays." In: *Nature* 401.6756 (1999), pp. 895–898 (cit. on p. 40).

[70] Joan Vila-Comamala et al. "Advanced thin film technology for ultrahigh resolution X-ray microscopy." In: *Ultramicroscopy* 109.11 (2009), pp. 1360–1364 (cit. on p. 40).

[71] A Do et al. "Characterization of a two-channel, high resolution hard x-ray microscope using Fresnel zone plates for laser-plasma interaction experiments." In: *Review of Scientific Instruments* 89.10 (2018), 10G122 (cit. on p. 40).

[72] K Jefimovs et al. "Fabrication of Fresnel zone plates for hard X-rays." In: *Microelectronic Engineering* 84.5-8 (2007), pp. 1467–1470 (cit. on p. 40).

[73] M Awaji et al. "X-ray imaging microscopy at 25 keV with Fresnel zone plate optics." In: *Nuclear Instruments and Methods in Physics Research Section A: Accelerators, Spectrometers, Detectors and Associated Equipment* 467 (2001), pp. 845–848 (cit. on p. 40).

[74] David Attwood. *Soft x-rays and extreme ultraviolet radiation: principles and applications*. Cambridge university press, 2000 (cit. on p. 43).

[75] Jack D Gaskill. "Linear systems, Fourier transforms, and optics." In: *Linear Systems* (1978) (cit. on p. 46).

[76] Joseph W Goodman. "Introduction to Fourier Optics, Roberts & Co." In: *Publishers, Englewood, Colorado* (2005) (cit. on p. 47).

[77] Jeffrey A Fessler and Bradley P Sutton. "Nonuniform fast Fourier transforms using min-max interpolation." In: *IEEE transactions on signal processing* 51.2 (2003), pp. 560–574 (cit. on p. 49).

[78] Julius O Smith III. "Audio signal processing in Faust." In: *online tutorial: https://ccrma. stanford. edu/jos/aspf* (2010) (cit. on p. 49).

[79] David George Voelz. *Computational fourier optics: a MATLAB tutorial*. SPIE press Bellingham, WA, 2011 (cit. on p. 54).

[80] Okan K Ersoy. *Diffraction, Fourier optics and imaging*. Vol. 30. John Wiley & Sons, 2006 (cit. on p. 54).

[81] Przemyslaw Wachulak et al. "Nanoimaging using soft X-ray and EUV laser-plasma sources." In: *EPJ Web of Conferences*. Vol. 167. EDP Sciences. 2018, p. 03001 (cit. on p. 67).

[82] PW Wachulak. "Recent advancements in the "water-window" microscopy with laser-plasma SXR source based on a double stream gas-puff target." In: *Opto-Electronics Review* 24.3 (2016), pp. 144–154 (cit. on p. 67).

[83] Satoshi Matsuyama et al. "Nearly diffraction-limited X-ray focusing with variable-numerical-aperture focusing optical system based on four deformable mirrors." In: *Scientific reports* 6.1 (2016), pp. 1–8 (cit. on p. 67).

[84] T Ejima et al. "Multilayer coated grazing incidence condenser for large numerical aperture objective at wavelength of 4.5 nm." In: *Applied optics* 53.29 (2014), pp. 6846–6852 (cit. on p. 67).

[85] Anatoly Snigirev et al. "A compound refractive lens for focusing high-energy X-rays." In: *Nature* 384.6604 (1996), pp. 49–51 (cit. on p. 67).

[86] Saint-Gobain. *X-Ray Analyzers*. [Online; accessed August 04, 2022]. URL: https://www.crystals.saint-gobain.com/x-ray-analyzers# (cit. on p. 67).

[87] Saša Bajt et al. "X-ray focusing with efficient high-NA multilayer Laue lenses." In: *Light: Science & Applications* 7.3 (2018), pp. 17162–17162 (cit. on p. 67).

[88] William Lawrence Bragg. "The diffraction of short electromagnetic waves by a crystal." In: *Scientia* 23.45 (1929) (cit. on p. 67).

[89] R Caciuffo et al. "Monochromators for x-ray synchrotron radiation." In: *Physics Reports* 152.1 (1987), pp. 1–71 (cit. on p. 67).

[90] Tadashi Matsushita and H Hashizume. "X-ray monochromators." In: *Handbook on synchrotron radiation* 1 (1983), pp. 261–314 (cit. on p. 67).

[91] L v Hámos. "Formation of true x-ray images by reflection on crystal mirrors." In: *Zeitschrift für Kristallographie-Crystalline Materials* 101.1-6 (1939), pp. 17–29 (cit. on p. 67).

[92] Dwight W Berreman, J t Stamatoff, and SJ Kennedy. "Doubly curved crystal point-focusing x-ray monochromators: geometrical and practical optics." In: *Applied Optics* 16.8 (1977), pp. 2081–2085 (cit. on p. 67).

[93] A Hauer, JD Kilkenny, and OL Landen. "Toroidally curved crystal for time-resolved x-ray spectroscopy." In: *Review of Scientific Instruments* 56.5 (1985), pp. 803–805 (cit. on p. 67).

[94] André Guinier. *X-ray crystallographic technology*. Hilger and Watts, 1952 (cit. on p. 69).

[95] Henry A Rowland. "XXIX. On concave gratings for optical purposes." In: *The London, Edinburgh, and Dublin Philosophical Magazine and Journal of Science* 16.99 (1883), pp. 197–210 (cit. on p. 70).

[96] SL Hulbert et al. *Vacuum ultraviolet spectroscopy*. Vol. 2. Elsevier, 2000 (cit. on p. 72).

[97] Shyam Singh. "Diffraction gratings: aberrations and applications." In: *Optics & Laser Technology* 31.3 (1999), pp. 195–218 (cit. on p. 72).

[98] H Johann. "Intense X-ray spectra obtained with concave crystals." In: *Z. Phys* 69 (1931), p. 185 (cit. on p. 72).

[99] David B Wittry and Nicholas C Barbi. "X-ray crystal spectrometers and monochromators in microanalysis." In: *Microscopy and Microanalysis* 7.2 (2001), pp. 124–141 (cit. on p. 72).

[100] T Johansson. "New focusing x-ray spectrometer crystals." In: *Z. Phys* 82 (1933), p. 507 (cit. on p. 73).

[101] David B Wittry and Songquan Sun. "X-ray optics of doubly curved diffractors." In: *Journal of applied physics* 67.4 (1990), pp. 1633–1638 (cit. on pp. 76, 78).

[102] Vincent JACQUES. *4-circle diffractometer*. [Online; accessed April 22, 2022]. URL: http://hebergement.universite-paris-saclay.fr/jacques/diffraction-x-de-laboratoire/ (cit. on p. 85).

[103] Marc Levoy et al. "Light field microscopy." In: *ACM SIGGRAPH 2006 Papers*. 2006, pp. 924–934 (cit. on p. 100).

[104] Robert Prevedel et al. "Simultaneous whole-animal 3D imaging of neuronal activity using light-field microscopy." In: *Nature methods* 11.7 (2014), pp. 727–730 (cit. on p. 100).

[105] Nicolas C Pégard et al. "Compressive light-field microscopy for 3D neural activity recording." In: *Optica* 3.5 (2016), pp. 517–524 (cit. on p. 100).

[106] Zhenkun Zhang et al. "Imaging volumetric dynamics at high speed in mouse and zebrafish brain with confocal light field microscopy." In: *Nature Biotechnology* 39.1 (2021), pp. 74–83 (cit. on p. 100).

[107] Przemyslaw W Wachulak et al. "Water-window microscopy using a compact, laser-plasma SXR source based on a double-stream gas-puff target." In: *Applied Physics B* 111.2 (2013), pp. 239–247 (cit. on p. 100).

[108] Łukasz Węgrzyński et al. "Laser-produced plasma soft x-ray source based on an aerosol target." In: *Physics of Plasmas* 27.7 (2020), p. 073102 (cit. on p. 102).

[109] Przemyslaw W Wachulak et al. "Desktop water window microscope using a double-stream gas puff target source." In: *Applied Physics B* 118.4 (2015), pp. 573–578 (cit. on p. 104).

[110] Desy PETRA-III. *Beamline P05*. https://confluence.desy.de/display/P5I/Beamline+overview (cit. on p. 106).

[111] James Anthony Seibert, John M Boone, and Karen K Lindfors. "Flat-field correction technique for digital detectors." In: *Medical Imaging 1998: Physics of Medical Imaging*. Vol. 3336. SPIE. 1998, pp. 348–354 (cit. on p. 113).

[112] John C Russ. *The image processing handbook*. CRC press, 2006 (cit. on p. 119).

[113] John Illingworth and Josef Kittler. "The adaptive Hough transform." In: *IEEE Transactions on Pattern Analysis and Machine Intelligence* 5 (1987), pp. 690–698 (cit. on p. 119).

[114] Gunilla Borgefors. "Distance transformations in arbitrary dimensions." In: *Computer vision, graphics, and image processing* 27.3 (1984), pp. 321–345 (cit. on p. 119).

[115] C Gonzalez Rafael et al. *Digital image processing using MATLAB*. Tata McGraw-Hill, 2010 (cit. on p. 119).

[116] Ming-Kuei Hu. "Visual pattern recognition by moment invariants." In: *IRE transactions on information theory* 8.2 (1962), pp. 179–187 (cit. on p. 119).

[117] Charlotte Herzog. "plenoptic imaging: from visible light to X-rays." PhD thesis. Université de Bordeaux, 2020 (cit. on p. 134).

[118] Charlotte Herzog et al. "Study of contrast variations with depth in focused plenoptic cameras." In: *Optics Letters* 44.19 (2019), pp. 4825–4828 (cit. on p. 134).

[119] Shree K Nayar and Yasuo Nakagawa. "Shape from focus." In: *IEEE Transactions on Pattern analysis and machine intelligence* 16.8 (1994), pp. 824–831 (cit. on p. 144).

[120] Max Born and Emil Wolf. *Principles of optics: electromagnetic theory of propagation, interference and diffraction of light*. Elsevier, 2013 (cit. on p. 144).

[121] Michael Bass et al. *Handbook of optics*. Vol. 2. McGraw-Hill New York, 1995 (cit. on pp. 144, 148).

[122] Manuel Martınez-Corral and Bahram Javidi. "Fundamentals of 3D imaging and displays: a tutorial on integral imaging, light-field, and plenoptic systems." In: *Advances in Optics and Photonics* 10.3 (2018), pp. 512–566 (cit. on p. 144).

[123] Lord Rayleigh. "XXXI. Investigations in optics, with special reference to the spectroscope." In: *The London, Edinburgh, and Dublin Philosophical Magazine and Journal of Science* 8.49 (1879), pp. 261–274 (cit. on p. 147).

ECOLE
DOCTORALE

Titre : Études numériques et expérimentales de systèmes d'imagerie plénoptique à rayons X

Mots clés : Plénoptique, Rayons X, Imagerie 3D

Résumé : L'information de chaque rayon lumineux dans l'espace peut être modélisée par les coordonnées dans deux plans, d'où provient la notion de champ de lumière en 4 dimensions (4D). Le système d'imagerie utilisé pour acquérir cette information 4D est appelé caméra plénoptique et a beaucoup été étudié dans le domaine du visible. Il a été démontré pour le domaine du visible que la capture du champ de lumière 4D permet de numériquement refocaliser l'image à différentes profondeurs et d'obtenir un modèle 3D d'un échantillon en une seule acquisition. Cependant, jusqu'à maintenant, peu d'études se sont intéressées aux systèmes d'imagerie plénoptique dans le domaine des rayons X.
Comparée à la tomographie, l'imagerie plénoptique à rayons X a deux avantages : d'une part, elle permettrait de réduire le temps d'exposition et donc la dose reçue aux échantillons biologiques. D'autre part, l'imagerie plénoptique à rayons X ne requiert pas de tourner l'échantillon, ni de l'immobiliser, ce qui permettrait de reconstruire des images 3D d'échantillons vivants ou en mouvement. Le but de ce travail de thèse est donc de construire un prototype de caméra plénoptique avec des éléments optiques fonctionnant pour les rayons X et permettant de façon préliminaire de reconstruire des images quasi-3D en très peu d'acquisitions. Dans ce but, le travail présenté dans ce manuscrit est séparé en quatre grandes parties :
Dans la première partie, nous faisons une revue du développement des systèmes d'imagerie plénoptique pour la lumière visible ainsi que des algorithmes. Nous avons démontré mathématiquement l'interconnexion entre les trois algorithmes de refocalisation en se basant sur l'optique géométrique. Dans la deuxième partie, nous proposons une caméra plénoptique pour rayons X mous (0.4 keV) basée sur les lentilles de Fresnel (en anglais ≪ Fresnel zone plate ≫, FZP). Pour concevoir une matrice dense de FZP pour l'imagerie plénoptique à rayons X, il faut réaliser un compromis entre la taille et la résolution de chaque FZP. La performance d'une FZP est déterminée par sa géométrie. Pour régler ce problème, une méthode de simulation basée sur la diffraction scalaire a été développée dans cette partie. A l'aide de cette simulation, l'effet du nombre de zones sur la formation d'une image par la FZP est discuté, et particulièrement dans le cas d'un très petit nombre de zones.
Pour les rayons X durs (17 keV), nous avons conçu un système d'imagerie plénoptique basé sur un cristal courbé comme ≪ lentille ≫ principale, qui est présenté dans la troisième section. Pour ce faire, un algorithme de tracé de rayons a été développé pour permettre d'étudier les propriétés d'imagerie de différentes configurations du cristal. A l'aide de ces calculs, nous montrons qu'un cristal torique possède une grande ouverture numérique et produit une focalisation point à point.
La dernière section décrit deux expériences sur des caméras plénoptiques pour des rayons X à différentes énergies. D'abord, la mise en place d'un microscope plénoptique expérimental dans la fenêtre dite ≪ de l'eau ≫ (0.43 keV) est détaillée. Ensuite, la première expérience avec rayonnement synchrotron à 11 keV d'un système d'imagerie plénoptique à rayons X basé sur les FZP est présentée. Le changement de la focale en fonction de la profondeur et l'information de profondeur de la cible ont été obtenus à partir des données expérimentales. Ces résultats montrent la validité pour les rayons X de la théorie plénoptique développée pour la lumière visible, ainsi que la faisabilité d'un système d'imagerie plénoptique à rayons X.

Title : Numerical and experimental studies of X-ray light field imaging systems

Keywords : Light field, X-rays, 3D imaging

Abstract : The information carried by each light ray in space can be parameterized by the coordinates of two planes, which generates the notion of 4-dimension (4D) light field. The imaging system to acquire such 4D light field information, so-called plenoptic camera, has been widely studied in visible. It has been demonstrated in visible light that the captured 4D light field allows for numerically refocusing the image at different depths and rendering a 3D model of the sample with one exposure. So far, however, there have been very limited developments about X-ray light field imaging system.
Compared to computed tomography, X-ray light field imaging has two major advantages: On the one hand, X-ray light field imaging has the property of acquiring 3D information with short exposure time, leading to lower doses and thus less radiation damage to biological samples. On the other hand, the data collection of X-ray light field imaging does not require the rotation or the immobilization of the sample, which allows to reconstruct 3D video of alive or moving sample. Therefore, the goal of the thesis is to build a prototype of X-ray plenoptic imaging system with suitable optical elements, enabling near-3D X-ray images in very few exposures in primary stage. The related work of the thesis can be divided into four main sections:
The first section reviewed the development of light field imaging system in visible light and the relevant refocusing and depth extraction algorithms. We mathematically demonstrated the interconnection between the three refocusing algorithms based on geometrical optics.
In the second section, we proposed a plenoptic camera based on Fresnel zone plates (FZP) for soft X-ray of 0.4 keV. To design a dense FZP array for X-ray light field imaging system, there exists a trade-off between the size and the resolution of each FZP. To address this issue, a simulation method based on scalar diffraction has been developed in this section. With the help of the simulation method, the effect of the number of zones on FZP image formation has been discussed, especially the case of very small number of zones.
For hard X-rays of 17 keV, we conceived an X-ray light field imaging system with a curved crystal as main "lens", which is introduced in the third section. A ray-tracing algorithm has been accordingly developed, which allows to examine the imaging property of the crystal with different geometries. Verified by our ray-tracing calculation, toroidally curved crystal exhibits high numerical aperture and point-to-point focusing property and is thus selected to be the main "lens".
The final section reported the experimental work on two plenoptic cameras at different X-ray energy. Firstly, the construction of an experimental X-ray light field microscope in the "water window" (0.43 keV) is described in detail. Secondly, the first experiment of the FZP-based X-ray light field imaging system with synchrotron radiation at 11 keV are presented with results. Numerical focus change and depth extraction have been achieved from X-ray experimental data. The experimental results demonstrated the applicability of visible light field theory in X-ray range and the feasibility of X-ray light field imaging system.

Institut Polytechnique de Paris
91120 Palaiseau, France